Design of Slow Light Modes in Photonic Crystal Ring Resonators

Kathleen McGarvey-Lechable

A Thesis
In
The Department
of
Physics

Presented in Partial Fulfillment of the Requirements
for the Degree of Master of Science (Physics) at
Concordia University
Montréal, Québec, Canada

March 2015

CONCORDIA UNIVERSITY

School of Graduate Studies

This is to certify that the thesis prepared

By: Kathleen McGarvey-Lechable

Entitled: Design of slow light resonant modes in photonic crystal ring resonators

and submitted in partial fulfillment of the requirements for the degree of

Master of Physics

complies with the regulations of this University and meets the accepted standards with respect to originality and quality.

Signed by the final examining commitee:

_____ Chair
Dr. Christophe Grova

_____ Examiner
Dr. Mariana Frank

_____ Examiner
Dr. Claudine Gauthier

_____ Supervisor
Dr. Pablo Bianucci

Approved _____
Chair of Department or Graduate Program Director

_____ 2015 _____
André Roy, Dean
Faculty of Arts and Sciences

ABSTRACT

Design of slow light modes in photonic crystal ring resonators

Kathleen McGarvey-Lechable

This work explores the optical properties of a photonic crystal ring resonator (PhCRR), a device consisting of a microring resonator upon which a photonic crystal structure is superimposed. Due to the periodic dielectric structure of the PhCRR, the gradient of the device's dispersion curve approaches zero near the photonic band edge, resulting in enhanced light-matter coupling and quality factors due to the low group velocity of the resonant modes. In order to fully exploit the "slow light" characteristics of the PhCRR, a design approach is used which allows for the selection of band edge resonant modes. A frequency domain computational approach models the dispersion of a periodic silicon photonic crystal waveguide. Boundary conditions are then imposed on the waveguide, ensuring the phase matching of propagating electromagnetic waves and the discreteness of the number of lattice cells in the ring. Through proper selection of design parameters, these geometric constraints return a set of resonant modes which fall precisely at the photonic band edge. Finite-difference time-domain simulations yield the field energy densities of the individual resonant modes of the PhCRR, with calculated quality factors greater than 10^7. The spectral features of the PhCRR and the effect of geometric disorder are explored. Finally, a design proposal for the silicon-on-insulator fabrication of on-chip photonic crystal ring resonators is discussed.

Acknowledgements

First of all, thank you to my thesis supervisor, Dr. Pablo Bianucci, for allowing me the opportunity to discover the field of photonics and for affording me the support and flexibility necessary to pursue my degree.

Thanks to my fellow research group members and office mates, Tabassom Hamidfar and Amir Hassanpour, for welcoming me into your folds and for tolerating an American in your midst.

Thanks to my sisters, for their lifetime of friendship and for the wonderful families they've built (and are building!)

Thanks to my parents, whose enthusiasm and encouragement have allowed me to accomplish far more than I ever imagined I could. Thank you for the countless hours that you have dedicated to reassuring my fears, sharing in my moments of success, and for proofreading my thesis!

Finally, to my husband David, our son Arthur, and our second child, whose arrival we eagerly await; thank you for making every single day better than the last.

Contents

List of Figures

List of Tables

To Elsie, for my inherited love of the scientific world and for teaching me from a young age that every step is simply about "putting one foot in front of the other".

To Barbara, for modelling determination, independence, grace, and spunk (and for knitting amazing sweaters).

To Dale, for demonstrating how work is not truly work if you love what you do.

To David, whose ability to live in the present has installed in me a lifelong appreciation for the natural world.

Chapter 1

Introduction

The electronic circuit has dominated the landscape of modern industry, paving the way for the emergence of revolutionary technologies such as the computer and the smart phone. However, the rapidly approaching limitations of electronic circuitry has opened the field for new innovations. In particular, increasingly high speed data transmissions over distances greater than 100 m are severely restricted due to the attenuation of data signals in electronic circuits. This limiting feature of electronic components has proven to be one of the main motivators for advancing the field of photonic signal processing.

Photonic circuits utilize the photon, rather than the electron, for information transfer, processing, and detection [1]. To date, the most prevalent photonic device in use is the fiber optics cable. A fiber optics cable is composed of optical fibers, which employ a refractive index contrast between the core and outer cladding layer to guide light along the length of the core. Optical fibers are capable of high speed transmissions of data on the order of 1 GB/s or greater over long distances with very little signal attenuation [2]. This disruptive technology has revolutionized the telecommunications industry and has demonstrated the future potential for growth of photonic devices in other fields. However, the proliferation of photonic circuits currently faces several fundamental obstacles, including:

1. **Regulation of light flow in integrated photonic circuits**:
   Photonic devices must offer a high degree of control over the propagation of light waves.

One photonic device which has shown particular promise in this respect is the **microresonator**. A microresonator is a photonic cavity whose dimensions are on the order of the wavelength of light [3]. Scaling of the microresonator's physical proportions allow the resonators to operate at a wide range of different frequencies.

2. **Miniaturization and integration of photonic devices**:
   In order for optical signal processing to contend with existing electronic circuit technologies, optical devices must be designed so as to allow for the miniaturization of on-chip photonic circuits. Furthermore, fabrication platforms must be found which facilitate the integration of photonic devices into low cost, mass reproducible circuits. One solution to these obstacles is to build upon current manufacturing technologies employed for the fabrication of electronic circuits.

Ensuing the dedication of substantial research and monetary resources to the optimization of electronic circuit fabrication, silicon manufacturing has emerged at the forefront of the current electronics industry. Transferring silicon manufacturing technologies to the photonics industry will allow us to capitalize on well-developed fabrication techniques already in place. In particular, the **silicon-on-insulator** (SOI) platform has shown considerable promise for the fabrication of integrated photonic circuits. The SOI platform utilizes a silicon microchip with a substrate layer of silica, upon which a thin layer of silicon is deposited. The high refractive index contrast between the thin silicon layer and its neighbouring silica layer allows for the miniaturization of optical features up to the sub-micron scale. Additionally, the SOI platform is compatible with current fabrication industry standards, allowing for the low cost, high throughput fabrication of reproducible photonic circuits. Most importantly, current telecommunications technologies utilize silicon and silica as the primary materials for the construction of optical fibers. Utilizing the SOI platform for the fabrication of photonic devices will facilitate the integration of photonic circuitry with existing telecommunications technologies.

Telecommunications devices operate predominantly at a wavelength of 1550 nm, corresponding not only to the transparency window of silicon but also to the lowest optical power attenuation rates of silica [4]. Photonic components operating in this range of frequencies are of notable interest due to their compatibility with said devices. Accordingly, the past few decades have

seen an upsurge in research devoted to micron or sub-micron scale microresonators. Microresonators of this scale operate in the infrared region of the electromagnetic spectrum and are thus congruent with telecommunications technologies.

One particular type of microresonator which has emerged as a fundamental component of integrated photonic circuits is the **microring resonator**. Similar to the optical fiber, a ring resonator utilizes the refractive index contrast of its constituent materials to confine an electromagnetic wave to its core. Under certain conditions, a propagating light wave in a ring resonator will interfere constructively as it performs multiple circuits of the ring. As a result, ring resonators allow for the buildup of high intensity, localized electric fields. This effect can result in strong interactions between the electromagnetic fields and the surrounding material. Strong coupling between light and matter in a microresonator paves the way for the exploration of quantum cavity electrodynamics phenomena [5], with applications in quantum information technology [6]. Strong light-matter coupling can also facilitate the observation of optical nonlinear effects [7, 8].

In addition, if a ring resonator possesses low optical losses, the spectral fingerprint of the resonator will display particularly narrow resonances. Ring resonators exhibiting such features have shown interesting potential for use as narrow-band optical filters [9]. A microresonator allows for the selective optical power transfer of resonant frequencies from one port of a photonic circuit to another, effectively extinguishing said frequencies from the input port of the circuit [10]. Microring resonators possessing narrow spectral features have also proven to be useful as sensitive bio-detection devices [11]. In recent years, ring resonators have been put to commercial use for the detection of infectious diseases and various cancers [12].

The features of a standard ring resonator can be improved upon by tailoring the properties of the resonator so that the velocity of a light wave is significantly slowed as it propagates through the resonator. **Slow light** is a phenomenon which has proven particularly interesting in recent decades. Specifically, slow light electromagnetic waves in microresonators have been shown to have enhanced light-matter interactions and low optical losses. Thus, the generation of slow light characteristics in ordinary ring resonators stands to improve upon the existing technologies already discussed.

Slow light can be introduced into a system in one of two ways [13]. Designer materials can be utilized, which have been tailored to slow light waves as they propagate through the material. However, a more versatile approach is to control the velocity of light via geometric structuring alone. Such a technique allows slow light characteristics to be introduced into commonly used materials, such as silicon, which are readily available and easy to work with. The most promising approach in producing slow light electromagnetic waves is via use of a **photonic crystal** (PhC). A photonic crystal possesses a periodic dielectric structure in one or more dimensions. Interaction of the light wave with the multiple dielectric interfaces formed by the periodic structure of the material can result in a reduction of a light wave's velocity.

The interesting spectral features of ring resonators can be merged with the properties of slow light devices by superimposing a photonic crystal structure onto a standard ring resonator to form a **photonic crystal ring resonator** (PhCRR). The core of this thesis will be committed to exploring how photonic crystal ring resonators can be designed so as to enhance light-matter interactions and lower optical losses of the resonator. The following three chapters are dedicated to laying down a theoretical foundation describing the characteristics of microresonators, photonic crystals, and slow light electromagnetic waves. A novel design approach allowing for the precise selection of slow light resonant modes is then presented, followed by a chapter dedicated to the computational verification of the validity of the design. The SOI fabrication of photonic crystal ring resonators is explored in Chapter 7, followed by a concluding discussion on future applications and research in the field.

Chapter 2

Dielectric waveguides and ring resonators

Microresonators rely on two main mechanisms in order to control the propagation of electromagnetic waves [3]. The first depends on reflection of the wave from a boundary formed by the interface of two dielectric materials, a process which is dictated by the law of total internal reflection. The second means by which to control the propagation of light is via periodic patterning of the dielectric material used to construct the microresonator. This chapter is devoted

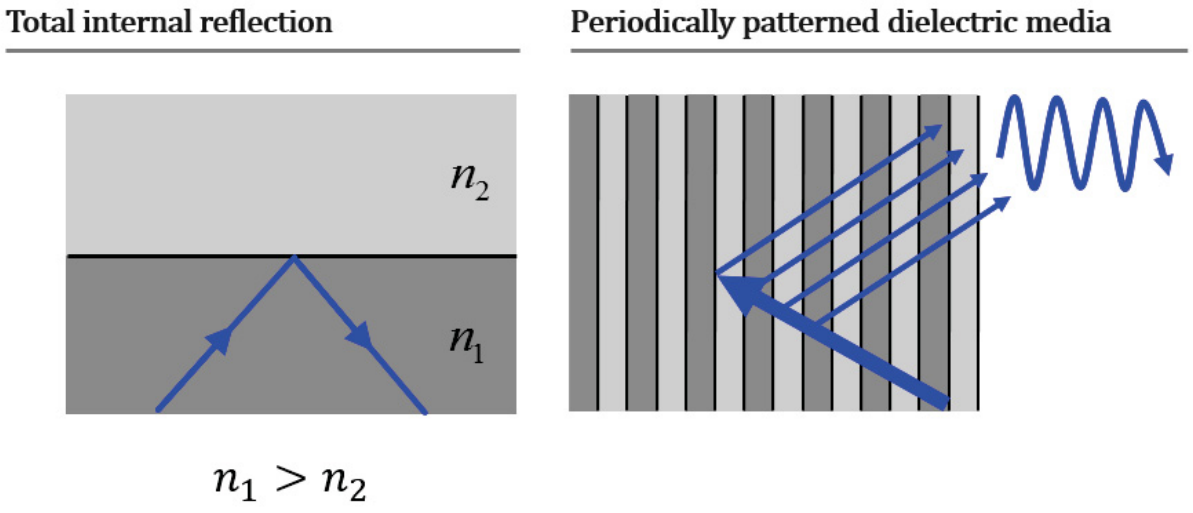

FIGURE 2.1: (a) Total internal reflection at a dielectric interface. (b) A periodically patterned dielectric structure.

to developing a deeper comprehension of total internal reflection and the two main types of microresonators which employ this process; the dielectric waveguide and the ring resonator.

2.1 Total Internal Reflection

To fully understand total internal reflection, we start by examining the behaviour of an electromagnetic wave at a dielectric interface. At the boundary between two materials of refractive indices n_1 and n_2, a portion of an incident wave is partially transmitted through the interface, while the remaining portion of the wave is reflected. In order to precisely determine the angles at which the transmitted and reflected fields will propagate, one must apply **Snell's law** [14].

$$n_1 \sin(\theta_R) = n_2 \sin(\theta_T) \tag{2.1}$$

where θ_R and θ_T are the reflected and transmitted angles, respectively.

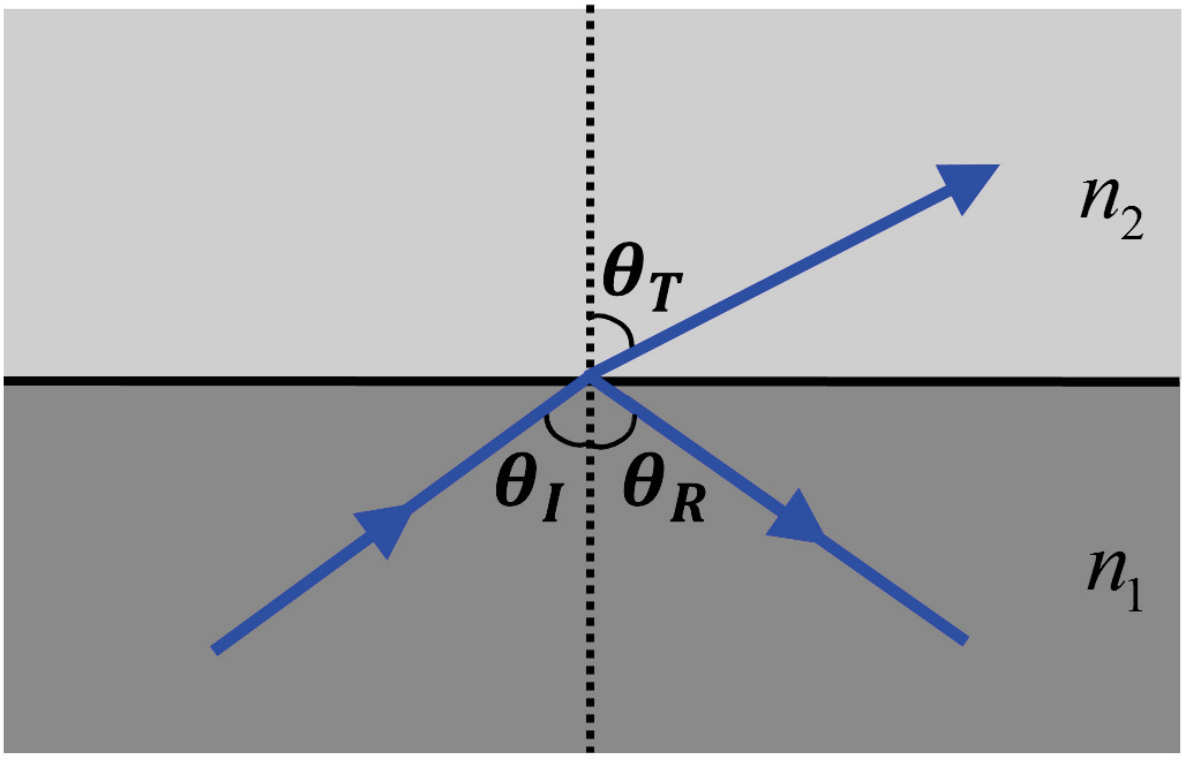

FIGURE 2.2: Reflection and transmission of an incident electromagnetic wave at a dielectric interface, as dictated by Snell's law.

If the wave is traveling from a high refractive index material to a low refractive index material with an incident angle larger than the **critical angle**, defined as $\theta_C = \sin^{-1}\left(\frac{n_2}{n_1}\right)$, the light will be **totally internally reflected** at the interface. In such cases, no energy flow is allowed to traverse the dielectric interface but, rather, is strictly confined to the high index material. It can thus be stated that the intensity of the incident and reflected electromagnetic waves are equivalent [15]. More precisely, the amplitudes of the incident and reflected electric fields can be related by:

$$|E_I|^2 = |E_R|^2 \tag{2.2}$$

While the intensities of the incident and reflected waves are invariant upon reflection from the dielectric interface, the wave will experience a phase shift. This change in phase, known as the **Goos-Hänchen effect** [14], can be described as:

$$E_R = E_I e^{2i\Phi}$$

where $\tan\Phi = \frac{+\sqrt{{n_1}^2 \sin^2\theta_I - {n_2}^2}}{n_1 \cos\theta_I}$.[1].

Despite the fact that the energy of the electromagnetic field is completely reflected at the dielectric interface, an electromagnetic wave can be found in the lower refractive index material. The transmitted wave, known as the **evanescent field**, will propagate parallel to the surface of the interface, with an exponentially decaying amplitude which will attenuate to negligible values within a few wavelengths of distance from the boundary (see Appendix A for more details).

2.2 Dielectric Waveguides

A dielectric **waveguide** is a microresonator which utilizes total internal reflection to guide light and energy in a specified direction. A waveguide is formed by interposing a film of material of

[1]The definition of Φ is to be applied solely to fields whose electric field is perpendicular to the direction of propagation. For fields whose magnetic field is perpendicular to the direction of propagation, one must use $\tan\Phi = \frac{{n_1}^2}{{n_2}^2}\frac{\sqrt{{n_1}^2 \sin^2\theta_I - {n_2}^2}}{n_1 \cos\Theta_I}$

FIGURE 2.3: A dielectric waveguide composed of a film of high refractive index material, n_f, surrounded by low index cladding and substrate materials.

refractive index, n_f, between a substrate and cladding material, of refractive indices n_s and n_c respectively (see Figure 2.3).

In order for an electromagnetic wave to be "guided" through the film, we must require that $n_f > n_c$ and $n_f > n_s$. Once the materials utilized to construct the dielectric waveguide have been selected, we can define two separate critical angles:

$$\begin{aligned} \theta_{C_1} &= \sin^{-1}\left(\frac{n_c}{n_f}\right) \\ \theta_{C_2} &= \sin^{-1}\left(\frac{n_s}{n_f}\right) \end{aligned} \tag{2.4}$$

The first, θ_{C_1}, is defined as the minimum incident angle required for an electromagnetic wave to be totally internally reflected from the film/cladding interface, while θ_{C_2} describes the analogous incident angle for the film/substrate interface.

Three different types of modes can be described in a dielectric waveguide (see Figure 2.4). A **radiation mode** describes an electromagnetic wave which is transmitted from the substrate into the film, but fails to strike the film/cladding interface at an angle exceeding the critical angle, θ_{C_1}. Consequently, a portion of the energy transport of the wave is necessarily transmitted through the interface where it will be lost to the cladding material.

The second type of mode satisfies the critical angle condition for the film/cladding interface, however strikes the film/substrate interface at an angle of incidence less than θ_{C_2}. Similar to a radiation mode, the energy density of the light wave will leak into the substrate material and is thus known as a **substrate mode**.

Finally, a **guided mode** is an electromagnetic wave whose incident angles at both the film/substrate and film/cladding interfaces exceed the critical angles defined in Eq. (2.4). In this case, the wave is totally internally reflected along the length of the film's core, confining the energy transport of the field to the high refractive index material. The greater the contrast between the refractive index of the film and its surrounding materials, the greater the confinement of the propagating wave. As was stated in Section 2.1, finite, exponentially decaying evanescent waves will be found in both the cladding and substrate materials.

Guided modes traveling through a waveguide can either propagate along the length of the high index film's core (defined here in Figure 2.3 as the $+\hat{z}$-direction) or in the opposite sense. The direction of propagation of the wave is determined by its wave vector, $\mathbf{k} = \frac{2\pi}{\lambda}\hat{\mathbf{r}}$, whose magnitude quantifies the phase change of the electromagnetic wave per unit length of propagation. Depending on the phase difference between the two counter-propagating waves, the field patterns will constructively or destructively interfere. In the case of constructive interference, the superposition of the two waves results in a standing wave field pattern of the guided modes in the $\hat{x}-$direction of the waveguide.

The standing wave field configurations depend on several different factors. Consider a single point on the standing wave form which is oscillating between the $+\hat{x}$-direction and the -$\hat{x}$-direction. As discussed in Section 2.1, when a wave is totally internally reflected at the film/-cladding interface, the wave will undergo a phase change, Φ_C. Similarly, a wave will undergo a second phase change, Φ_S, upon total internal reflection from the film/substrate interface. The wave will also experience a phase shift as it propagates the distance between the cladding and substrate interfaces. The total phase change experienced by the wave is thus given by:

$$\Phi_{total} = 2|\mathbf{k}|n_f h\cos\theta_I - 2\Phi_C - 2\Phi_S \tag{2.5}$$

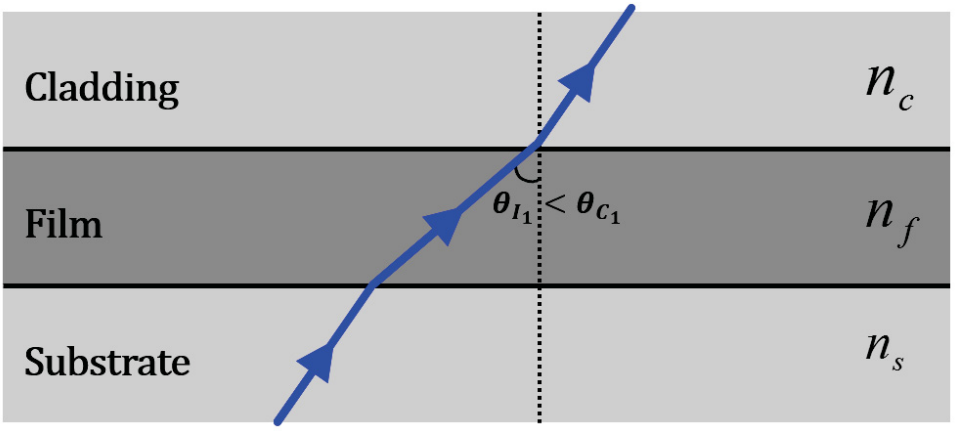

(A) A radiation mode: the electromagnetic wave strikes the cladding/film interface at an incident angle less than the critical angle θ_{C_1}.

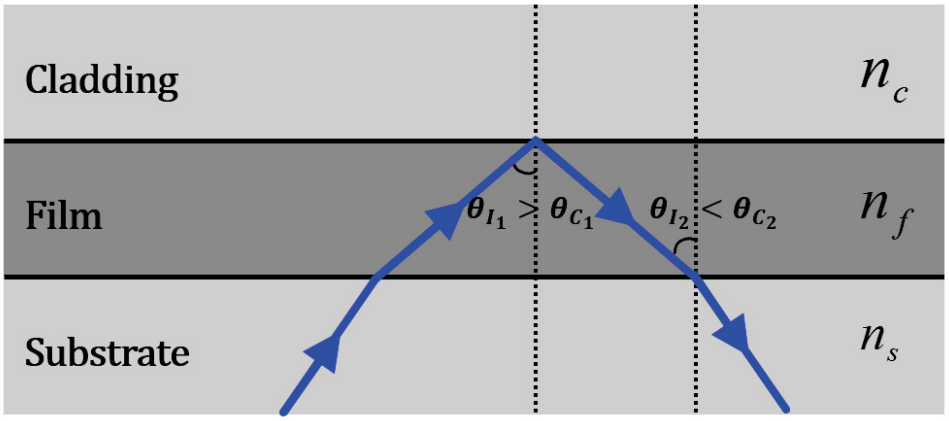

(B) A substrate mode: the electromagnetic wave is totally internally reflected at the cladding/film interface. However, the incident angle of the wave at the film/-substrate interface is less than the critical angle, θ_{C_2}, required for total internal reflection.

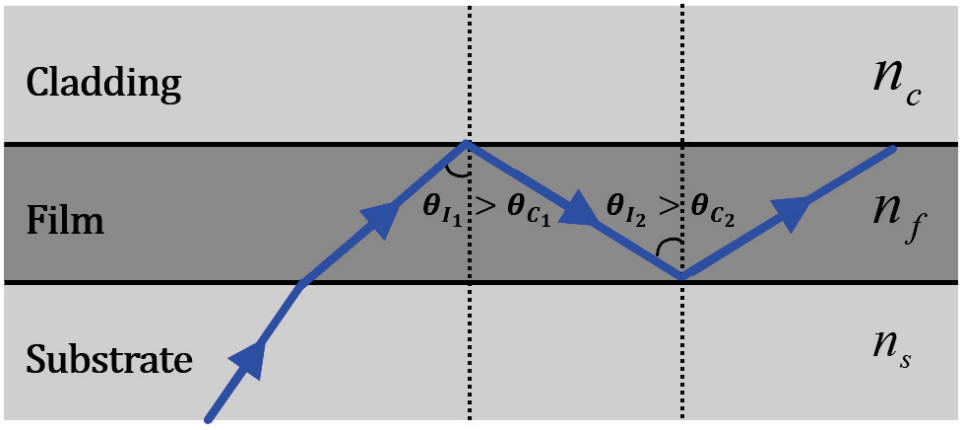

(C) A guided mode: the electromagnetic wave's incident angles at both the cladding/film and film/substrate interfaces satisfy the conditions required for total internal reflection. The wave is accordingly guided along the length of the film's core.

FIGURE 2.4: Three different electromagnetic waves in a dielectric waveguide

where h is the thickness of the waveguide and θ_I is the incident angle of the wave. In order for constructive interference to occur, we must require Eq. (2.5) to satisfy the following condition:

$$2|\mathbf{k}|n_f h\cos\theta_I - 2\Phi_C - 2\Phi_S = 2\pi m \tag{2.6}$$

where m is a positive integer. Equation (2.6) defines a discrete set of incident angles which satisfy the phase matching requirement for a propagating guided mode. Consequently, only waves incident on the waveguide with an angle, θ_I, belonging to this set may propagate through the waveguide. Alternatively, waves possessing incident angles falling outside the discrete spectrum of allowable angles will be extinguished in the waveguide via destructive interference.

Each integer value m satisfying Eq. (2.6) characterizes a guided mode of the dielectric waveguide. The **fundamental mode** of a waveguide corresponds to the wave possessing the mode number $m = 0$. This electromagnetic wave will have the lowest frequency of any guided mode allowed by the waveguide. One can also see from Eq. (2.6) that as the thickness of the film, h, increases, an increasing number of values of m will satisfy the phase matching condition. A waveguide which allows for numerous guided modes to propagate through the film material is known as a **multi-mode waveguide**. The electromagnetic field configuration of a multi-mode waveguide represents the linear combination of several field configurations corresponding to various different mode numbers. It is often desirable to restrict the allowable guided modes of the waveguide to a single mode (known, accordingly, as a **single-mode waveguide**). This result can be achieved by limiting the thickness of the film so that only a singular mode number satisfies Eq. (2.6). In general, a waveguide is classified as single-mode when its thickness is on the order of half a resonant wavelength [16].

As was briefly mentioned in the introduction, an excellent example of a high index contrast material platform is silicon-on-insulator. The index contrast between the silicon, the silica-based insulating layer, and the surrounding cladding material (air or silica) allows for total internal reflection of the wave through the silicon core. The index contrast also tightly confines the field to the silicon core, allowing for very small waveguide dimensions on the order of 400 nm or less.

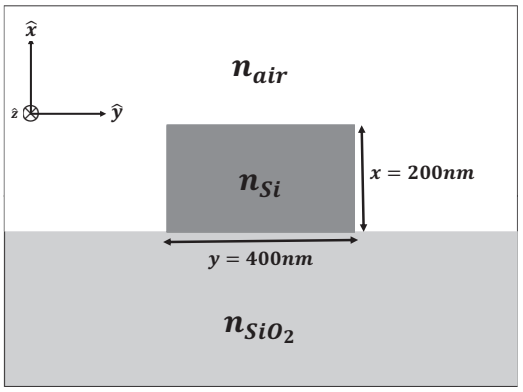

(A) The geometry of a dielectric waveguide constructed on the SOI platform. A high refractive index silicon core ($n_{SI} = 3.48$) is placed on a SiO_2 layer ($n_{SiO_2} = 1.44$). The cladding material is generally composed of silica or air ($n_{air} = 1.00$). The high refractive index contrast between the silicon core and the surrounding materials allows for very small core dimensions.

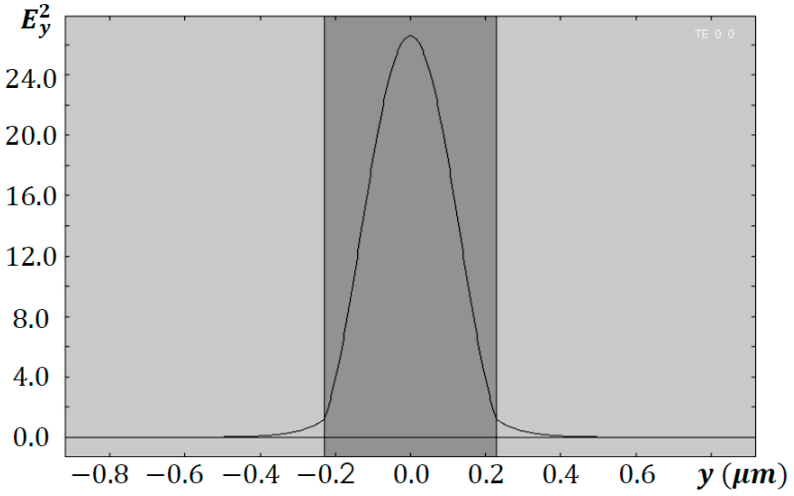

(B) The intensity, $|E_y|^2$, of the fundamental mode of the silicon waveguide as a function of the horizontal direction, y. Here we consider in-plane polarization of the electric field. The high refractive index contrast of the SOI platform results in strong confinement of the electric field to the silicon core.

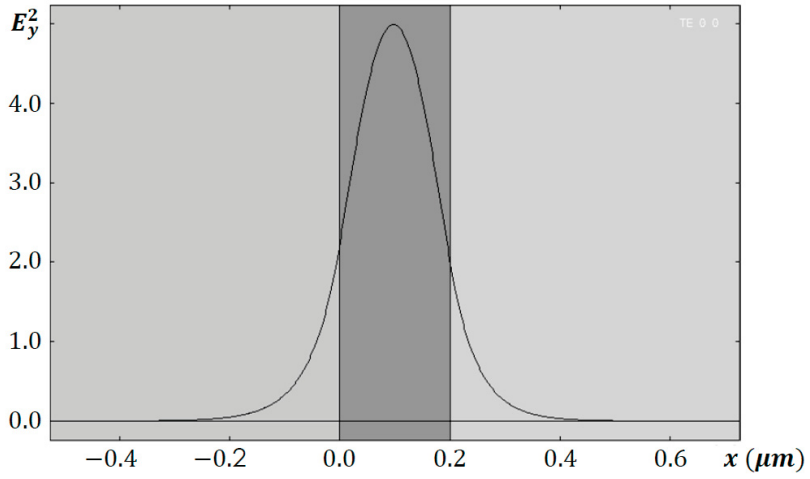

(C) The intensity, $|E_y|^2$, of the fundamental mode of the silicon waveguide as a function of the vertical direction, x. Similar to the horizontal confinement, the electric field intensity is largely concentrated in the high refractive index silicon core. However, the smaller dimension in the vertical direction, as compared to the horizontal direction, results in higher optical losses.

FIGURE 2.5: The geometry and electric field intensities of a silicon waveguide of core dimensions 400 × 200 nm on a silica substrate.

Figures 2.5b and 2.5c show how the intensity of the electromagnetic field is restricted in the horizontal and vertical directions, while allowing for propagation along the length of the core. It also demonstrates how the smaller the dimensions of the device, the more tightly the guided mode is confined to the silicon core. However, small core dimensions can also result in higher optical losses, as can be seen in the mode profile depicting the vertical confinement of the guided modes. The tails of the intensity curves are not restricted to the core but, rather, behave as evanescent waves which will decay into the cladding material.

2.3 Chromatic Dispersion

Chromatic dispersion describes the dependency of an electromagnetic wave's frequency on its wave vector. As an electromagnetic wave propagates through a dielectric waveguide, it will experience two different types of chromatic dispersion.

A polychromatic electromagnetic wave packet traveling through the empty space of vacuum travels at a velocity of $c \equiv 3.00 \times 10^8$ m/s. Alternatively, the velocity of an equivalent wave packet in a material of refractive index n will be altered as the propagating pulse interacts with the constituent particles of the material. This velocity modification varies for waves of differing frequencies, causing each component of the wave packet to propagate at different velocities. This effect, known as **material dispersion**, depends on the unique composition of a material and is discussed further in the following section.

An alternative, but equally impactful, type of chromatic dispersion is **waveguide dispersion**. Waveguide dispersion describes how an electromagnetic wave interacts with the dielectric interfaces of a waveguide. The geometric restrictions imposed by the non-homogeneity of the waveguide's composing materials can additionally alter the velocities of waves of different frequencies. Section 2.3.2 is devoted to further developing this concept.

2.3.1 Material Dispersion

We start our discussion on material dispersion by considering a plane wave in a homogeneous, non-magnetic material [15]. The wave is linearly polarized along the $+\hat{z}$-direction, so that the

complex field amplitude of the wave can be described as $\mathbf{E} = (E_x, E_y, E_z) = (0, 0, E_z)$. We consider the wave to be propagating in the $+\hat{x}$-direction with a wave vector $\mathbf{k} = (+k_x, 0, 0)$. The electric field of such a wave is described as:

$$E_z(x,t) = E_z e^{-i(k_x x - \omega t)} \tag{2.7}$$

where ω is the angular frequency of the wave. We will now express the wave vector in terms of a real and imaginary part [14]:

$$k = \beta + i\frac{\alpha}{2} \tag{2.8}$$

Plugging Eq. (2.8) into Eq. (2.7) yields:

$$E_z(x,t) = E_z e^{-i((\beta + i\frac{\alpha}{2})x - \omega t)} = E_z e^{-i(\beta x - \omega t)} e^{-\frac{\alpha x}{2}} \tag{2.9}$$

Examining this equation, we see that the first exponential function represents a propagating plane wave, while the second term describes a decaying exponential function. This second term, $e^{-\frac{\alpha x}{2}}$, quantifies the rate at which the intensity of the electromagnetic plane wave decays. The decay rate is determined by the imaginary part of the wave vector, α, and is most commonly known as the intensity absorption coefficient. This coefficient is determined by the absorption qualities of a particular material.

If we choose to neglect absorption losses of the material, we can consider only the real part of the wave vector of the electromagnetic wave, β, known as the propagation constant. If we reexamine Eq. (2.9) by setting $\alpha = 0$ and dividing the argument of the exponent by β we find:

$$E_z(x,t) = E_z e^{-i(x - \frac{\omega}{\beta} t)} \tag{2.10}$$

We see immediately that the velocity of the propagating wave is quantified by the term $\frac{\omega}{\beta}$. Thus, deriving an expression for β will provide valuable information concerning the behaviour of an electromagnetic wave in a non-absorptive and non-magnetic material.

A comprehensive derivation (see Appendix B) yields the result:

$$\beta = \frac{2\pi n}{\lambda} \tag{2.11}$$

Using the relations $\beta = \mathrm{Re}(k)$ and $c = \frac{\lambda\omega}{2\pi}$, Eq. (2.11) can be rewritten in what is known as the **dispersion relation**.

$$\omega = \frac{ck}{n} \tag{2.12}$$

We can also define the velocity of the electromagnetic wave by dividing ω by Eq. (2.11):

$$v = \frac{\omega}{\beta} = \frac{\omega}{\frac{2\pi n}{\lambda}} = \frac{c}{n} \tag{2.13}$$

Eq. (2.13) tells us that the velocity of the wave is determined by the ratio of the speed of light in vacuum to the refractive index of a material. Thus the refractive index of a material quantifies the rate by which the velocity of an electromagnetic wave is slowed by a material, due to interactions with the constituent particles of the material. By examining Eq. (2.12) we also see that the wave vector of an electromagnetic wave is related to its frequency by the proportionality factor $\frac{c}{n}$, defined as the velocity of the propagating wave.

If the refractive index of the material is independent of wavelength, the dispersion relation described by Eq. (2.12) is linear. A material possessing a linear dispersion relation is considered to be non-dispersive, implying that every frequency of light traveling through the material will travel at a constant velocity. For example, an electromagnetic wave packet propagating through vacuum does not experience dispersion, as free space possesses a wavelength-independent refractive index of $n = 1$. Thus, *all* electromagnetic waves traveling through vacuum will possess the same velocity, c, regardless of the frequency of the wave.

However, if the refractive index of the material is wavelength dependent or, equivalently, wave vector dependent (i.e. $n = n(\lambda)$) the dispersion relation of the material is decidedly non-linear. The velocity of the wave now depends on wavelength, causing electromagnetic waves of different frequencies to propagate at different velocities. Depending on the particular properties

of the material, an electromagnetic wave packet will either spread out or compress as it moves through the material. A material possessing a wavelength-dependent refractive index is known as **dispersive**.

2.3.2 Waveguide Dispersion

We now turn our focus to an electromagnetic wave propagating through a dielectric waveguide. The material can no longer be described as homogeneous, as the refractive indices of the film, cladding, and substrate must satisfy the condition $n_f > n_c \geq n_s$ in order for wave guiding of light to occur. The non-uniformity of the material seen by a guided mode results in a second type of chromatic dispersion experienced by the propagating wave, known as waveguide dispersion.

As seen in Section 2.2, the individual geometric properties of the waveguide structure impose certain conditions on a propagating light wave. The allowable modes of a waveguide are required to have an incident angle belonging to a discrete set of values, as is defined by Eq. (2.6). In contrast, an electromagnetic wave propagating through a homogeneous material with no restricting geometric features can possess an incident angle belonging to a continuous range of incident angle values. Consequently, the propagation constant of a light wave moving through a waveguide depends not only on the properties of the material, but on the allowable mode profiles which are guided by the waveguide.

The propagation constant of an electromagnetic wave in a waveguide is given by [15]:

$$\beta = \frac{2\pi n_{eff}}{\lambda_0} \tag{2.14}$$

Here the material refractive index, n, has been replaced by the **effective refractive index**, n_{eff}, and λ_0 is defined as the vacuum wavelength of the wave in question. The effective refractive index describes the rate by which the speed of light is slowed by both the material and the geometric properties of the waveguide. Not only will the propagating wave interact with the constituent particles of the material, but will now also experience reflections off of the dielectric interfaces formed by the geometric boundaries of the waveguide. If we apply the relation $k_0 = \frac{2\pi}{\lambda_0}$ to Eq. (2.14), the effective refractive index can be defined as:

$$n_{eff} = \frac{k}{k_0} \tag{2.15}$$

The effective refractive index of a waveguide is most commonly determined through a computational approach. Once the geometry and composing materials of a waveguide have been defined, the mode profiles of the waveguide are calculated by numerical means. The wave vector of the guided mode is then compared to the wave vector of the propagating wave in vacuum via Eq. (2.15) to solve for the effective refractive index.

2.4 Ring resonators

In addition to the waveguide, a second common photonic device utilizing total internal reflection is the ring resonator. As in a waveguide, total internal reflection confines the light inside the ring resonator, provided that the incident angle of the electromagnetic wave is larger than the critical angle and that the refractive index of the core of the ring resonator is larger than that of its surrounding materials. While in theory, total internal reflection can only truly occur when the dielectric interface encountered by a propagating electromagnetic wave is perfectly flat, in practice a radius of curvature $R > \frac{\lambda_0}{n_{eff}}$ is sufficient to appreciably reduce optical bending losses.

If phase matching of an electromagnetic wave in the ring resonator occurs, the light will constructively interfere in the resonator as it performs multiple circuits of the ring [17]. This allows for the buildup of high intensity electric field configurations at the resonant wavelengths, λ_m, of the device. The phase shift of an electromagnetic wave traveling through the ring resonator is described by:

$$\Phi = k \cdot n_{eff} \cdot 2\pi R \tag{2.16}$$

where R is the radius of the ring resonator. To ensure phase matching of the resonant mode, we must require the overall phase shift experienced by a light wave in the resonator be restricted to integer values of 2π:

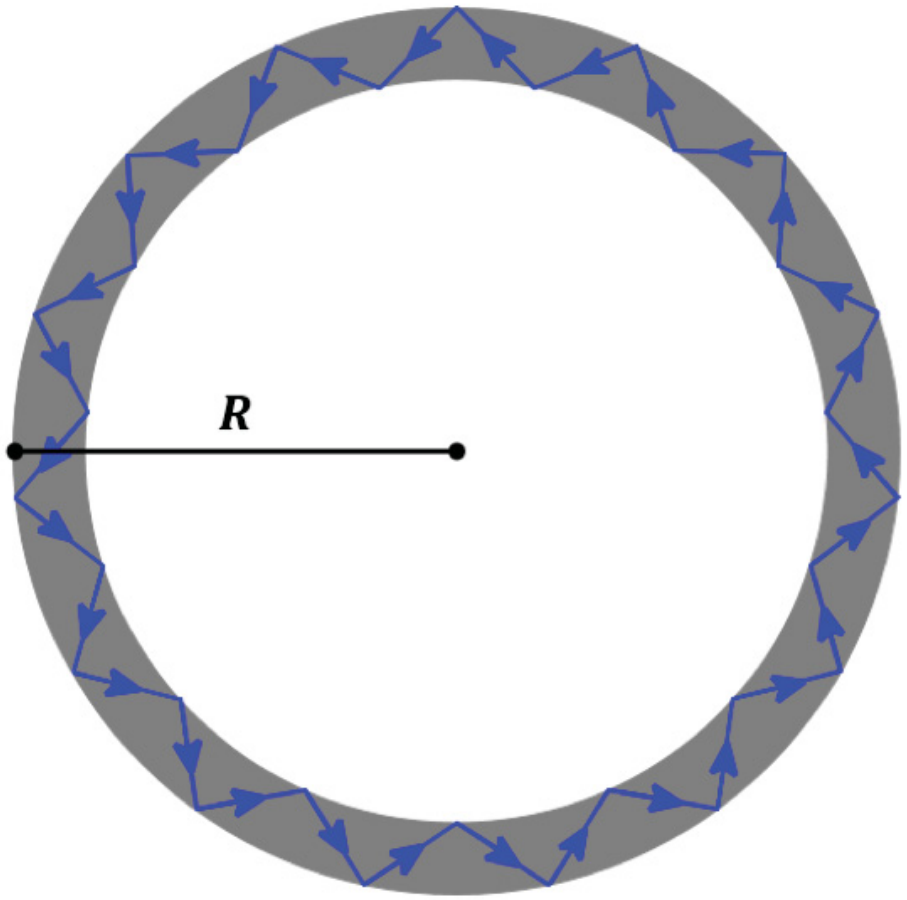

FIGURE 2.6: A ring resonator of radius R with a high effective refractive index core, n_{eff}, (indicated in grey) surrounded by low index cladding (indicated in white). A propagating electromagnetic wave is totally internally reflected at the dielectric interfaces formed by the ring resonator's boundaries with the surrounding cladding material.

$$\Phi = 2\pi m \tag{2.17}$$

where $m \in \mathbb{Z}$.

Combining Eqs. (2.16) and (2.17) yields a description of precisely where the resonant wavelengths of the device can be found:

$$\lambda_m = \frac{2\pi R \cdot n_{eff}}{m} \tag{2.18}$$

The spectral profile of a ring resonator will demonstrate peak intensities at these resonant wavelengths due to the constructive interference of propagating light waves.

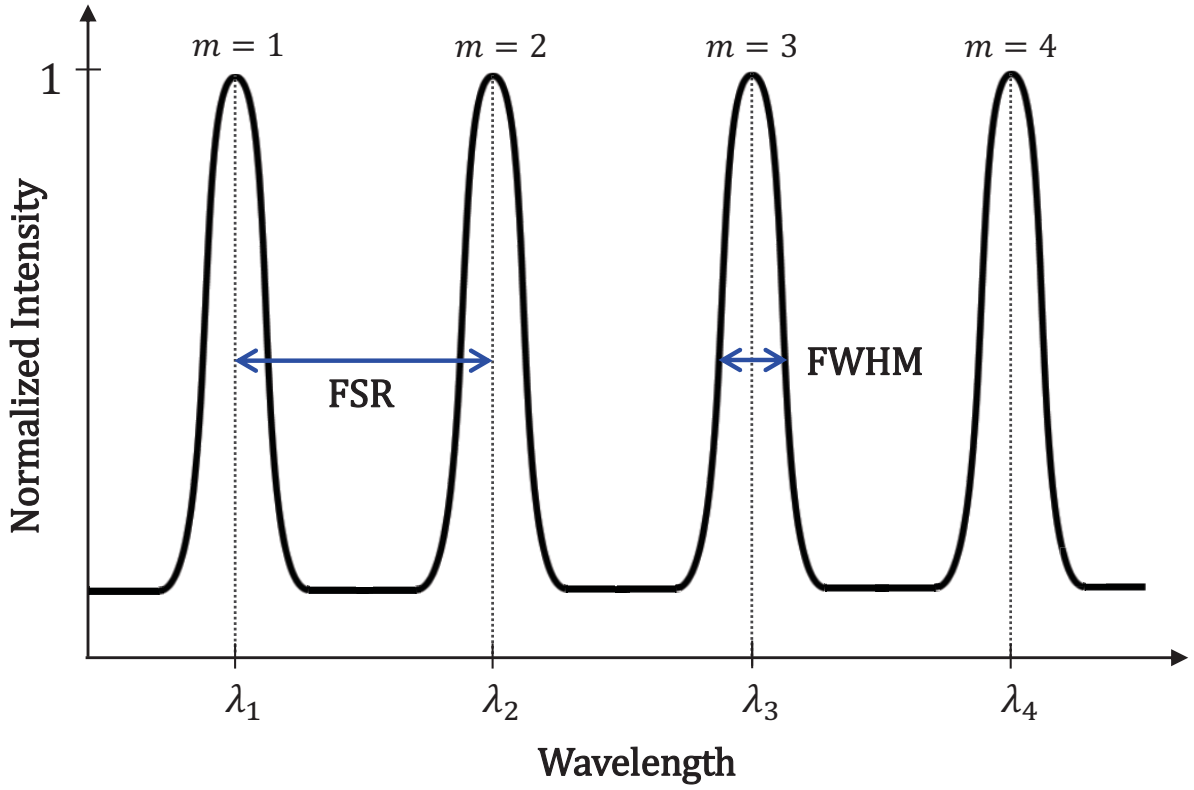

FIGURE 2.7: The spectral profile of a ring resonator. The ring resonator exhibits peak intensities at its resonant wavelengths, λ_m

2.4.1 Attributes of microresonators

When discussing microresonators, we refer often to several quantities describing specific attributes of the resonator. The **free spectral range** (FSR) of a microresonator is defined as the difference between the wavelengths of two adjacent resonant conditions, m and $m+1$:

$$FSR = \Delta\lambda = \lambda_{m+1} - \lambda_m \tag{2.19}$$

For a ring resonator, consecutive modes are all equidistantly spaced, signifying that the free spectral range of a ring resonator is constant for all m and $m+1$ pairings.

Secondly, the optical loss of a microresonator is quantified by its **quality factor**, Q. The quality factor of a resonant mode is proportional to the lifetime of a photon in the optical cavity and is defined by:

$$Q = \frac{\lambda}{FWHM} \tag{2.20}$$

where $FWHM$ refers to the full width, half maximum of a resonant mode. As can be seen in Eq. (2.20), the quality factor of a mode is inversely proportional to the FHWM of the resonance, implying that a narrow resonance in the frequency domain corresponds to a low loss cavity. This relation can also be thought of in terms of a Fourier analysis: the Fourier transform of a frequency-domain resonance is the equivalent resonance in the time-domain. Accordingly, a narrow resonance peak in the frequency space corresponds to a photon with a long lifetime. Typical high quality microresonators have a Q-factor on the order of 10^6 [18].

Chapter 3

Periodically Patterned Dielectric Structures

Periodically patterned dielectric structures offer an alternative means by which to control the propagation of electromagnetic waves in a microresonator. These structures, more commonly known as photonic crystals, possess a periodic dielectric function. An electromagnetic wave traveling through a photonic crystal encounters multiple dielectric interfaces, at which the wave can either be transmitted or reflected. Reflections off of multiple interfaces interfere with each other, allowing only certain frequencies of light to propagate through the photonic crystal [3].

Photonic crystal electromagnetics phenomena have many similarities to occurrences in solid state physics. In particular, Bloch's theorem describes the behaviour of an electron traveling through a crystal lattice of ions [19]. The electron experiences a periodic potential which can be described as:

$$U(\mathbf{r} + \mathbf{R}) = U(\mathbf{r}) \tag{3.1}$$

where $\mathbf{r}$ corresponds to the position vector and $\mathbf{R}$ is the lattice vector quantifying the distance between two adjacent ions. If the wave function of the electron satisfies certain conditions, the

electron can propagate through the periodic potential of the underlying lattice of ions with a non-zero mean velocity. This implies that the electrons are *not* scattered via Coulomb interactions with the lattice of ions but, rather, travel through the lattice undisturbed.

Because the characteristic length scales of a typical crystal lattice ($\sim 1\mathring{A}$) are on the order of, or less than, the DeBroglie wavelength of a free electron, a quantum mechanical analysis of the behaviour of the electron is required. The generalized equation for a single electron is given by Schrödinger's equation:

$$\left(-\frac{\hbar^2}{2m}\nabla^2 + U(\mathbf{r})\right)\Psi = E\Psi \tag{3.2}$$

In a periodic potential, such as the potential defined in Eq. (3.1), the wave function of a Bloch electron which satisfies Schrödinger's equation is described as:

$$\Psi(\mathbf{r}) = e^{i(\mathbf{k}\cdot\mathbf{r})}u(\mathbf{r}) \tag{3.3}$$

where $\mathbf{k}$ is the wave vector of the Bloch electron. The term $u(\mathbf{r})$ represents a function which follows the periodicity of the lattice potential, namely:

$$u(\mathbf{r} + \mathbf{R}) = u(\mathbf{r}) \tag{3.4}$$

Eq. (3.3) tells us that a Bloch electron behaves very similarly to a free electron propagating through free space. However, rather than propagating simply as a plane wave of the form $e^{i(\mathbf{k}\cdot\mathbf{r})}$, the wave function of the Bloch electron is modified by a periodic spatial function $u(\mathbf{r})$ which conforms to the periodicity of the underlying lattice ion potential. This characteristic sets Bloch electrons apart from free electrons and allows them to avoid scattering as they propagate through the lattice.

In parallel, photonic crystal electromagnetics considers a photon propagating through a mixed dielectric material that possesses a periodic dielectric function, $\epsilon_r(\mathbf{r})$. Similar to Eq. (3.1), the dielectric function (also known as the relative permittivity[1]) must satisfy the condition:

$$\epsilon(\mathbf{r}) = \epsilon(\mathbf{r} + \mathbf{a}) \tag{3.6}$$

where $\mathbf{a}$ represents the lattice vector quantifying the periodicity of the mixed dielectric material. Akin to Bloch's theorem for electrons in a periodic potential, photons in a periodic photonic crystal that satisfy certain conditions can propagate through the material undisturbed. In addition, photonic crystals can be designed so as to completely prohibit the propagation of certain electromagnetic frequencies.

3.1 Electromagnetics Master Equation

In order to understand these unique qualities of periodically patterned dielectric structures, we must start with an examination of precisely how a photon interacts with mixed dielectric media. In solid state physics, the phenomenon of the propagation of undisturbed Bloch electrons is dictated by Schrödinger's equation. In a photonic crystal, however, the behaviour of a photon is explained by **Maxwell's equations** [21]:

$$\nabla \cdot \mathbf{D} = \rho \qquad \nabla \cdot \mathbf{B} = 0 \tag{3.7a}$$

$$\nabla \times \mathbf{E} + \frac{\partial \mathbf{B}}{\partial t} = 0 \qquad \nabla \times \mathbf{H} - \frac{\partial \mathbf{D}}{\partial t} = \mathbf{J} \tag{3.7b}$$

Here, Maxwell's equations are expressed in terms of the macroscopic electric and magnetic induction fields, $\mathbf{E}$ and $\mathbf{B}$, the electric displacement field, $\mathbf{D}$, the magnetic field $\mathbf{H}$, and the free

[1] Here the relative permittivity is defined as the ratio of a material's permittivity, ϵ, to the vacuum permittivity, ϵ_0 [20]:

$$\epsilon_r(\mathbf{r}) = \frac{\epsilon}{\epsilon_0} \tag{3.5}$$

As per convention, we will from here on denote the relative permittivity as $\epsilon(\mathbf{r})$.

charge and current densities, ρ and $\mathbf{J}$. For most dielectric materials that we wish to consider, there are several reasonable approximations which can be made:

1. There exists no free charge or current sources within the mixed dielectric material. As a result, we can set the free charge and current densities, ρ and $\mathbf{J}$, equal to zero.

2. We consider only low power field strengths, allowing us to consider the materials in question as **linear media**. In general, the components of the electric displacement field may be expressed as a power expansion in terms of the electric field:

$$\frac{D_i}{\epsilon_0} = \sum_j \epsilon_{ij} E_j + \sum_{j,k} \chi_{ijk} E_j E_k + O(E^3) \tag{3.8}$$

   where χ_{ikj} are components of the electric susceptibility tensor, ϵ_0 is the vacuum permittivity, and D_i, E_j, and E_k represent various components of the displacement and electric fields. In the linear regime, the strength of the electric field is low enough that we can safely neglect the higher order terms of the power series and express the electric displacement field as linearly proportional to the electric field:

$$D(\mathbf{r}) = \epsilon_0 \epsilon(\mathbf{r}) E(\mathbf{r}) \tag{3.9}$$

3. We will assume that the dielectric materials under consideration are **transparent**, signifying that the absorption coefficients of the material are negligible. For example, the semiconductor band gap of silicon at 300K is equal to 1.11 eV. Microresonators compatible with current telecommunications technologies employ wavelengths on the order of 1550 nm. Such an electromagnetic wave has approximately 0.8 eV of energy and is thus not energetic enough to be absorbed by the material. As a result, silicon can be considered as transparent for the wavelengths in question.

4. Our fourth approximation assumes that the material in question is non-magnetic, indicating that the magnetic susceptibility of the material, χ_m, is negligible. As a result the material permeability is essentially equal to the permeability of free space, μ_0 [20]:

$$\mu \equiv \mu_0(1 + \chi_m) \cong \mu_0 \tag{3.10}$$

Similar to the relative permittivity (Eq. (3.5)), we can define the relative permeability as:

$$\mu_r = \frac{\mu}{\mu_0} \tag{3.11}$$

Combining Eqs. (3.10) and (3.11), we see that the relative permeability of a non-magnetic material is approximately equal to 1.

The refractive index of a material can be expressed as the product of the relative permittivities and permeabilities. Our assumption that the magnetic susceptibility of the material is negligible allows us to express the dielectric function solely in terms of the refractive index of the material, $n(\mathbf{r})$:

$$\begin{aligned} n(\mathbf{r}) \equiv \sqrt{\epsilon(\mathbf{r})\mu_r} \approx \sqrt{\epsilon(\mathbf{r})} \\ \therefore \epsilon(\mathbf{r}) \cong n(\mathbf{r})^2 \end{aligned} \tag{3.12}$$

5. Our final assumption is to neglect the effect of material dispersion [21]. If we select the appropriate refractive index of a material for the range of frequencies in question, we can neglect the dependency of an electromagnetic wave's frequency on its wave vector and express the refractive index as a constant.

Applying assumptions (1) and (2) to the divergence equations (Eq. (3.7a)) yields:

$$\begin{aligned} \nabla \cdot \epsilon(r)\mathbf{E}(\mathbf{r},t) = 0 \\ \nabla \cdot \mathbf{H}(\mathbf{r},t) = 0 \end{aligned} \tag{3.13}$$

Similarly, applying the assumptions to the curl equations returns the following expressions:

$$\begin{aligned} \nabla \times \mathbf{E}(\mathbf{r},t) + \mu_0 \frac{\partial \mathbf{H}(\mathbf{r},t)}{\partial t} = 0 \\ \nabla \times \mathbf{H}(\mathbf{r},t) - \epsilon_0 \epsilon(\mathbf{r}) \frac{\partial \mathbf{E}(\mathbf{r},t)}{\partial t} = 0 \end{aligned} \tag{3.14}$$

Equation (3.14) provides us with a set of linear differential equations which can be solved via the method of separation of variables. We thus consider general solutions of the form:

$$\begin{aligned}\mathbf{H}(\mathbf{r},t) &= \mathbf{H}(\mathbf{r})e^{i\omega t} \\ \mathbf{E}(\mathbf{r},t) &= \mathbf{E}(\mathbf{r})e^{i\omega t}\end{aligned} \tag{3.15}$$

Because Eq. (3.14) is linear, we know that any solution to Maxwell's equations can be composed via a linear combination of other solutions. Thus, choosing functions which vary sinusoidally with time is an appropriate choice, as these solutions allow us to construct essentially *any* function by properly building the Fourier series for the function in question.

Finally, the periodic nature of the dielectric function allows us to apply Bloch's theorem (Eq. (3.3)) to the spatial field profiles of the propagating fields:

$$\begin{aligned}\mathbf{H}(\mathbf{r}) &= e^{(i\mathbf{k}\cdot\mathbf{r})}\mathbf{u}_\mathbf{k}(\mathbf{r}) \\ \mathbf{E}(\mathbf{r}) &= e^{(i\mathbf{k}\cdot\mathbf{r})}\mathbf{w}_\mathbf{k}(\mathbf{r})\end{aligned} \tag{3.16}$$

where, similar to Eq. (3.4), $u_\mathbf{k}(\mathbf{r})$ and $w_\mathbf{k}(\mathbf{r})$ are periodic functions which conform to the periodicity of the dielectric function, defined in Eq. (3.6)

Combining Eqs. (3.15) and (3.16) allows us to express the generalized solutions to Maxwell's equations for a photonic crystal possessing a periodic dielectric function as:

$$\begin{aligned}\mathbf{H}_\mathbf{k}(\mathbf{r},t) &= \mathbf{u}_\mathbf{k}(\mathbf{r})e^{(i\mathbf{k}\cdot\mathbf{r}-\omega t)} \\ \mathbf{E}_\mathbf{k}(\mathbf{r},t) &= \mathbf{w}_\mathbf{k}(\mathbf{r})e^{(i\mathbf{k}\cdot\mathbf{r}-\omega t)}\end{aligned} \tag{3.17}$$

3.2 Frequency Eigenvalues and Eigenmodes

Combining Eqs. (3.14) and (3.15) to eliminate $\mathbf{E}(\mathbf{r})$ allows us to reformulate Maxwell's equations into what is known as the **electromagnetics master equation**:

$$\Theta\mathbf{H}(\mathbf{r}) = \left(\frac{\omega}{c}\right)^2\mathbf{H}(\mathbf{r}) \tag{3.18}$$

where $\Theta \equiv \nabla \times \frac{1}{\epsilon(\mathbf{r})}\nabla\times$. Once the dielectric function $\epsilon(\mathbf{r})$ of the problem has been specified, the master equation can be used to solve for the spatial modes of the magnetic fields, $\mathbf{H}(\mathbf{r})$. Finally, the calculated magnetic field profiles can be reentered into Eq. (3.14) to solve for the electric field configurations, $\mathbf{E}$.

One can immediately see that the electromagnetics master equation is in fact an **eigenvalue problem**. In an eigenvalue problem, an operator defined as $\mathbf{A}$ acts upon a function f [22]. This operation yields a scalar eigenvalue λ multiplied by the original function, or more concisely:

$$\mathbf{A}f = \lambda f \tag{3.19}$$

The set of eigenvalues resulting from the eigenvalue problem is known as its spectrum of eigenvalues. Each eigenvalue has a corresponding eigenfunction, f.

Under certain circumstances, the operator $\mathbf{A}$ satisfies the following condition:

$$\langle \mathbf{A}f|g\rangle = \langle f|\mathbf{A}g\rangle \tag{3.20}$$

where f and g are two distinct eigenfunctions. An operator which satisfies the condition specified in Eq. (3.20) is known as **Hermitian**. This equation tells us that a Hermitian operator applied to the first function of an inner product[2] yields an equivalent result as when the Hermitian operator is applied to the second function of the inner product.

Hermitian eigenvalue problems occur frequently in physics, the most common of which is Schrödinger's equation. As can be seen in Eq. (3.2), a Hermitian operator $\mathbf{H} = \left(-\frac{\hbar^2}{2m}\nabla^2 + U(\mathbf{r})\right)$ operates on a system's wave function, Ψ. The resulting eigenvalues corresponding to the eigenfunctions of Schrödinger's equation quantify the energy of the system.

In this case, our Hermitian operator is defined as $\Theta \equiv \nabla \times \frac{1}{\epsilon(\mathbf{r})}\nabla\times$, our eigenfunctions are the magnetic fields $\mathbf{H(r)}$, and our eigenvalues are $\left(\frac{\omega}{c}\right)^2$. The spectrum of eigenvalues and

[2]The **inner product** can be described as the n-dimensional generalization of the dot product, $f \cdot g$. If the set of eigenfunctions under consideration have an orthonormal basis, the inner product of two eigenfunctions can be defined as:

$$\langle f|g\rangle = f_1^* g_1 + f_2^* g_2 + f_3^* g_3 + ... \tag{3.21}$$

where f_i and g_j represent the various components of the eigenfunctions.

their corresponding eigenfunctions belonging to the electromagnetics Hermitian operator exhibit several attributes that offer important insights into the behaviour of electromagnetic waves satisfying the master equation:

1. Eigenfunctions representing physically realizable systems must be **normalized**, implying $\langle f|f\rangle = 1$.

2. The set of eigenvalues belonging to a Hermitian operator are known as observables. They are so named due to the fact that the spectrum of eigenvalues corresponding to a Hermitian operator must be real. Suppose the Hermitian operator $\mathbf{A}$ has an eigenfunction f with corresponding eigenvalue a. Then:

$$\begin{aligned} \langle \mathbf{A}f|f\rangle &= \langle f|\mathbf{A}f\rangle \\ a^*\langle f|f\rangle &= a\langle f|f\rangle \end{aligned} \tag{3.22}$$

   where a^* represents the complex conjugate of the eigenvalue a. Because the eigenfunctions under consideration are normalized, as specified above, we know $\langle f|f\rangle = 1$. This implies that $a^* = a$ and, equivalently, that all eigenvalues belonging to a Hermitian operator must be **real**.

3. Eigenfunctions belonging to distinct eigenvalues are **orthogonal** to each other. Suppose two eigenfunctions f and g have corresponding, distinct eigenvalues a and b. Taking the inner product of the eigenfunctions with the Hermitian operator $\mathbf{A}$ yields:

$$\begin{aligned} \langle \mathbf{A}f|g\rangle &= \langle f|\mathbf{A}g\rangle \\ a^*\langle f|g\rangle &= b\langle f|g\rangle \end{aligned} \tag{3.23}$$

   Provided $a \neq b$, the inner product of the eigenfunctions $\langle f|g\rangle$ must be equal to zero.

4. Eigenfunctions belonging to a Hermitian operator form a **complete set**. That is, *any* solution to a specific eigenvalue problem can be constructed by a linear combination of other eigenfunctions.

5. Spatial bounding of the eigenfunctions of a Hermitian operator results in the formation of a **discrete** spectrum of eigenvalues. When the eigenfunctions are unbounded, their

corresponding eigenvalues can take on a continuous range of values. However, spatial limits of the eigenfunctions imposes certain boundary conditions on the spatial profiles of the functions, implying that they can only take on certain configurations. The resulting spectrum of eigenvalues corresponding to the bounded eigenfunctions are thus restricted to a discrete set of values.

These attributes provide us with a mathematically robust explanation as to why only certain frequencies of light are allowed to propagate through a photonic crystal, while others are prohibited. The discrete translational symmetry of the photonic crystal's dielectric function forces a periodicity, or a repetition of a bounded field profile, of the magnetic fields. As a result, only certain frequencies of light, corresponding to a discrete spectrum of eigenvalues, can propagate through the photonic crystal. However a deeper understanding of the unique characteristics of photonic crystals is achieved by examining precisely *why* the field profiles of magnetic fields take on certain configurations. This alternative explanation can best be achieved through examination of the one-dimensional photonic crystal.

3.3 One-dimensional photonic crystal structures

We start by considering a one-dimensional photonic crystal possessing a uniform dielectric profile in the $\hat{y}$ and $\hat{z}$ directions, with discrete translational symmetry of periodicity a in the $\hat{x}$-direction. Due to the discrete translational symmetry of the dielectric function in the $\hat{x}$-direction, the physical representation of the photonic crystal has strong corollaries to the **Bravais lattice** used to describe a crystalline structure in solid state physics (see Figure 3.2) [19]. If we wish to transform into momentum space, we can describe the physics of the system via the **reciprocal lattice**, whose reciprocal lattice vector is defined as $\mathbf{k} = \frac{2\pi}{\mathbf{a}}$.

One fundamental postulate in solid state physics is that *all* physical phenomena corresponding to a periodic array of discrete points (i.e. the Bravais lattice) can be described in reciprocal space by what is known as the **first Brillouin zone**. The first Brillouin zone is a cell which spans the volume of space containing exactly one lattice point, but which neither overlaps nor leaves vacancies with any surrounding cells. Alternatively, the first Brillouin zone can

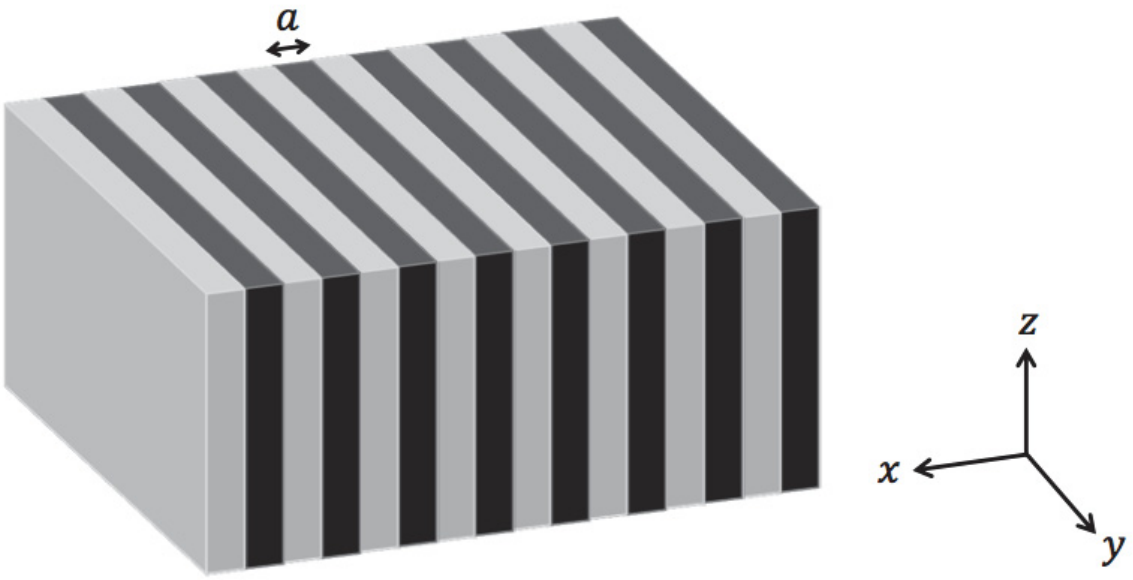

FIGURE 3.1: A one-dimensional photonic crystal possessing a periodic dielectric function of lattice constant a in the $\hat{x}$-direction.

be described as the volume in reciprocal space beyond which the k-points describe redundant physical phenomenon.

Similarly, in photonic crystal electromagnetics the dispersion relation describing the propagating electromagnetic wave can be represented by the first Brillouin zone in photonic reciprocal space. For a one-dimensional photonic crystal with a lattice vector $\mathbf{a} = a\hat{x}$, the first Brillouin zone spans the space from $k_x = -\frac{\pi}{a}$ to $k_x = +\frac{\pi}{a}$, corresponding to the length of one reciprocal lattice vector. These k_x points coincide with what is known as the **photonic band edge**. Points on the dispersion relation falling outside of the first Brillouin zone provide no new information concerning the dispersion relation of the photonic crystal but, rather, correspond to degenerate eigenfunctions with shared frequency eigenvalues. Specifically, there exists a degeneracy of states at the photonic band edge where the eigenfunction at $k_x = -\frac{\pi}{a}$ is equivalent to the eigenfunction at $k_x = +\frac{\pi}{a}$.

In Ref. [21], a qualitative description of the behaviour of an electromagnetic wave in a one-dimensional photonic crystal is provided, which offers insight into the physical phenomena occurring at the photonic band edge. As in any physical system, the field profile of a propagating magnetic field arranges itself so as to minimize the energy (or, equivalently, the frequency

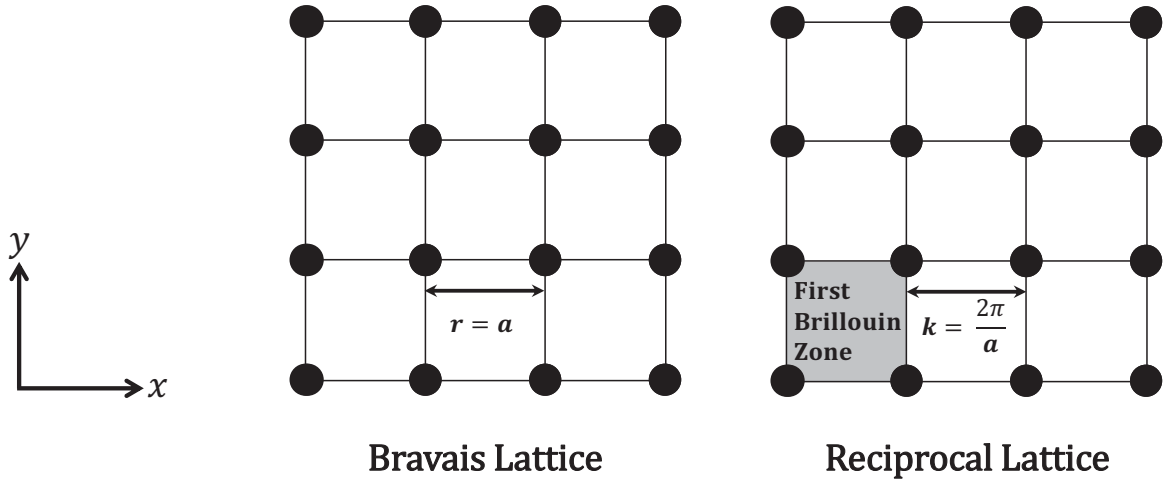

FIGURE 3.2: A crystal lattice with a lattice vector of $\mathbf{r} = \mathbf{a}$ and its equivalent lattice in reciprocal space. The first Brillouin zone of the reciprocal lattice is indicated by the shaded unit cell, whose length spans the space of one reciprocal lattice vector, $\mathbf{k} = \frac{2\pi}{\mathbf{a}}$.

eigenvalue) of the system. The energy of the system can be described using the **energy functional**, which yields a scalar quantity specifying the energy of a particular electromagnetic field configuration in vector space. The energy functional of an electromagnetic wave propagating through a photonic crystal is defined as:

$$U_f(\mathbf{H}) \equiv \frac{\langle \mathbf{H}, \Theta\mathbf{H} \rangle}{\langle \mathbf{H}, \mathbf{H} \rangle} \tag{3.24}$$

Variational principle can be utilized to probe the effect that small variations of the magnetic field profiles have upon the energy of the system. Use of the method provides a description of one means by which we can minimize the energy functional of the fields:

$$U_f(\mathbf{H}) = \frac{\int |\nabla \times \mathbf{E}(\mathbf{r})|^2 d^3\mathbf{r}}{\int \epsilon(\mathbf{r}) |\mathbf{E}(\mathbf{r})|^2 d^3\mathbf{r}} \tag{3.25}$$

This equation demonstrates that the denominator of the energy functional can be maximized by placing the strength of the electric field in regions of the photonic crystal possessing a high dielectric constant.

The discrete translational symmetry of the photonic crystal allows degenerate electromagnetic field eigenfunctions found at the photonic band edge to take one of two separate field configurations:

1. The field concentrates its electric field energy density in the regions of material in the photonic crystal possessing a **high** dielectric constant. This configuration lowers the energy functional, resulting in a lowering of the frequency eigenvalue at the photonic band edge.

2. The field concentrates its electric field energy density in the regions of material in the photonic crystal possessing a **low** dielectric constant. This configuration minimizes the denominator of Eq. (3.25), resulting in an increase of the corresponding band edge frequency eigenvalue.

The two field configurations available to the electromagnetic field due to the discrete translational symmetry of the one-dimensional photonic crystal breaks the degeneracy of the eigenfunctions at the photonic band edge. This results in the formation of what is known as a **photonic band gap**. Similar photonic band gaps due to the degeneracy of eigenfunctions found at the points $k_x = \pm\frac{2\pi}{a}, \pm\frac{3\pi}{a}, ...$ will be found at higher energies, resulting in a photonic band structure. Photons with frequencies falling within the photonic band gaps are completely prohibited from propagating through the photonic crystal. Only electromagnetic waves possessing a wave vector and corresponding frequency falling on a photonic band may travel through the crystal undisturbed. Most importantly for our discussion on photonic crystal ring resonators, the photonic dispersion relation at the band edge flattens out, signifying that the derivative of the frequency of the photon with respect to its wave vector, $\frac{d\omega}{dk_x}$, is equal to zero. The implications of this unique characteristic belonging to photons at the photonic band edge are found by exploring the general behaviours and attributes of electromagnetic waves.

3.3.1 Wave dynamics: Phase and group velocity

We begin with the most general description of a wave propagating in one-dimension [23]:

$$\frac{\partial^2 u(x,t)}{\partial x^2} = \frac{1}{v_x^2}\frac{\partial^2 u(x,t)}{\partial t^2} \tag{3.26}$$

Here u describes the x-component of a wave, while v_x denotes the x-component of the velocity of the wave. This second-order differential equation is known as the one-dimensional **wave equation** and describes the relationship between the spatial variation of a wave and its time evolution. Because the left hand side of the equation depends solely on the position component x, while the right-hand side depends uniquely on time, the differential equation can be solved via the method of separation of variables. We start by assuming a solution to the problem of the form:

$$u(x,t) = X(x)T(t) \tag{3.27}$$

Substituting Eq. (3.27) into Eq. (3.26) yields a solution which satisfies the wave equation [24]:

$$u(x,t) = A\cos(\omega t - k_x x + \phi) \tag{3.28}$$

where A and ϕ are respectively the arbitrary amplitude and phase angle determined by the initial conditions of the wave at $x = t = 0$.

We now consider the time evolution of a point on the wave of fixed phase angle, ϕ, which can be described as:

$$\begin{aligned} u(x,t) &= u(x+\Delta x, t+\Delta t) \\ A\cos(\omega t - k_x x + \phi) &= A\cos(\omega(t+\Delta t) - k_x(x+\Delta x) + \phi) \\ \omega t - k_x x &= \omega(t+\Delta t) - k_x(x+\Delta x) \\ \frac{\omega}{k_x} &= \frac{(x+\Delta x) - x}{(t+\Delta t) - t} \end{aligned} \tag{3.29}$$

For infinitesimal periods of time, this equation becomes:

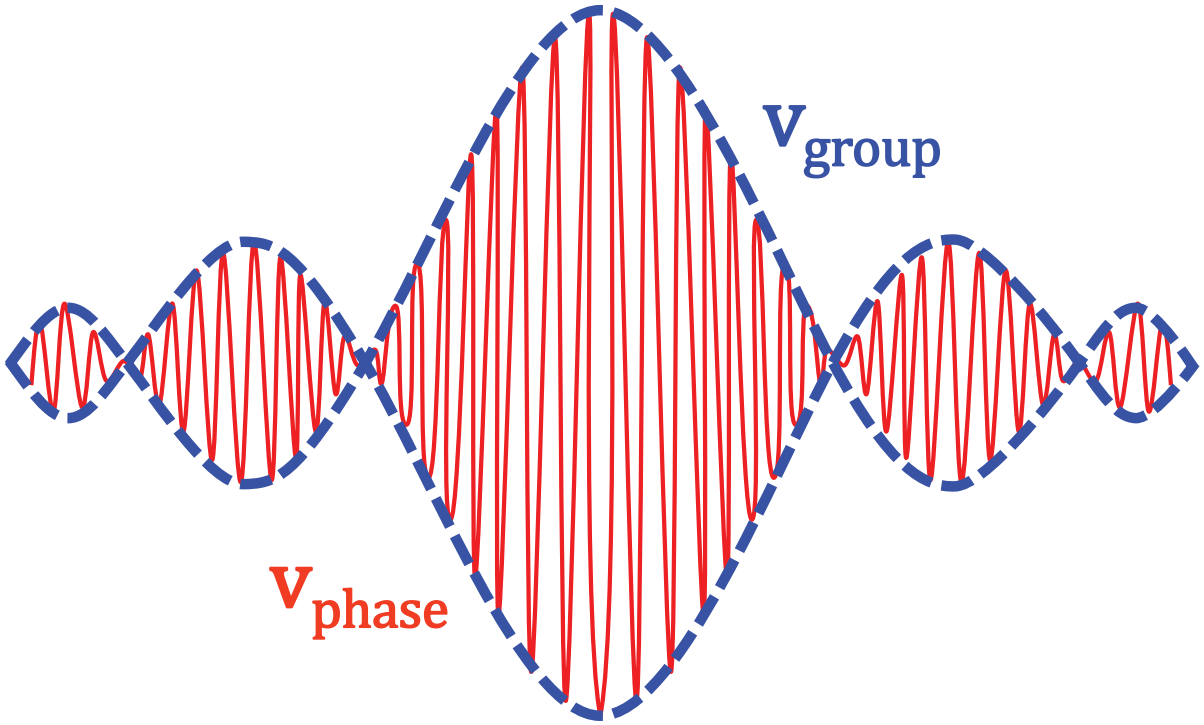

FIGURE 3.3: A propagating light pulse. The outer envelope (indicated by the dotted blue line) represents the wave's group velocity, while the inner oscillations (indicated in red) indicate the wave's phase velocity.

$$\frac{dx}{dt} = \frac{\omega}{k_x} \tag{3.30}$$

Eq. (3.30) describes the velocity of a group of points on a waveform of *constant phase angle* and is known as the **phase velocity**. It can easily be generalized to three dimensions to yield the equation:

$$\mathbf{v_p} = \frac{\omega}{\mathbf{k}} \tag{3.31}$$

Similarly, if we consider points on a waveform of *constant amplitude*, the velocities of said points can be described by the wave's **group velocity**:

$$\mathbf{v_g} = \frac{d\omega}{d\mathbf{k}} \tag{3.32}$$

Graphically, the phase velocity is represented by the inner oscillations of a wave packet. The inner oscillations of the wave can move at a rate either slower or faster than that of the outer envelope. However, the rate at which information can be transmitted by a wave is ultimately determined by its group velocity.

Wave packets can be described as either traveling or standing waves. A traveling wave has a non-zero group velocity, allowing for the outer envelope of the wave packet to propagate in a specified direction. Alternatively, a standing wave has a **zero group velocity**. Rather than propagating, the wave packet instead displays simple harmonic oscillations in the amplitudes of various points on the waveform.

Electromagnetic waves with a low group velocity are known as **slow light waves**. As mentioned at the end of Section 3.3, the derivative of the photonic dispersion relation of a one-dimensional photonic crystal, $\frac{d\omega}{dk_x}$, approaches zero at the photonic band edge. As a result, it can be said that an electromagnetic wave in a one-dimensional photonic crystal whose x-component of the wave vector is equal to $\pm\frac{\pi}{a}$ has a zero group velocity. As will be seen in the next chapter, slow light electromagnetic waves possess special properties which make them particularly interesting for use in microresonators.

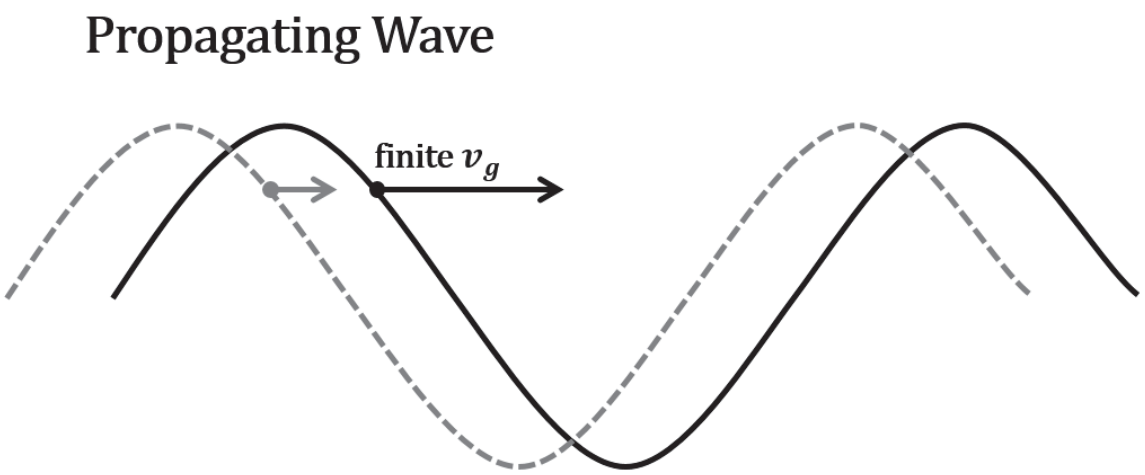

(A) A propagating waveform with a finite group velocity.

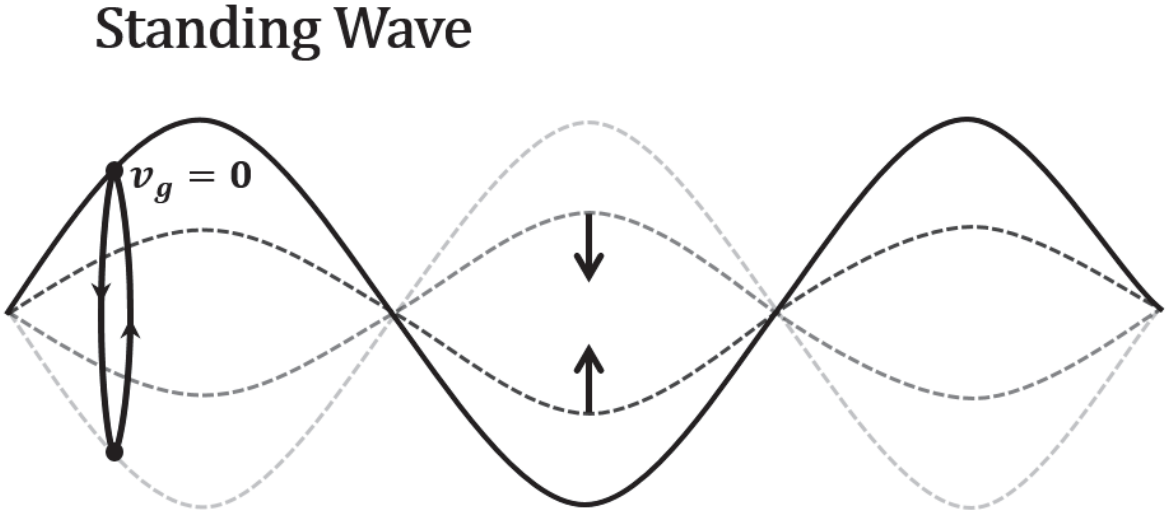

(B) A standing wave with $v_G = 0$. Each point on the waveform undergoes simple harmonic oscillations in amplitude.

FIGURE 3.4: A propagating and standing waveform.

Chapter 4

Slow light enhancement of photonic crystal ring resonator modes

In Chapter 3, our discussion on periodically patterned dielectric structures demonstrated how photonic crystals can be employed to "slow down" the group velocity of an electromagnetic wave. Chapter 4 will be dedicated to exploring precisely how slow light effects can be produced in microresonators and what subsequent outcomes can reasonably be expected. We will start with a discussion on the impacts of slow light resonant modes in microresonators and then conclude with a description on how microresonators and periodically patterned dielectric structures are combined to produce a particularly interesting slow light microstructure: the photonic crystal ring resonator.

4.1 Qualities of slow light resonant modes

To better understand the nature of slow light in a photonic crystal, we start by examining a propagating electromagnetic wave in a photonic crystal waveguide. The photonic crystal waveguide is formed by introducing a one-dimensional line "defect" into a two-dimensional photonic crystal (see Figure 4.1). As the wave propagates through a photonic crystal waveguide, it encounters multiple dielectric interfaces which can result in the backscattering of a forward-propagating mode into a backward-propagating mode [25]. At the photonic band edge, the backscattered

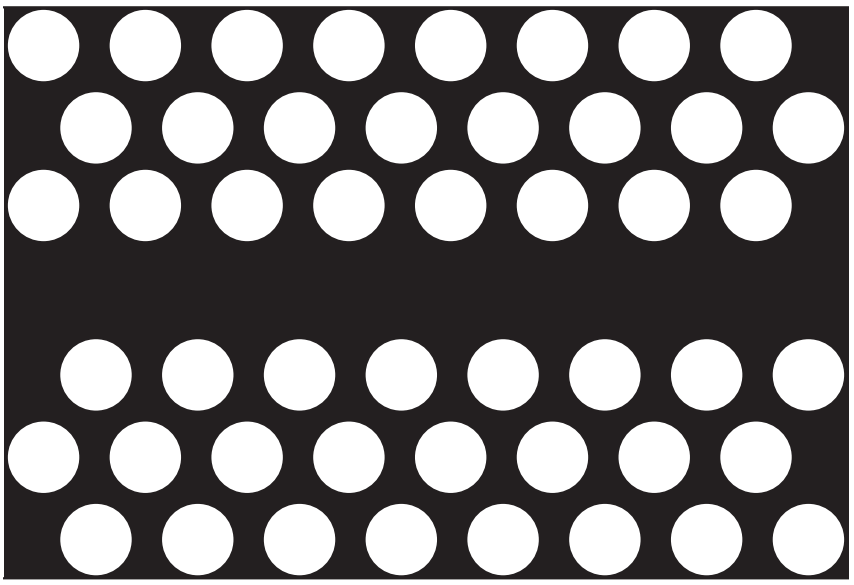

FIGURE 4.1: A photonic crystal waveguide formed by introducing a line defect of missing holes in a photonic crystal slab. The photonic crystal slab is composed of a high refractive index material (indicated in black) with a lattice of low refractive index holes (indicated in white)

.

light interferes constructively with the forward-propagating mode, resulting in a standing wave configuration. As discussed in Section 3.3.1, a standing wave does not propagate but, rather, undergoes simple harmonic oscillations in amplitude. Accordingly, the linear combination of the in phase forward- and backward-propagating light waves can be considered as a zero group velocity, slow light resonance of the photonic crystal waveguide.

As we move away from the band edge, the backscattered light falls more and more out of phase with the forward-propagating electromagnetic wave. Close to the band edge, the light can be said to fall within the "slow light regime". The light can no longer be classified as a standing wave, as it possesses a small, yet finite, group velocity. Rather, the resonances found near the band edge will demonstrate the slow propagation of an interference pattern. Once we are far enough removed from the photonic band edge so that the resonances can no longer be classified as falling within the slow light regime, the propagation of light waves is now dominated by the process of total internal reflection, rather than the interference of forward- and backward-propagating waves.

The slow light nature of electromagnetic waves allows for interesting phenomena that make slow light resonators of interest for use in integrated photonic circuits. The following sections are

dedicated to discussing these unique properties in more detail.

4.1.1 Enhanced light-matter interactions

Slow light resonant modes have been shown to possess enhanced interaction between the dielectric material and the propagating electromagnetic wave [26–28]. This phenomenon can be attributed to two separate causes:

1. **Low group velocity/Increased optical path length**:
   Enhanced light-matter interactions due to the low group velocity of slow light electromagnetic fields is intuitively quite easy to comprehend. The slower the group velocity of a propagating field, the more time it has to interact with its surrounding material. An alternative explanation is found through examination of the **optical path length** (OPL) of a light wave in an optical cavity [29]. The OPL relates the distance a photon travels in free space in a given time, t, to the distance the photon travels in an optical cavity in the same time period:

$$\mathrm{OPL} = \frac{c}{v_g} L_{\mathrm{medium}} \tag{4.1}$$

   This equation indicates that the optical path length traveled by a photon will always be greater than the physical length, L_{medium}, of an optical cavity. It is also evident that the optical path length diverges as the group velocity of the light approaches zero, resulting in a nearly infinite interaction length between the photon and its surrounding material.

2. **Increased optical energy density**:

   As an electromagnetic wave enters the slow light regime, the front of the light pulse will accordingly experience a decrease in its group velocity. However, the group velocity of the back of the light pulse will continue on unaltered, resulting in a spatial compression of the optical pulse [25]. Assuming that no energy is lost by the light pulse upon arrival in the slow light regime, the resulting electromagnetic wave will exhibit increased optical energy densities. As a result, the slow light wave will interact more strongly with the surrounding material.

It must be clarified that increased optical energy densities of slow light electromagnetic waves can only be expected in environments possessing low second and third-order dispersion parameters. Otherwise, the dispersive properties of the surrounding material will cause the optical pulse to distort, counteracting the favourable spatial compression of the electromagnetic fields. In order to take advantage of increased optical energy densities, a slow light resonator must be designed so as to slow the group velocity of an electromagnetic wave, while simultaneously avoiding large second and third-order dispersion parameters (refer to Section 6.5.1 for additional details).

4.1.2 Improvement of quality factors

Slow light electromagnetic waves in microresonators have also been shown to possess high quality factors or, equivalently, low optical losses [30]. In Ref. [31], a theoretical model is developed which provides a qualitative description of the slow light enhancement of a microresonator's quality factors. We start by considering a microresonator which is coupled to both an input and output channel. The quality factor of the resonator can be described by:

$$\frac{1}{Q_{res}} = \frac{1}{Q_{rad} + Q_{abs} + Q_{IO}} \tag{4.2}$$

Here Q_{rad} quantifies the optical losses due to coupling of the microresonator's modes to radiation modes, Q_{abs} represents the quality factor related to the material absorption of the electromagnetic fields, and Q_{IO} is the quality factor due to coupling with the input and output ports. The transmission of the non-dispersive resonator is expressed as:

$$T_{non-disp}(\omega) = \frac{P_{out}(\omega)}{P_{in}(\omega)} = \frac{{\Gamma_{IO}}^2}{(\omega - \omega_{res})^2 + (\Gamma_{rad} + \Gamma_{abs} + \Gamma_{IO})^2} \tag{4.3}$$

where P_{in} and P_{out} are the incoming and outcoming powers, $\Gamma_{rad}, \Gamma_{abs}$, and Γ_{IO} represent the radiation, absorption, and input/output FWHMs, respectively, and ω_{res} is the resonant frequency of the microresonator in question.

We now consider the transmission of an equivalent resonator whose material has been replaced with a highly dispersive material. In this case, a highly dispersive material refers to a medium possessing a high group index, which is defined as [32]:

$$n_g = c\frac{dk}{d\omega} = \frac{c}{v_g} \tag{4.4}$$

We see here that the group index experienced by an electromagnetic wave is inversely proportional to its group velocity; hence, a resonator composed of a highly dispersive material can be considered as equivalent to a resonator with slow light propagating modes.

By replacing the non-dispersive material of the resonator by a highly dispersive material, each electromagnetic wave of frequency ω will perceive a different change in the refractive index of the material:

$$\partial n(\omega) = n(\omega) - n(\omega_{res}) \approx (\omega - \omega_{res})\frac{dn}{d\omega}\bigg|_{w_{res}} \tag{4.5}$$

Equation (4.5) tells us that for $\omega > \omega_{res}$, $\partial n(\omega) > 0$, indicating that the frequencies see a perceived shift in the resonance curve to the left. Likewise, $\omega < \omega_{res}$ experience a negative change in refractive index ($\partial n(\omega) < 0$), resulting in a perceived shift in the resonance curve to the right. The resulting resonance curve is much narrower as compared to the resonance curve in a non-dispersive material. Recall from Section 2.4.1 that the FWHM of a resonant curve is inversely proportional to its quality factor. As a result, a narrowing of the resonance curve signifies an increase in the quality factor of the microresonator.

Examination of the transmission of the microresonator composed of a highly dispersive material provides further clarification as to precisely why the enhancement of quality factors occurs. From Ref. [31], in a highly dispersive material, Eq. (4.3) becomes:

$$T_{disp}(\omega) = \frac{{\Gamma_{IO}}^2 \Big/ \left[1 + \frac{\sigma}{n(\omega_{res})}\left(\frac{c}{v_g} - n(\omega_{res})\right)\right]^2}{(w - w_{res})^2 + (\Gamma_{rad} + \Gamma_{abs} + \Gamma_{IO})^2 \Big/ \left[1 + \frac{\sigma}{n_{res}}\left(\frac{c}{v_g} - n(\omega_{res})\right)\right]^2} \tag{4.6}$$

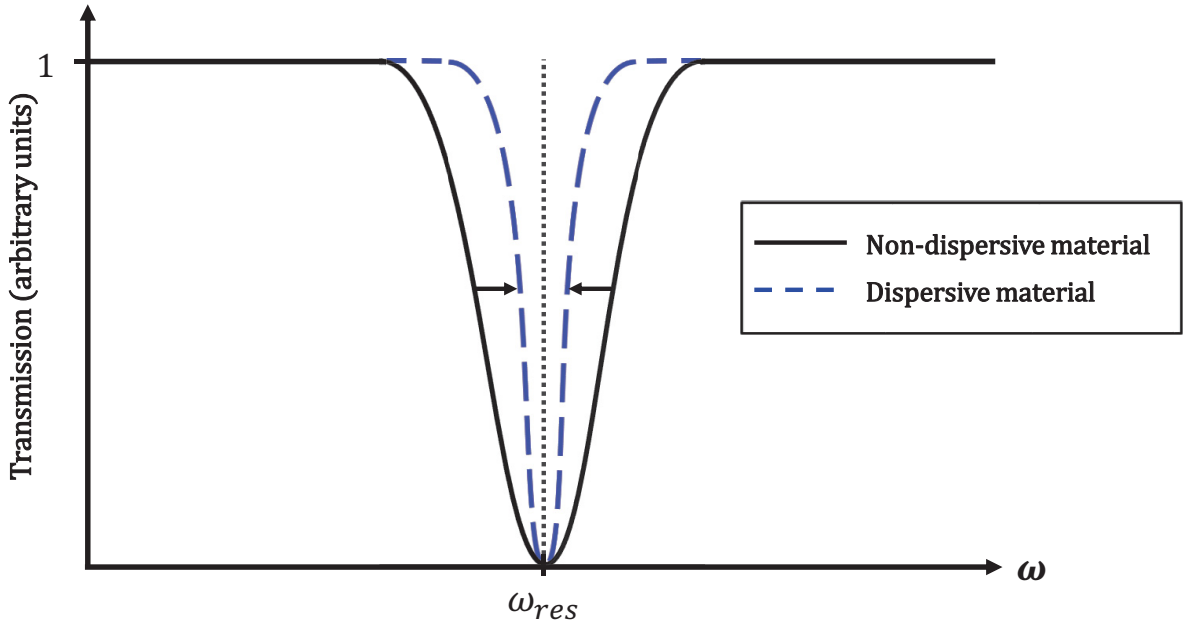

FIGURE 4.2: The transmission curves of microresonators composed of non-dispersive and highly dispersive materials. The FWHM of the resonance in a dispersive material is reduced, implying decreased optical losses of the resonator.

where $\sigma \equiv \left[\int_{V_{\partial n}} \epsilon(\mathbf{r})|\mathbf{E}(\mathbf{r})|^2 d^3x\right] \Big/ \left[\int_{V_{mode}} \epsilon(\mathbf{r})|\mathbf{E}(\mathbf{r})|^2 d^3x\right]$ is defined as the fraction of the electric displacement field energy found in the highly dispersive material.

As can be seen in Eq. (4.6), each FWHM factor quantifying optical losses (i.e. $\Gamma_{rad}, \Gamma_{abs}$, and Γ_{IO}) are reduced by a factor of $\left[1 + \frac{\sigma}{n(\omega_{res})}\left(\frac{c}{v_G} - n(\omega_{res})\right)\right]^2$. This reduction leads to an overall increase in the lifetime of the photon in the microresonator.

4.2 Photonic crystal ring resonators

As seen in the previous section, the various qualities of slow light microresonators position the devices as highly desirable for integration into photonic circuits. One particular device which has demonstrated potential as an effective means by which to slow down the propagation of light waves is the **photonic crystal ring resonator** (PhCRR). A PhCRR merges the properties of a standard ring resonator with those of a photonic crystal. The resonator is formed by superimposing a periodic dielectric structure of low refractive index material holes of radius r onto a high refractive index material ring resonator. The periodicity of the photonic crystal structure is quantified by its lattice vector, a. The resonant wavelengths of the resonator are

dependent upon several factors, namely the effective refractive indices of the ring material, n_{ring}, and the photonic crystal lattice holes, n_{hole}, the width of the ring, w, and the photonic crystal's **filling factor**, defined as $ff = \frac{r}{a}$.

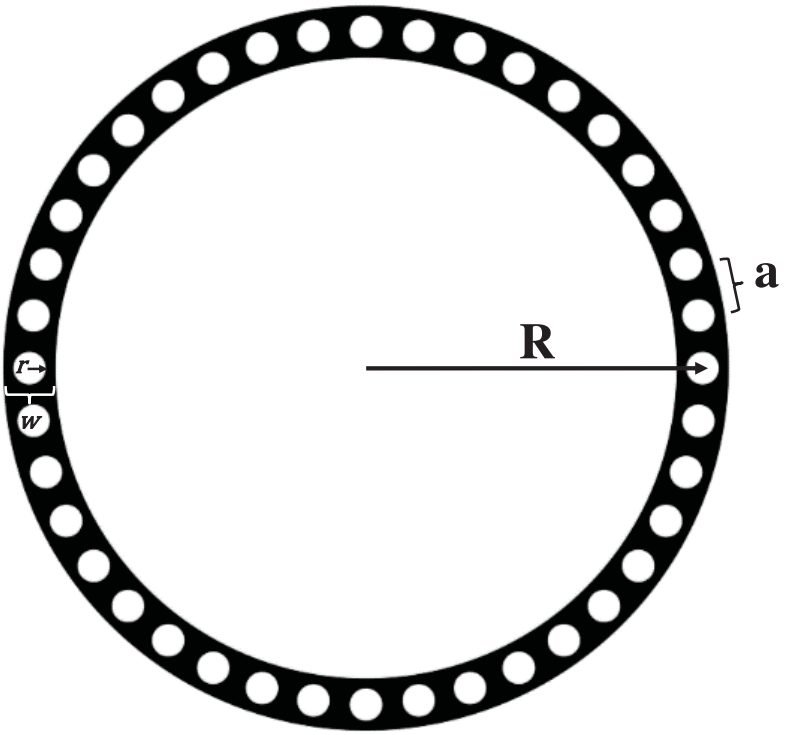

FIGURE 4.3: A photonic crystal ring resonator of radius R composed of a high refractive index ring resonator, n_{ring}, (indicated in black) overlaid with a photonic crystal lattice of low refractive index holes, n_{hole} (indicated in white).

In a standard ring resonator, the effects of waveguide dispersion can slightly modify the mode spectrum of the resonator. Recall from Section 2.3.2 that the waveguide dispersion is attributed both to the refractive index of the resonator's material and the geometric properties of the ring; these properties allow for the slight reduction of the wave's group velocity as compared to the propagation of a wave in vacuum. However, a ring resonator lacks the capacity to significantly alter the group velocity of a propagating wave to the extent that it falls within the slow light regime.

Alternatively, the periodic nature of the dielectric media seen by a propagating PhCRR resonant mode can dramatically alter the dispersion of the resonator, providing design control over the group velocity of a resonance. If a resonant mode of the PhCRR has a wave vector which coincides with the photonic band edge in reciprocal space, the mode will possess a zero group

velocity and will thus exhibit the previously discussed properties of slow light modes. As a result, it is of high interest to formulate a design method which will allow for the selective positioning of resonant modes in the slow light regime of a photonic crystal ring resonator's dispersion relation. Chapter 5 will be dedicated to presenting just such an approach.

Chapter 5

Design of slow light resonant modes in photonic crystal ring resonators

In order to fully exploit the enhancement of light-matter interactions and quality factors of slow light resonances, we wish to position the resonant modes of a PhCRR in the desirable regions of the photonic dispersion relation. As was explored in the previous chapters, precise design of the waveguide and photonic crystal geometries provides engineering control over the photonic dispersion relation. Accordingly, the potential lies for the construction of a PhCRR which maximizes the slow light enhancement of its resonances through careful selection of its geometric parameters.

Previous design approaches have succeeded in placing resonant modes in the slow light region of a photonic crystal ring resonator's dispersion relation [30, 33]. However, they have lacked the capacity to systematically choose design criteria which will ensure a band edge mode, depending rather on trial and error efforts in the design of the photonic crystal ring resonator's geometry. The core of this work is a novel design approach which allows for the precise selection of photonic band edge resonant modes [34]. Moreover, the periodic dielectric structure of the photonic crystal ring resonator provides scaling control over the wavelengths at which these resonances are placed.

5.1 Step 1: Dispersion relation of a one-dimensional photonic crystal waveguide

The first step of the design approach is to model the dispersion of an infinitely long waveguide possessing a periodic dielectric function in one dimension. In considering the photonic crystal ring resonator as a straight waveguide, we have assumed that the radius of curvature of the PhCRR is large enough so that bending losses can be neglected (i.e. $R > \frac{\lambda_0}{n_{eff}}$). A computational approach is employed which makes use of the open-source MIT Photonic Bands (MPB) software package [35]. MPB is a a frequency domain eigensolver which simultaneously computes frequency eigenvalues and their corresponding eigenmodes using a plane-wave basis.

FIGURE 5.1: A representative portion of an infinitely long photonic crystal waveguide of width w. The waveguide is composed of a high refractive index material (indicated in black), overlaid with a photonic crystal lattice of low refractive index holes (indicated in white) of radius r and lattice constant a. The photonic crystal waveguide is oriented in the $x-y$ plane with the $\hat{z}$-direction coming out of the page.

A unit cell of length a representing the physical dielectric function is first specified in generalized coordinates. MPB calculates the photonic dispersion relation in reciprocal space and accounts for the creation of photonic band gaps by assuming the unit cell periodically repeats itself an infinite number of times. The photonic dispersion relation of the photonic crystal is computed in units of its periodicity. It therefore outputs a dimensionless frequency, ν_D, which is given in units of $\frac{c}{a}$. The dimensionless frequency can subsequently be scaled to a physical frequency by changing the value of the lattice constant.

Due to limited computational resources, simulations are conducted in two dimensions. The two-dimensional photonic crystal waveguide in question possesses mirror symmetry about the z-axis (see Figure 5.1). It can be shown [21] that any two-dimensional photonic crystal with a mirror symmetry plane can be categorized as possessing one of the following two polarizations:

1. **Transverse-electric (TE) polarization:**

   A transverse electric mode possesses an electric field whose propagation is restricted to the $x-y$ plane of the photonic crystal. It is described in terms of its only non-zero components (E_x, E_y, H_z).

2. **Transverse-magnetic (TM) polarization:**

   Alternatively, a transverse magnetic mode restricts the propagation of its *magnetic* field to the $x-y$ plane of the photonic crystal. It can thus be characterized in terms of the components (H_x, H_y, E_z).

The two-dimensional approximation of the three-dimensional case is improved by using a calculated effective refractive index of a waveguide of thickness, t, on a substrate with low index cladding. The filling factor of the photonic crystal lattice and the width of the waveguide are also specified in units of the lattice constant a. While the filling factor will affect the shape of the dispersion relation, the band edge dimensionless frequency remains largely unaffected, providing flexibility in the choice of the $\frac{r}{a}$ ratio. Because the waveguide possesses a periodicity of length a, we need only compute the dispersion relation of the first Brillouin zone in reciprocal space.

Figure 5.2 depicts the first three photonic bands of the photonic crystal waveguide for modes with transverse-electric polarization. The dashed line represents the "light line", which quantifies the dispersion relation of an electromagnetic wave propagating through free space. The regions of the photonic bands falling above the light line correspond to modes which are not confined to the waveguide but, rather, to radiation modes which will leak into the surrounding cladding material. The further the mode is found from the light line, the lower the overlap of a guided mode profile with that of a radiation mode profile. Consequently, modes found far from the light line will not couple into the lossy radiation modes of the system and will thus be strongly confined to the core of the waveguide. Our area of interest lies in the slow light region of the photonic dispersion relation, corresponding to the reciprocal space band edge of the first photonic band.

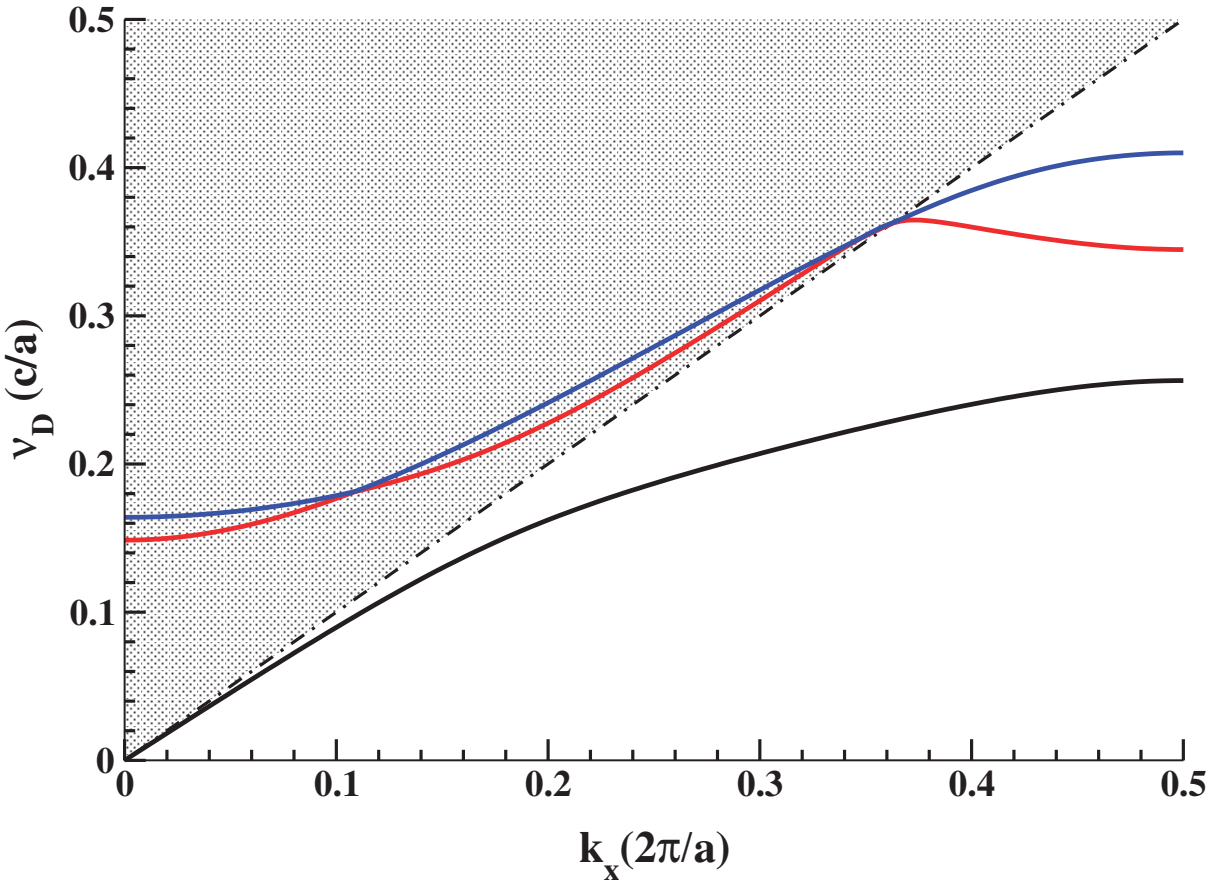

FIGURE 5.2: The first three photonic bands of a photonic crystal waveguide with $n_{eff} = 2.83$, $ff = 0.3$, and $w = 1.0$a. The first, second, and third photonic band are represented as the solid black, red, and blue lines, respectively. The dashed black line corresponds to the light line; any propagating waves falling on the dispersion curves found above the light line (i.e. in the shaded region) correspond to radiation modes which will decay exponentially into the air cladding of the photonic crystal waveguide.

5.2 Step 2: Spatial bounding of the photonic crystal waveguide

In order to convert the continuous spectrum of frequency eigenvalues belonging to the infinitely long waveguide to a discrete spectrum of eigenvalues corresponding to the photonic crystal ring resonator, boundary conditions must be imposed that enforce spatial bounding of the structure. The first boundary condition ensures periodicity of the photonic crystal structure; more precisely, an integer number of unit cells are required to fit within the perimeter of the ring:

$$Na = 2\pi R \tag{5.1}$$

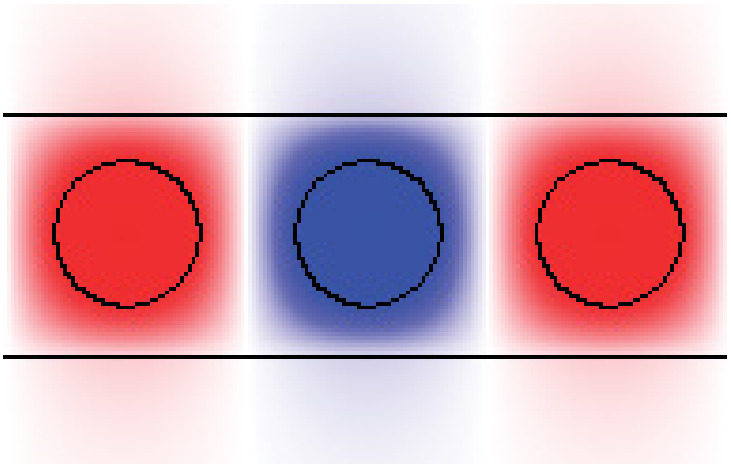

(A) H_z of the first photonic band

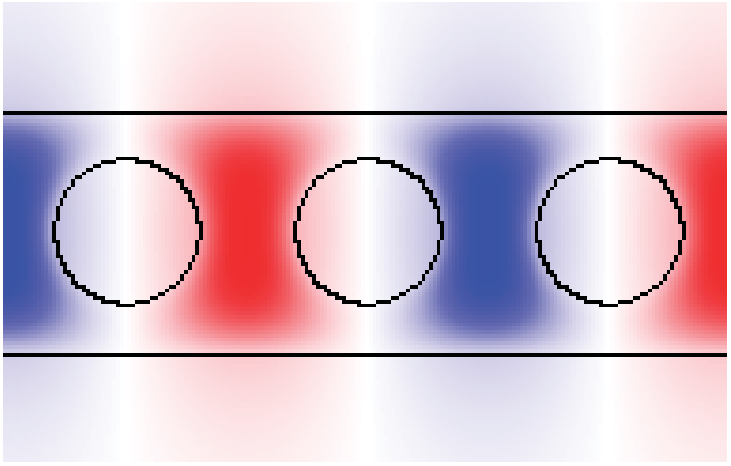

(B) H_z of the second photonic band

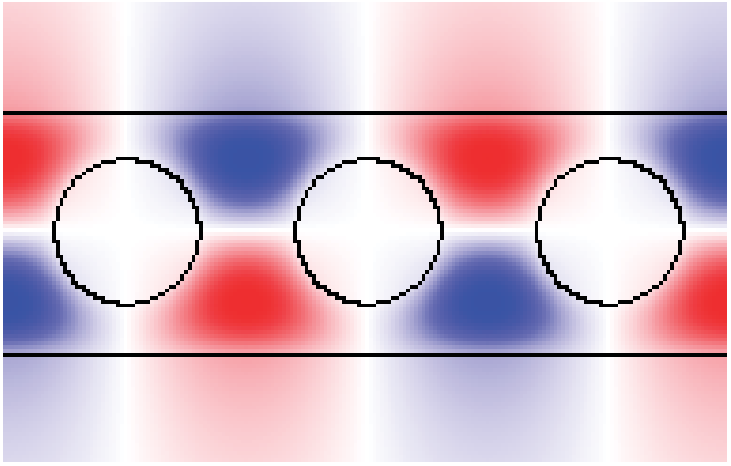

(C) H_z of the third photonic band

FIGURE 5.3: Magnetic field configurations of the first three photonic bands

Here $N \in \mathbb{Z}$ is defined as the number of unit cells found in the ring. The second boundary condition enforces phase matching of a propagating electromagnetic wave by requiring resonant modes to have an integer number of wavelengths that fit within the ring:

$$k_x R = m \tag{5.2}$$

where $m \in \mathbb{Z}$ corresponds to the mode number of a given resonance. Combining Eqs. (5.1) and (5.2), we are left with an expression for k_x which depends on the number of unit cells in the photonic crystal ring resonator and the lattice constant of the periodic dielectric function:

$$k_x = \frac{2\pi m}{Na} \tag{5.3}$$

In order to place a resonant mode of the PhCRR directly at the photonic band edge, we must require the $\hat{x}$-component of the wave vector be equal to $\frac{\pi}{a}$. Inserting this condition into Eq. (5.3) yields:

$$m_{BE} = \frac{N}{2} \tag{5.4}$$

Because we have required m to be an integer value, Eq. (5.4) reveals that a photonic band edge resonant mode can only occur in photonic crystal ring resonators possessing an even number of unit cells.

Figure 5.4 demonstrate graphically how the discrete spectrum of frequency eigenvalues are determined. Using an alternative, but equivalent, representation of the first Brillouin zone, the dispersion relation of the first photonic band of the photonic crystal waveguide is plotted. The boundary conditions, seen in red and blue, are superimposed onto the dispersion relation. Every intersection between a vertical line and the first photonic band represents a resonant mode of the photonic crystal ring resonator. When N is an even number, a resonance is found directly at the photonic band edge. Alternatively, the N odd configuration does not possess a band edge mode but, rather, has its resonances placed symmetrically about the band edge.

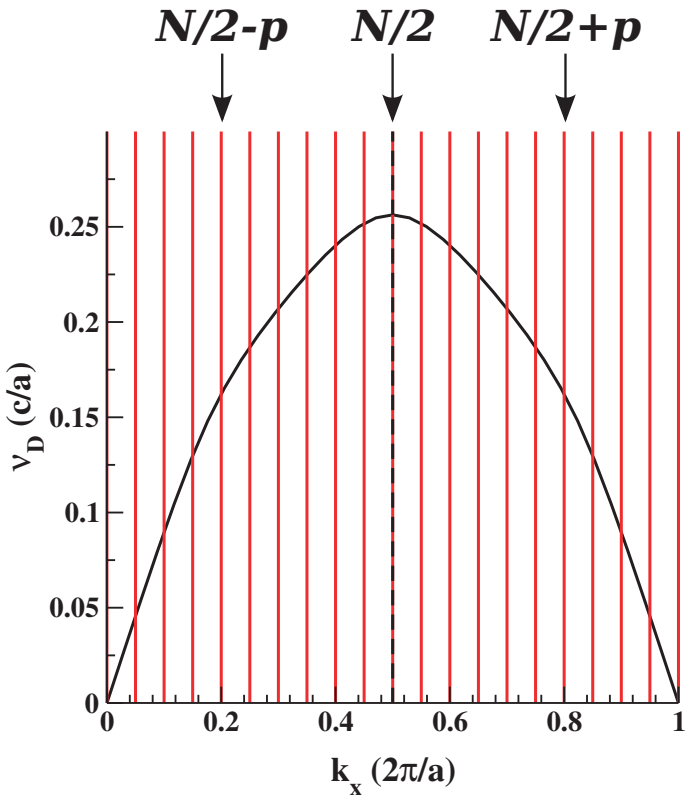

(A) The discrete spectrum of eigenvalues corresponding to the N-even configuration. The dispersion relation for the photonic crystal waveguide is plotted from $k_x = 0$ to $\frac{2\pi}{a}$, spanning the length of one reciprocal lattice vector.

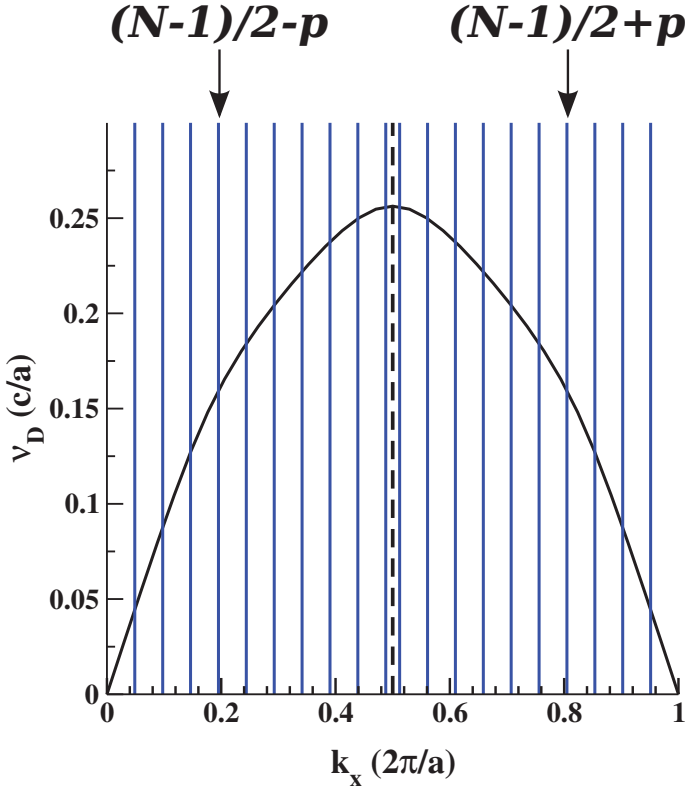

(B) The discrete spectrum of eigenvalues corresponding to the N-odd configuration.

FIGURE 5.4: The dispersion relations and boundary conditions for the photonic crystal ring resonator. A photonic band edge mode is found only in the N-even configuration.

One notable feature of a photonic crystal ring resonator is its free spectral range. Recall from Section 2.4.1 that the free spectral range quantifies the spacing in wavelength between two adjacent resonant conditions. A standard ring resonator possesses a linear dispersion relation which allows for equidistantly spaced adjacent modes. In comparison, the PhCRR's dispersion relation is markedly non-linear. The free spectral range of the PhCRR accordingly increases with increasing distance from the photonic band edge. In addition, the spatial bounding of the periodic dielectric structure enforces a frequency cutoff at the photonic band edge, beyond which no resonant mode can be found. As a result, the highest frequency (or equivalently, lowest wavelength) resonant mode will be found at the photonic band edge.

5.3 Step 3: Calculation of the photonic crystal lattice period

Once the band edge dimensionless frequency has been computed, the lattice constant of the photonic crystal can be determined using the following relations:

$$\nu_D = \frac{\nu_0 \cdot a}{c} \tag{5.5}$$

$$\lambda_0 \nu_0 = c \tag{5.6}$$

where ν_0 and λ_0 represent the physical frequency and vacuum wavelength, respectively. Combining these two equations yields an expression for the lattice constant of the photonic crystal:

$$a = \lambda_0 \nu_D \tag{5.7}$$

We see immediately that the photonic crystal design approach gives us a high degree of control over the resonant wavelength of the photonic band edge mode. The lattice constant of the periodic dielectric function is linearly proportional to the wavelength of the resonance. As a result, once the dimensionless frequency of a physical system has been calculated, we are afforded the flexibility of tuning the resonant wavelength of the photonic band edge mode solely by scaling the lattice constant accordingly.

It is also worth noting that we can choose to place a resonant mode of a desired wavelength *away* from the band edge simply by replacing the band edge dimensionless frequency with the frequency of a resonant condition found on either side of the photonic band edge. Herein lies the full potential of the design approach; we are not restricted to placing a resonance of a desired wavelength at the photonic band edge but, rather, have the flexibility to position the resonance in *any* region of interest along the dispersion relation. (see Section 6.5.1 for alternative engineering approaches which are of interest).

The final step in the design approach is to specify a desired radius for the photonic crystal ring resonator and then to calculate the number of units cells required to construct the ring resonator. Alternatively, we can fix a target number of unit cells and calculate the resulting radius of the resonator.

5.4 Example calculation

To illustrate the proposed design approach in practice, this section will be dedicated to an example calculation. Our goal is to design a photonic crystal ring resonator with an approximate radius of 2.5 microns. For reasons discussed in Section 2.2, we wish to design the photonic crystal ring resonator on the silicon-on-insulator platform. The target resonant wavelength for the device is 1550 nm, corresponding to the telecommunications transparency window.

We first model an infinitely long waveguide with width $w = 1.0$a and $ff = 0.3a$. The width of the waveguide is restricted to one lattice constant to avoid the introduction of higher order modes into the waveguide (see Section 2.2). The effective refractive index of the waveguide is set to a value of $n_{eff} = 2.83$, corresponding to a 220 nm thick silicon layer on a 2 μm silica substrate with air cladding. The MPB calculation of the photonic crystal waveguide yields a value of 0.2563 for the band edge dimensionless frequency (see Figure 5.5).

The lattice constant is calculated by taking the product of our dimensionless frequency with the target wavelength (Eq. 5.7)).

$$a = \lambda_0 \cdot \mu_D = (1550\text{nm})(0.2563) \simeq 397\text{nm} \tag{5.8}$$

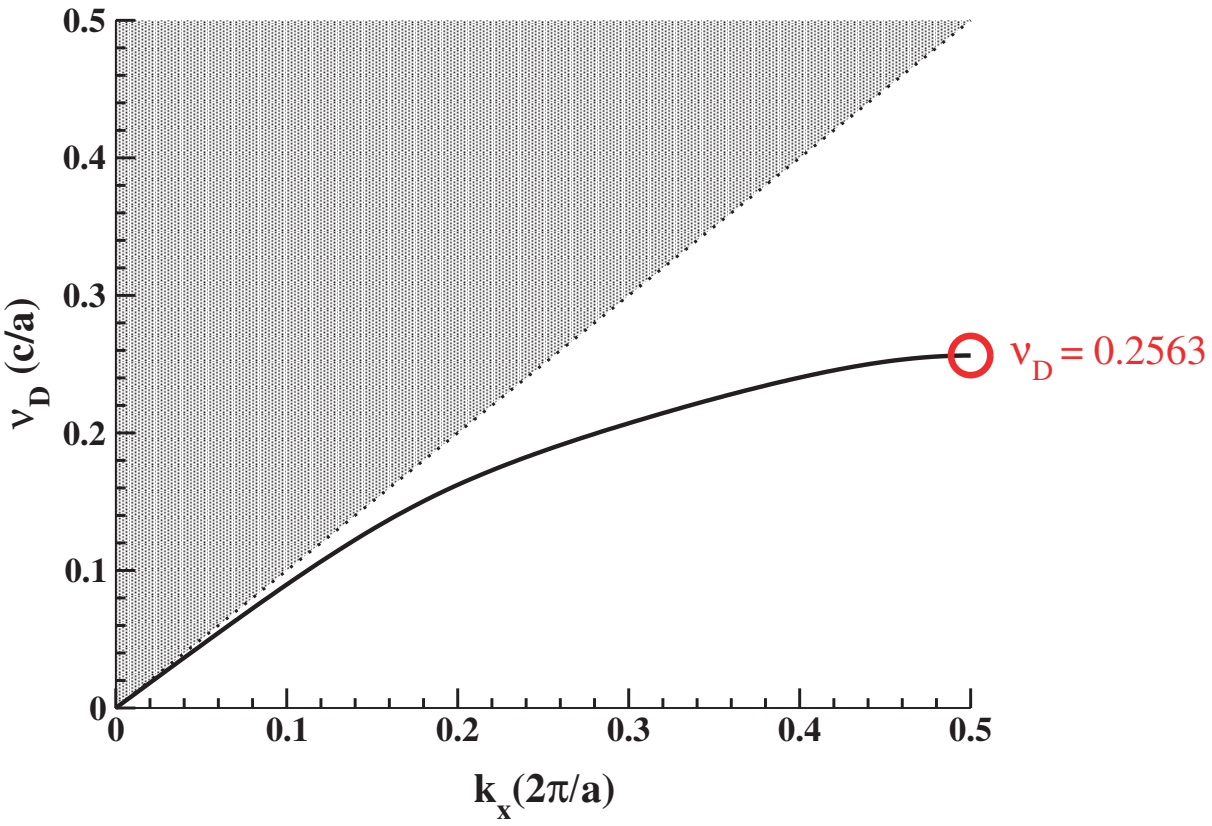

FIGURE 5.5: The first photonic band of a photonic crystal waveguide with $n_{eff} = 2.83$, $ff = 0.3$, and $w = 1.0$a. The photonic band edge dimensionless frequency is found at $\nu_D = 0.2563$

Using the computed value for a, we can in turn calculate the radius of the photonic crystal lattice holes ($r = 0.3a \simeq 119$ nm) and the width of the waveguide ($w = 1.0a = 397$ nm). The number of unit cells required to construct the PhCRR is then calculated using Eq. (5.1):

$$N = \frac{2\pi R}{a} = \frac{2\pi(2.5\mu\text{m})}{0.397\mu\text{m}} \approx 39.5 \tag{5.9}$$

In order to ensure a band edge resonant mode, we must round this number up to the closest even integer value, 40. Finally, the exact radius of the ring resonator is calculated, yielding a value of 2.527 μm.

Chapter 6

Computational verification of design approach

6.1 Spectral response of a photonic crystal ring resonator

In order to explore the time evolution of the electromagnetic fields in the designed photonic crystal ring resonator of Section 5.4, we will make use of the MIT Electromagnetic Equation Propagation software package [36] which utilizes a finite-difference time-domain computational approach to calculate the temporal change in the fields. A broadband Gaussian current dipole source is first employed to spectrally excite the electromagnetic fields. To avoid placing the excitation source in the node of a resonant mode, one current source is placed slightly off-set from the centre of a photonic crystal hole, while a second source is placed in the closest adjacent neighbouring hole (see Figure 6.1).

A 200 nm wide pulse is centered on 1550 nm, corresponding to the target band edge resonant wavelength of the device. Recall that our derivation of the electromagnetics master equation in Section 3.1 assumed the absence of free charge or current sources in the dielectric material. Consequently, we must allow for the current sources to decay to negligible values before computing the resulting field configurations.

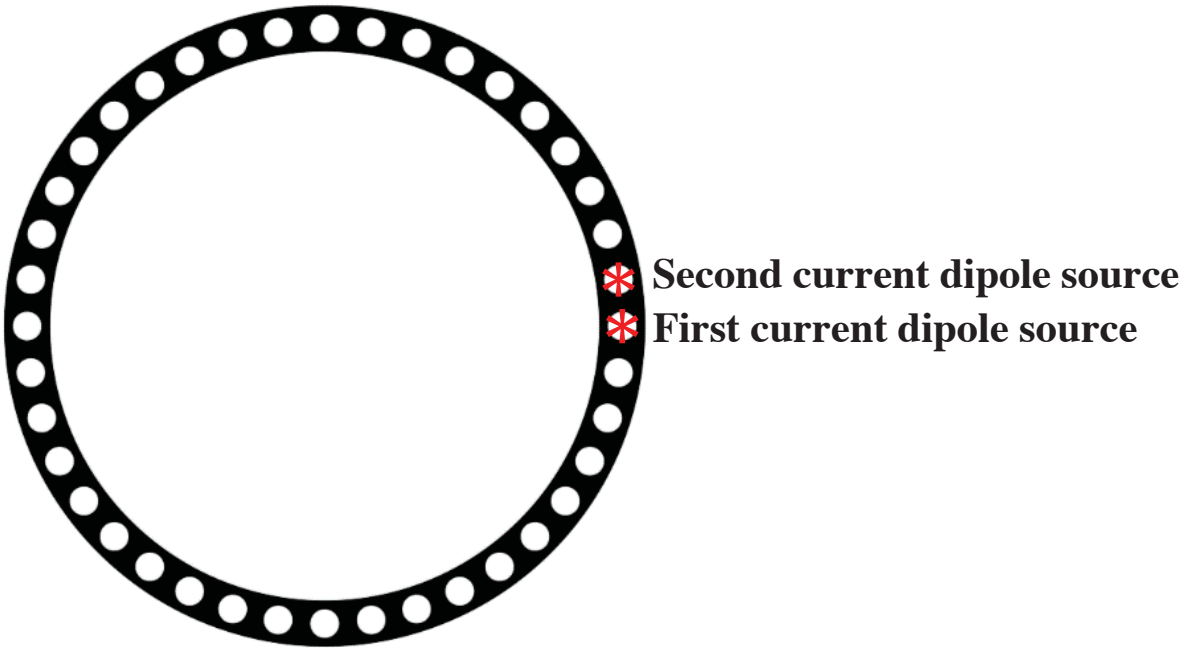

FIGURE 6.1: A photonic crystal ring resonator whose current dipole excitation source locations are indicated by red stars.

The broadband current source will excite a set of resonances whose magnetic fields satisfy Eq. (3.18). MEEP accordingly outputs the time evolution of a linear combination of these eigenfunctions. Because we are considering the transverse-electric configuration of the fields, we need only consider the z-component of the magnetic field, H_z. In order to extract the placement of each individual mode in the frequency domain, a discrete Fourier transform of the time evolution of the electric fields is performed.

The frequencies of each resonant mode can subsequently be confirmed via use of the open-source program, Harminv [37]. Given an input function comprised of a linear combination of sinusoidal functions, Harminv makes use of a harmonic inversion algorithm [38] to calculate the amplitudes, decay rates, phases, and frequencies of each sinusoid. The spectral response of our example photonic crystal ring resonator in the frequency domain extracted via Harminv can be seen in Figure 6.3. The photonic band edge mode is found at 1553 nm, a difference of $< 1\%$ from our expected target wavelength. Also as predicted, the free spectral range of adjacent modes increases with increasing distance from the photonic band edge. Furthermore, the predicted frequency cutoff due to the bounded nature of the photonic crystal ring resonator's dispersion relation is observed at the photonic band edge. In comparison, the calculated modes of a

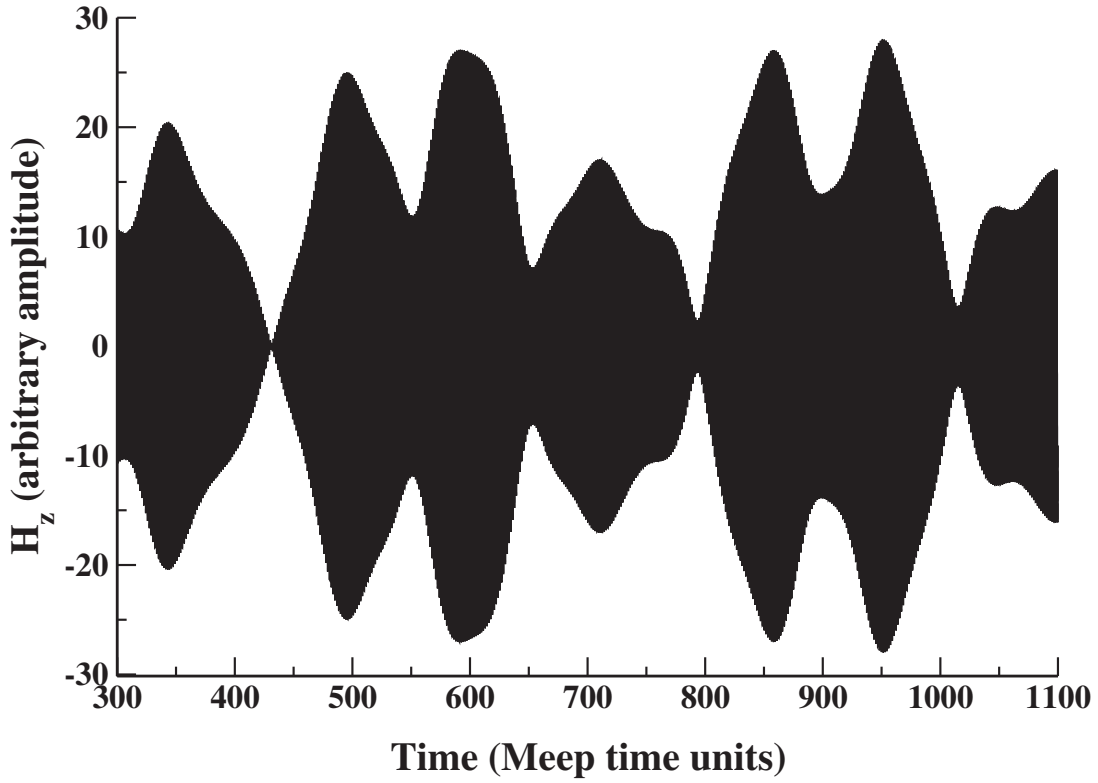

(A) Time evolution of the excited resonances of the example PhCRR.

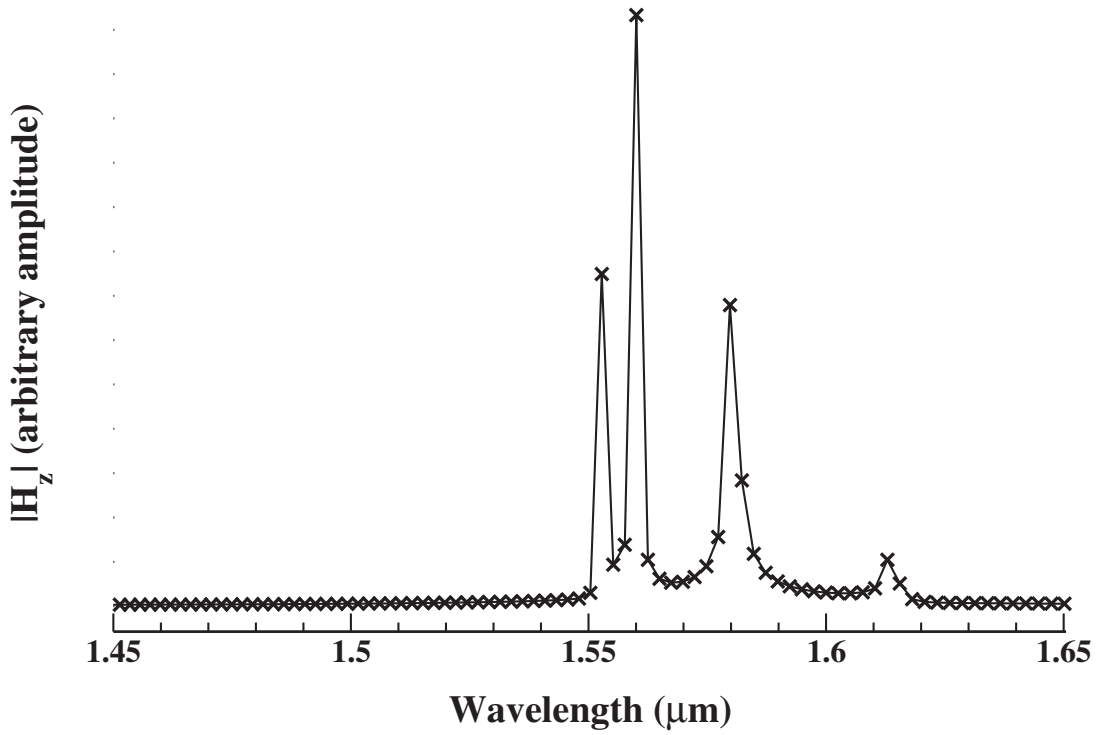

(B) Fourier transform of the electromagnetic fields from the time domain to the frequency domain. The resonances have been converted from frequency to wavelength using Eq. (5.7).

FIGURE 6.2: The time evolution of the excited electromagnetic fields of the photonic crystal ring resonator and its equivalent Fourier transform in the frequency domain computed via MEEP.

standard ring resonator display equidistance spacing between adjacent modes and no frequency cutoff.

Adjacent Mode Numbers	**Free Spectral Range**
$m = 20 \rightarrow m = 21$	7 nm
$m = 21 \rightarrow m = 22$	21 nm
$m = 22 \rightarrow m = 23$	34 nm

TABLE 6.1: Free spectral ranges of the example photonic crystal ring resonator from Section 5.4. Here the band edge mode at 1553 nm corresponds to a mode number of $m_{BE} = \frac{N}{2} = 20$.

6.2 Slow light enhancement of quality factors

In order to quantify the quality factors of each individual mode, a narrowband Gaussian source of width 5 nm[1] is centered on each resonant wavelength. Once the sources have died out, the resulting electromagnetic field corresponding to a particular mode is allowed to evolve until the square of the absolute value of the field has decayed to 90% of its initial value. The fields can then be analyzed in order to extract the quality factor of the mode in question. Due to decay mechanisms, such as scattering of the fields from imperfections on the surface of the resonator and coupling of guided modes to lossy radiation modes, the fields of the resonant modes will necessarily decay with time. For the transverse electric resonant modes for the example PhCRR in question, the optical losses of the fields can be described as:

$$H_z(x,t) = H_z(x)e^{(i\omega t)}e^{(-\frac{t}{\tau})} \tag{6.1}$$

.

Here τ quantifies the rate of optical losses of the resonator and is related to the quality factor by the equation:

$$Q = \frac{2\pi c \cdot \tau}{\lambda_m} \tag{6.2}$$

[1]In the case that adjacent modes are closely spaced to one another (i.e. their FSR $<$ 5 nm), a 5 nm-wide excitation pulse may be insufficient to individually resolve each mode. In such cases, a narrower pulse must be utilized.

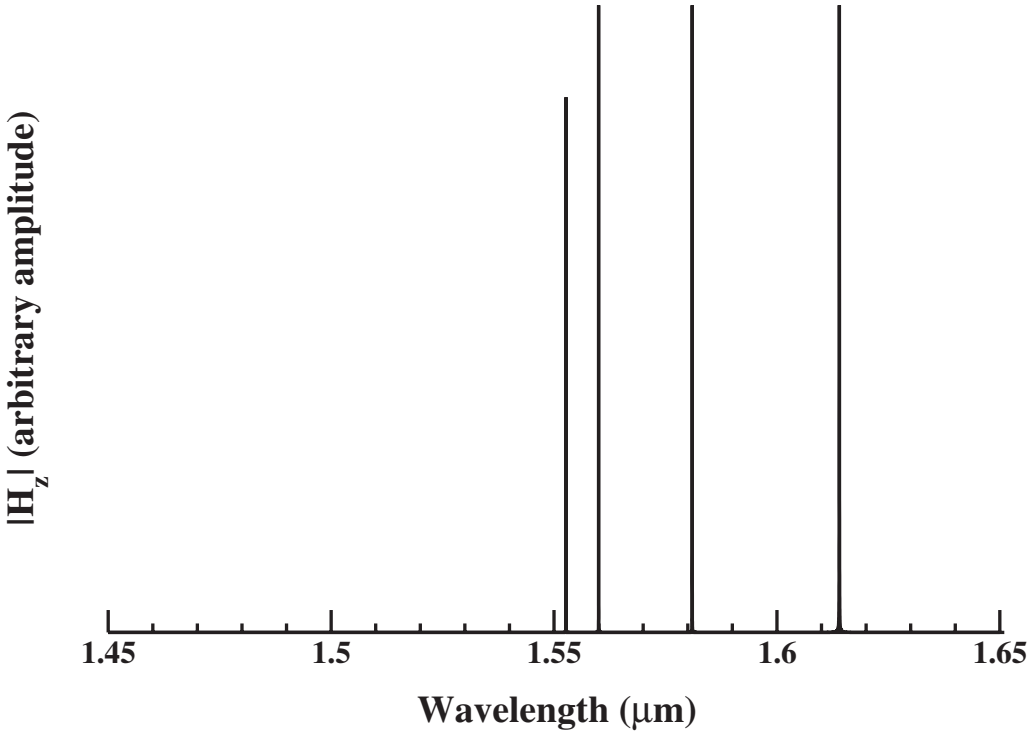

(A) Magnetic field spectrum of the resonant modes of the example PhCRR

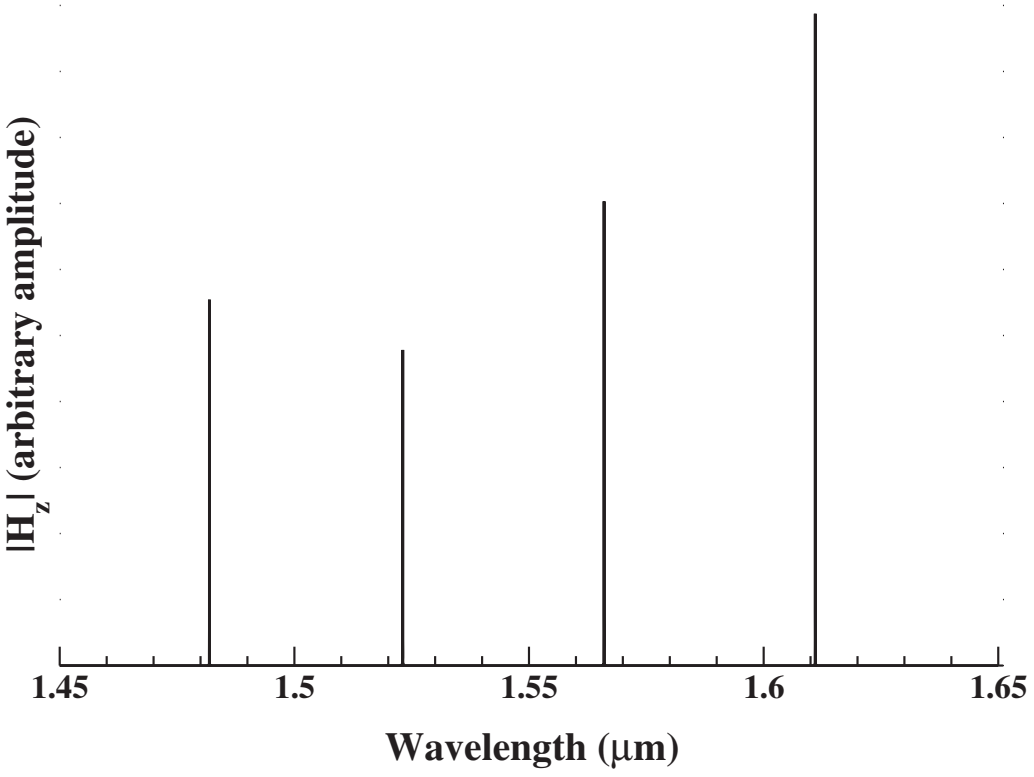

(B) Magnetic field spectrum of an equivalent standard ring resonator

FIGURE 6.3: Spectral responses of the example PhCRR and an equivalent standard ring resonator computed via the harmonic inversion algorithm program, Harminv.

Resonant Wavelength	**Exponential Decay Fit**	**Harminv**
1553 nm	2.59×10^7	1.30×10^7
1560 nm	1.29×10^7	1.19×10^7
1581 nm	1.59×10^6	3.88×10^6
1614 nm	3.16×10^5	3.02×10^5

TABLE 6.2: Quality factors of the resonant modes of the example photonic crystal ring resonator from Section 5.4.

where λ_m is the resonant wavelength of the mode under analysis. Once the time evolution of the electromagnetic fields have been calculated by MEEP, the optical loss envelope modifying the amplitude of the fields is extracted by isolating the local maxima of each oscillation (see Figure 6.4). A decaying exponential function is then fitted to this data, resulting in a fit parameter quantifying τ.

This value can in turn be inserted into Eq. (6.2) to calculate the quality factor for the resonance in question.[2] Verification of these values can be confirmed through comparison with the quality factors computed by Harminv.

Figure 6.5 demonstrates graphically the calculated quality factors for each resonant mode of the example photonic crystal ring resonator. The quality factors of the modes decrease away from the photonic band edge, confirming the prediction of slow light enhancement of quality factors.

6.3 Mode profiles of resonant modes

To obtain the field profiles of each resonance, the z-component of the magnetic field is plotted. The field profiles of the fundamental, photonic band edge mode demonstrate confinement of the electromagnetic fields to the core of the photonic crystal ring resonator. Additionally, the strength of the fundamental mode's electric field is concentrated in the high refractive index material of the silicon core, consistent with our discussion in Section 3.3.

[2]Note that the value for τ obtained from analysis of the fields is in MEEP time units and therefore must be converted to physical time units (i.e. seconds) before being applied to Eq. (6.2).

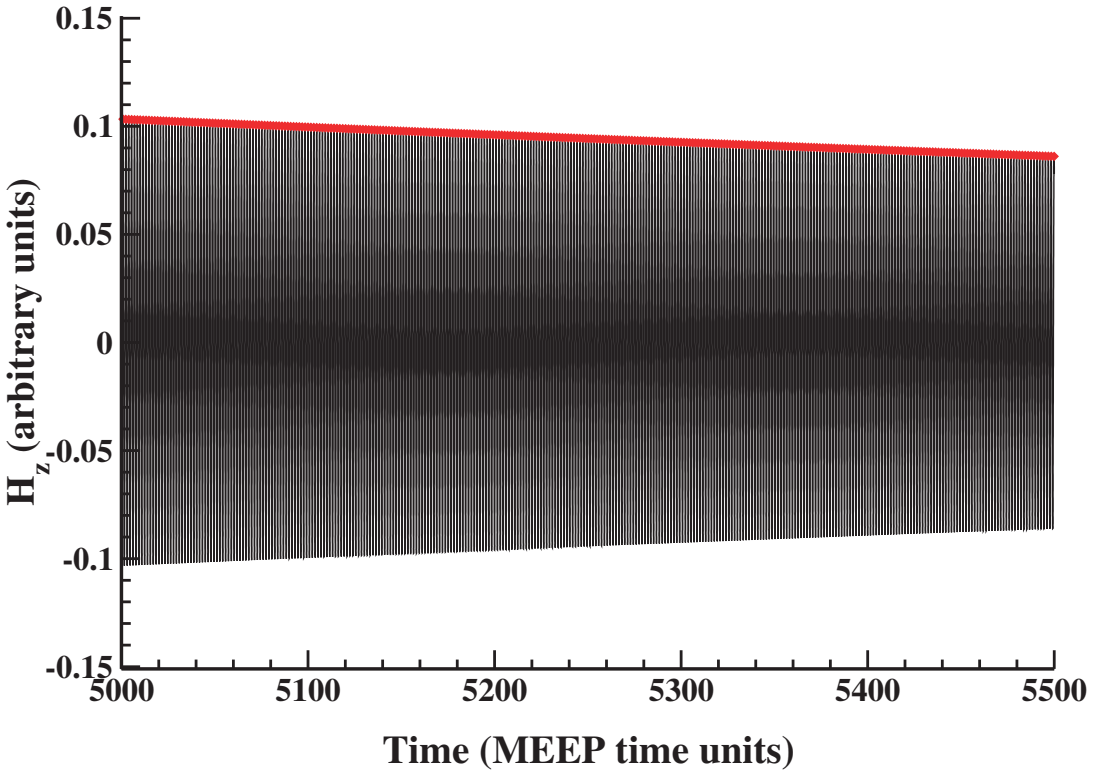

(A) Exponential decay of the H_z fields of the example photonic crystal ring resonator.

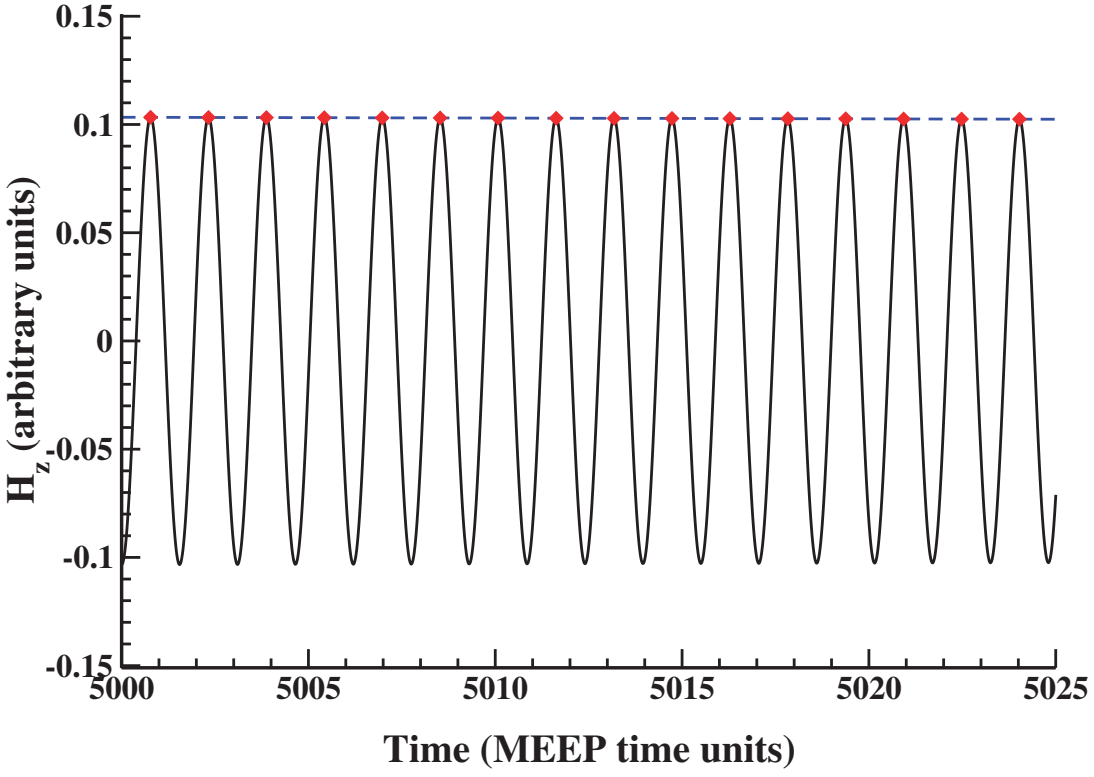

(B) Close-up of the decay over 25 MEEP time units. The optical loss envelope is indicated in red, while the exponential function fit to the data is indicated by the blue dashed line.

FIGURE 6.4: Exponential decay of the magnetic fields of the example photonic crystal ring resonator

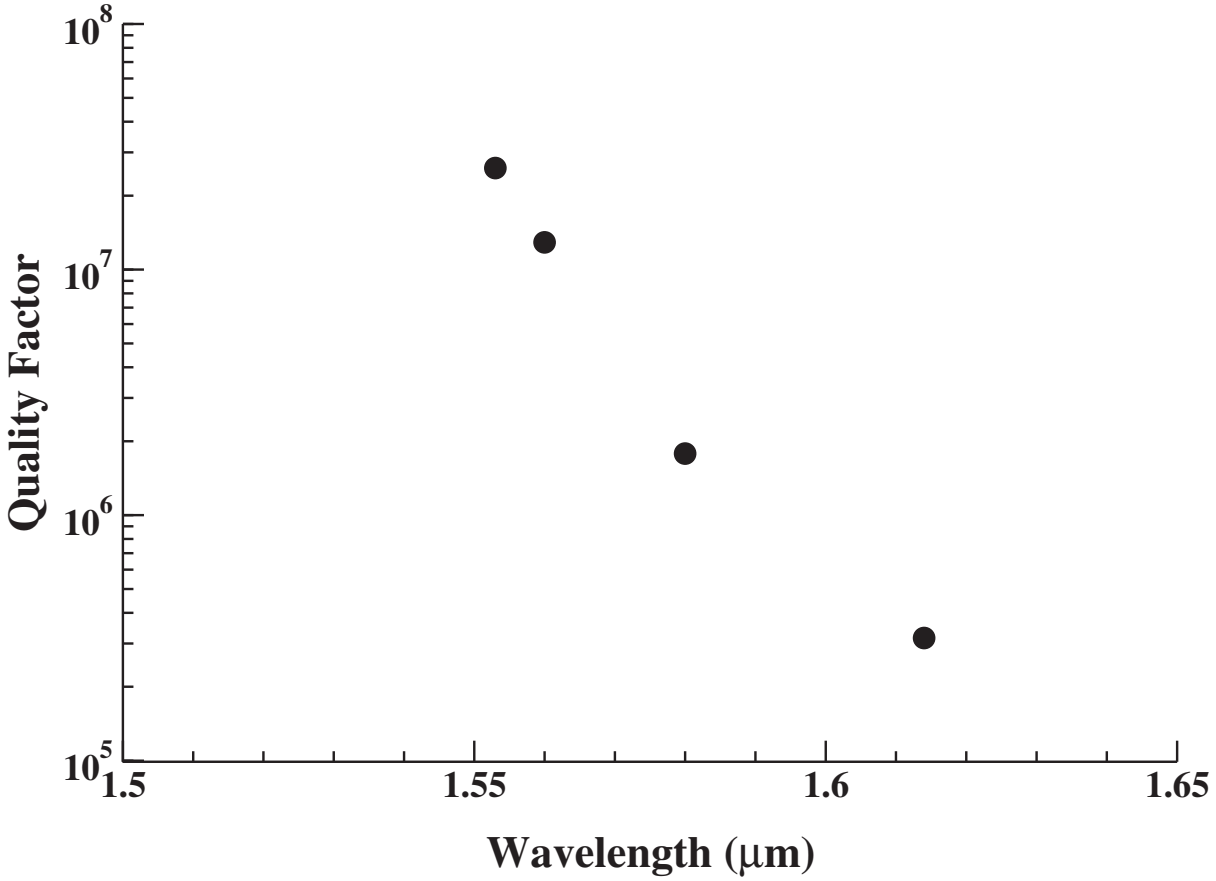

FIGURE 6.5: Calculated quality factors of the example photonic crystal ring resonator

6.3.1 Spatial beating due to symmetry of photonic dispersion relation

The resonant modes found away from the band edge all demonstrate a unique spatial beating in their field configurations. This beating is due to the symmetry of the photonic crystal ring resonator's dispersion relation about the photonic band edge. This symmetry allows for a degenerate set of clockwise and counterclockwise propagating eigenmodes, corresponding to wave vectors $k_{x_+} > 0$ and $k_{x_-} < 0$, respectively. As discussed in Section 3.2, the set of eigenfunctions of a Hermitian operator are complete. Accordingly, a standing wave eigenfunction composed of a linear combination of the clockwise and counterclockwise propagating modes will also satisfy the electromagnetic eigenvalue problem. Any mode found away from the band edge can thus be represented either as a traveling wave or a standing wave. The linear combination of the degenerate set of eigenfunctions can be described as:

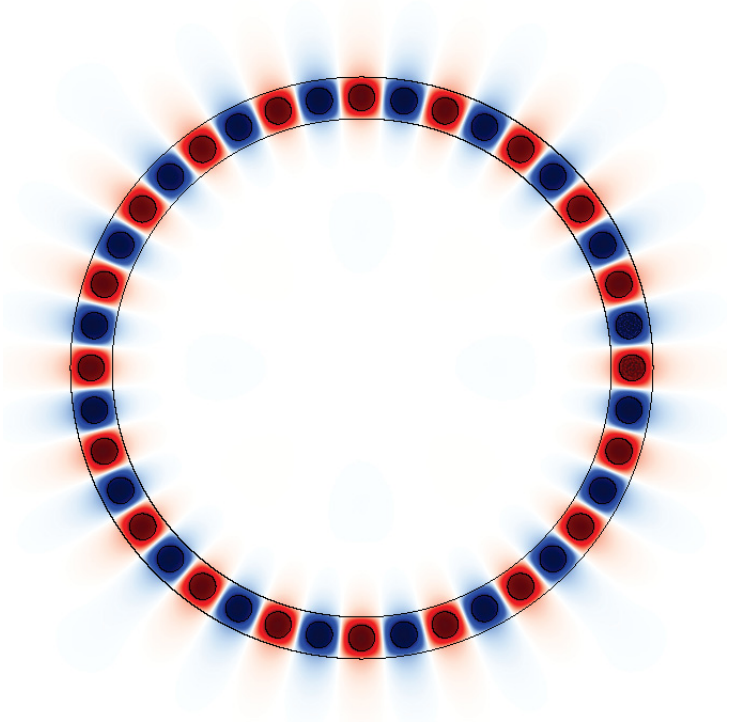

(A) H_z of the photonic band edge mode of the example photonic crystal ring resonator with $\lambda = 1553$ nm.

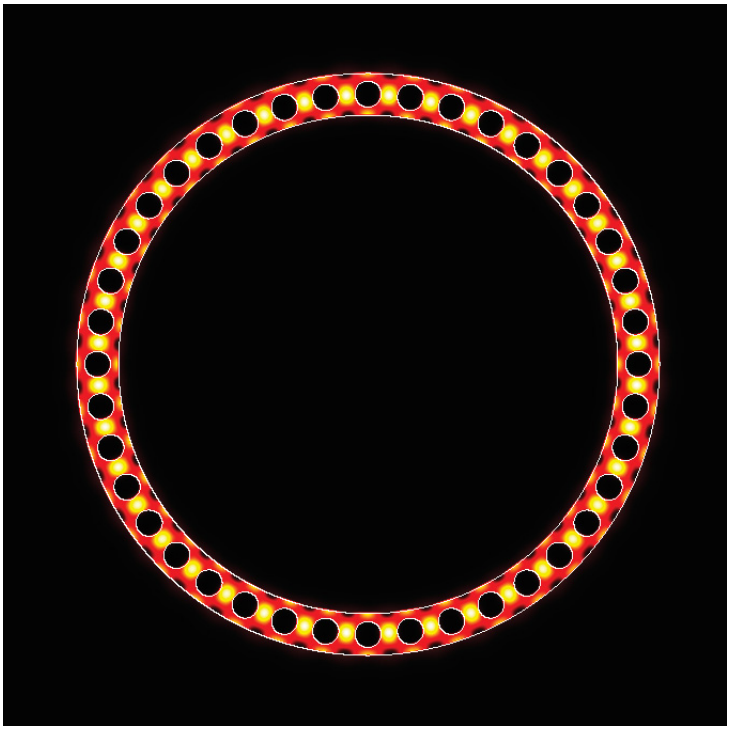

(B) $|\mathbf{D}|^2$ of the photonic band edge mode. The electric field density is found concentrated in the high refractive index material of the silicon core of the ring resonator.

FIGURE 6.6: The magnetic field profile and electric field energy density of the PhCRR's fundamental, band edge resonant mode.

$$H_z \propto e^{i(k_{x_+}x)} + e^{i(k_{x_-}x)} \tag{6.3}$$

Combining Eq. (6.3) with Eqs. (5.3) and (5.1) allows us to represent the linear combination of the degenerate set of eigenfunctions in terms of their mode numbers. For the N-even configuration, we can quantify the clockwise propagating mode number as $m_{k_{x_+}} = m_{BE} + p$ and the counterclockwise propagating mode number as $m_{k_{x_-}} = m_{BE}$ - p (where $p \in \mathbb{Z}$). Eq. (6.3) can be thus be rewritten as:

$$\begin{aligned} H_z &\propto e^{i\left(\frac{2\pi(m_{BE}+p)}{Na}x\right)} + e^{i\left(\frac{2\pi(m_{BE}-p)}{Na}x\right)} \\ &\propto e^{i\left(\frac{m_{BE}}{R}x\right)}\left(e^{i\left(\frac{2\pi p}{Na}x\right)} + e^{i\left(\frac{-2\pi p}{Na}x\right)}\right) \\ &\propto e^{i\left(\frac{m_{BE}}{R}x\right)}\cos\left(\frac{2\pi p}{Na}x\right) \end{aligned} \tag{6.4}$$

An examination of Eq. (6.4) provides a deeper understanding of the spatial beating seen in the resonant modes found away from the band edge. The exponential function represents the field configuration of the fundamental band edge mode, while the cosine function modulates the strength of the electromagnetic field. The argument of the cosine depends on the integer p, which quantifies the displacement of the mode from the band edge. Note that for the N-even configuration, only an **even** number of nodes is allowed.

Our analysis can be expanded to include photonic crystal ring resonators composed of an odd number of unit cells. Similar to the N-even configuration, a PhCRR with an N-odd configuration also possesses a symmetric dispersion relation about the band edge. The mode numbers of the clockwise and counter-clockwise propagating modes can be represented as:

$$\begin{aligned} m_{k_{x_+}} &= \frac{(N-1)}{2} + p \\ m_{k_{x_-}} &= \frac{(N-1)}{2} - p \end{aligned} \tag{6.5}$$

Inserting Eq. (6.5) into Eq. (6.3) yields:

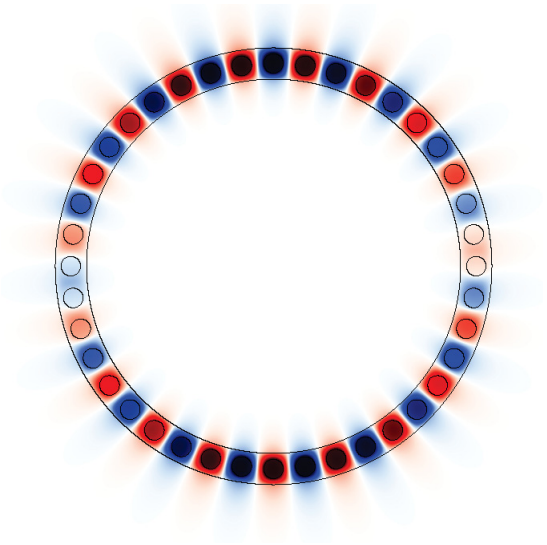

(A) H_z of the dipole mode with $\lambda = 1.560$ nm.

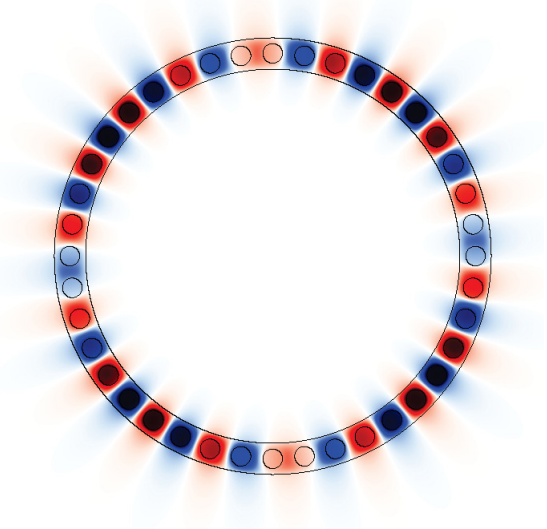

(B) H_z of the quadrupole mode with $\lambda = 1.581$ nm.

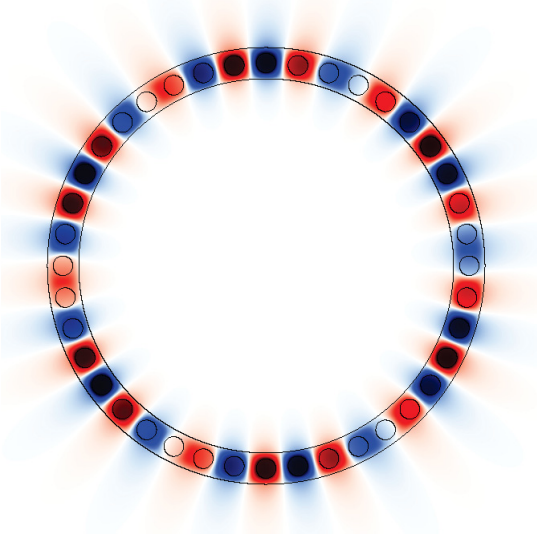

(C) H_z of the hexapole mode with $\lambda = 1.614$ nm.

FIGURE 6.7: Magnetic field configurations of the photonic crystal ring resonator's modes for the N-even configuration.

$$H_z \propto e^{i(\frac{m_{BE}}{R}x)} \cos\left(\frac{2\pi(p+1)}{Na}x\right) \tag{6.6}$$

We can again describe the field configurations as the product of the band edge field configuration and a modulating cosine function. Contrary to the N-even configuration, however, Eq. (6.6) only allows for an *odd* number of nodes (see Figure 6.8 for illustration).

6.3.2 Electric field densities of higher order resonances

Due to the orthogonality requirements of eigenfunctions satisfying the electromagnetics master equation, higher-order modes are required to decrease the concentration of their electric field densities in the high index material holes. The resulting electric field densities for the first three higher-order modes of the photonic crystal ring resonator can be seen in Figure 6.9.

6.4 Source symmetry requirements

It can be observed that the nodes of the fields are slightly offset from the $\hat{x}$- and $\hat{y}$-axes. This can be explained by recalling the placement of the sources described in Section 6.1. The sources are placed in a manner which creates an axis of symmetry which is oriented at a 4.5° angle away from the $\hat{x}$-axis. If possible, field configurations must respect the symmetry conditions imposed by the sources. Because the sources used to excite the fields of our example PhCRR are symmetric (i.e. identical), the magnetic field configurations can be described as **even**[3], implying that [21]:

$$H_z(x, y) = H_z(-x, -y) \tag{6.8}$$

[3]The magnetic field, **H** transforms as a pseudovector under symmetry operations, as opposed to the electric field, **E**, which transforms as a vector. Consequently, an even mode for an electric field is defined as

$$\mathbf{E(r)} = \mathbf{-E(-r)} \tag{6.7}$$

.

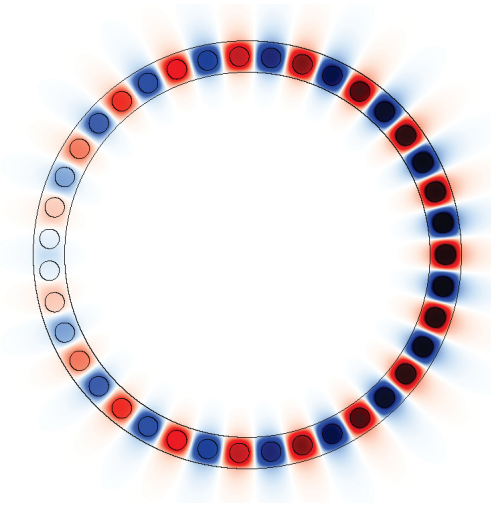

(A) H_z of the monopole mode with $\lambda = 1.555$ nm.

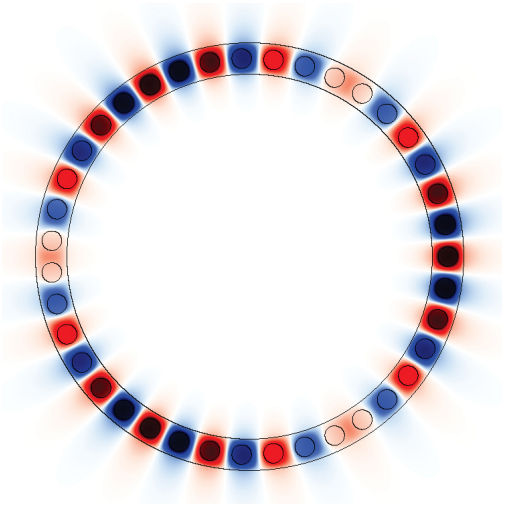

(B) H_z of the tripole mode with $\lambda = 1.600$ nm.

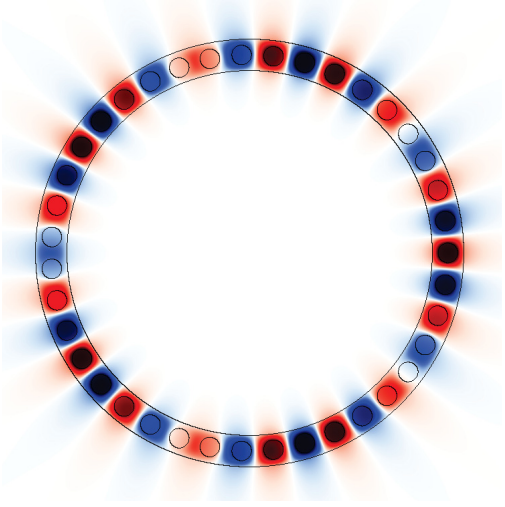

(C) H_z of the pentapole mode with $\lambda = 1.571$ nm.

FIGURE 6.8: Magnetic field configurations of the photonic crystal ring resonator's modes for the N-odd configuration.

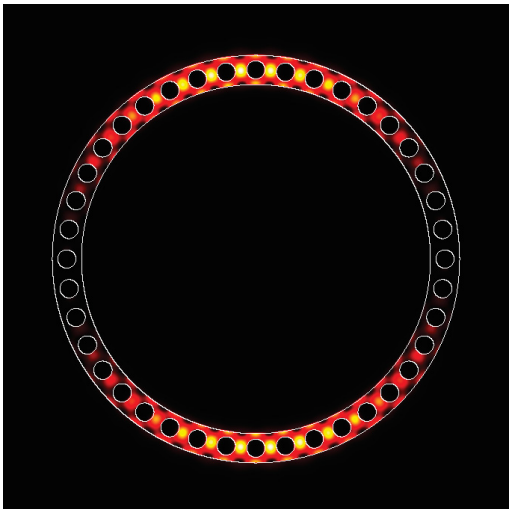

(A) $|\mathbf{D}|^2$ of the dipole mode with $\lambda = 1.560$ nm.

(B) $|\mathbf{D}|^2$ of the quadrupole mode with $\lambda = 1.581$ nm.

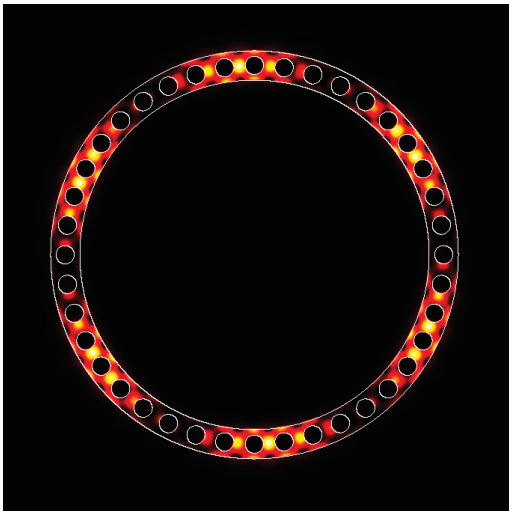

(C) $|\mathbf{D}|^2$ of the hexapole mode with $\lambda = 1.614$ nm.

FIGURE 6.9: Electric field densities of the first three higher-order modes of the photonic crystal ring resonator. Decreasing concentrations of the electric field density are found in the high index material holes as compared to the electric field density of the fundamental mode.

If the sources are anti-symmetric, signifying that they possess equal but opposite magnitudes, the resulting magnetic field configuration will be **odd**[4] with respect to the axis of symmetry. An odd configuration can be described as:

$$H_z(x, y) = -H_z(-x, -y) \tag{6.10}$$

Figure 6.10 demonstrates the different mode families which can be excited in our example photonic crystal ring resonator simply by adjusting the placement and symmetry of the excitation sources. Here we have placed a set of symmetric and anti-symmetric sources in the centre of the 1^{st} and 21^{st} periodic elements, creating an axis of symmetry about the $\hat{y}$-axis. For the symmetric configuration, we find that only the fundamental, quadrupole, and octapole modes are excited, as they are the only modes that respect the even symmetry conditions imposed by the symmetric set of sources. Alternatively, the anti-symmetric set of sources excites only the odd modes (i.e. the dipole, hexapole, and decapole modes) of the photonic crystal ring resonator.

6.5 Geometric disorder

As mentioned in Section 6.2, a photonic crystal ring resonator will undergo optical losses due to geometric disorder of the resonator. These losses can be attributed to two main mechanisms. In practice, it proves impossible to fabricate perfectly smooth surfaces defining the dielectric interfaces of the PhCRR. Indeed, optical losses due to **surface roughness** are observed even in our computational model due to the discretization of the computational grid. Section 6.5.1 will be dedicated to exploring the impact of surface roughness and its effect on the resonator's quality factors.

Secondly, **non-uniformity of the photonic crystal** structure of the resonator breaks the perfect periodicity of the PhCRR's dielectric function. The consequences (both positive and negative) of periodicity breaking will be further discussed in Section 6.5.2 .

[4] Again, the vector nature of the electric field under symmetry operations requires an odd mode of an electric field to be represented as

$$\mathbf{E(r) = E(-r)} \tag{6.9}$$

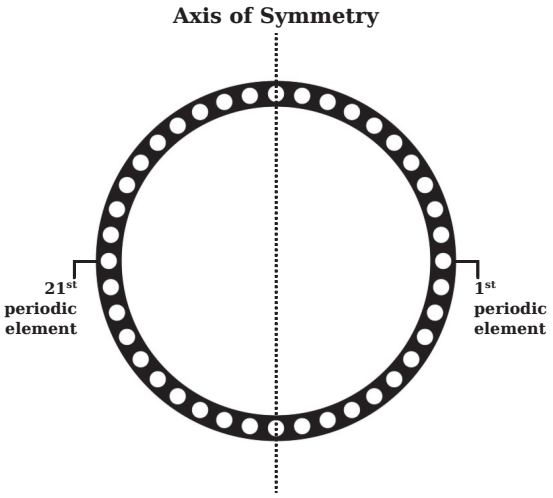

(A) The location of current dipole excitation sources utilized to excite the PhCRR's resonances. The sources are placed in the centre of the 1^{st} and 21^{st} periodic elements, while the axis of symmetry of the photonic crystal ring resonator is indicated by a dashed line.

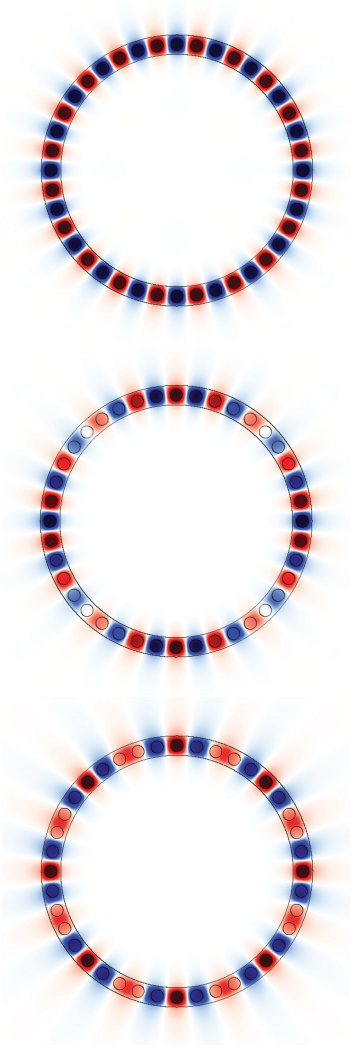

(B) The **even modes** of a photonic crystal ring resonator excited by a **symmetric** pair of current dipole sources.

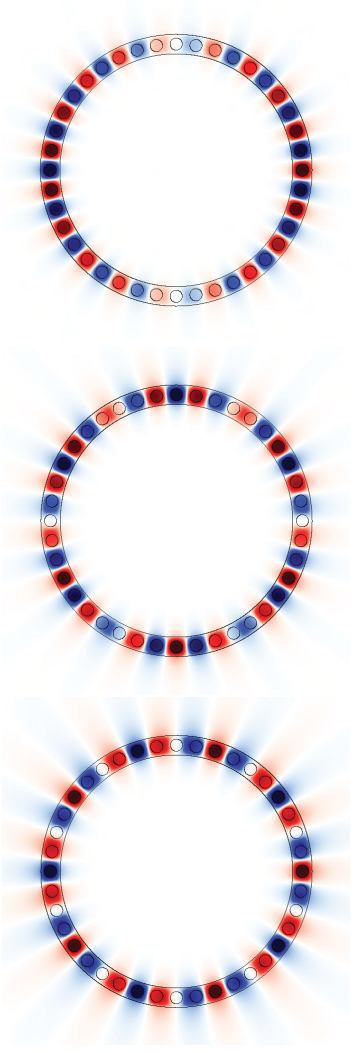

(C) The **odd modes** of a photonic crystal ring resonator excited by an **anti-symmetric** pair of current dipole sources

FIGURE 6.10: The excited resonances of a photonic crystal ring resonator under even and odd source symmetry requirements

6.5.1 Surface Roughness

Fabrication techniques at the forefront of current manufacturing technologies have successfully reduced fabrication-induced surface roughness to less than 2 nm RMS [39]. Despite these tight fabrication tolerances, scattering of propagating electromagnetic waves in a photonic crystal ring resonator will necessarily introduce optical losses to the system. It has been theoretically and experimentally verified that backscattering losses due to the presence of scatterers on the surface of a resonator scales as the square of the group index [18,40,41] in the slow light regime. Recall from Eq. (4.4) that the group index of a material is inversely proportional to the group velocity of a propagating wave; consequently, a slow light resonance possesses an extremely high group index. Surface roughness induced losses thus present a substantial hurdle in the design of slow light resonant modes.

To determine the effect of surface roughness on the quality factors of our example photonic crystal ring resonator, random scatterers are placed on the surface of the resonator and the resultant quality factors are subsequently measured. For our example photonic crystal ring resonator, we will model a surface roughness of approximately 3 nm along the edges of the waveguide interfaces. Computational limitations prevent us from extending our analysis to include roughness along the edges of the photonic crystal holes; the resulting calculated quality factors will therefore be slightly higher than what can be expected in practice. As seen in Figure 6.11, all of the resonant modes demonstrate the predicted decrease in quality factors. However, the effect is most pronounced at the photonic band edge, resulting in a decrease of the quality factors by a factor of nearly 80.

Moreover, backscattering mechanisms can significantly alter the frequency response of a photonic crystal ring resonator. Defects found on the surface of the PhCRR backscatter resonances, arising in coupling between the propagating and counterpropagating modes [42]. This coupling breaks the degeneracy of the propagating and counterpropagating resonances, resulting in a splitting of the corresponding eigenvalues of each mode. Evidence of this process is found through examination of the spectral response of a PhCRR with simulated surface roughness, which exhibits a small, yet finite, splitting of frequency eigenvalues. Furthermore, because the split modes now correspond to distinct eigenvalues, the field configurations (or, equivalently,

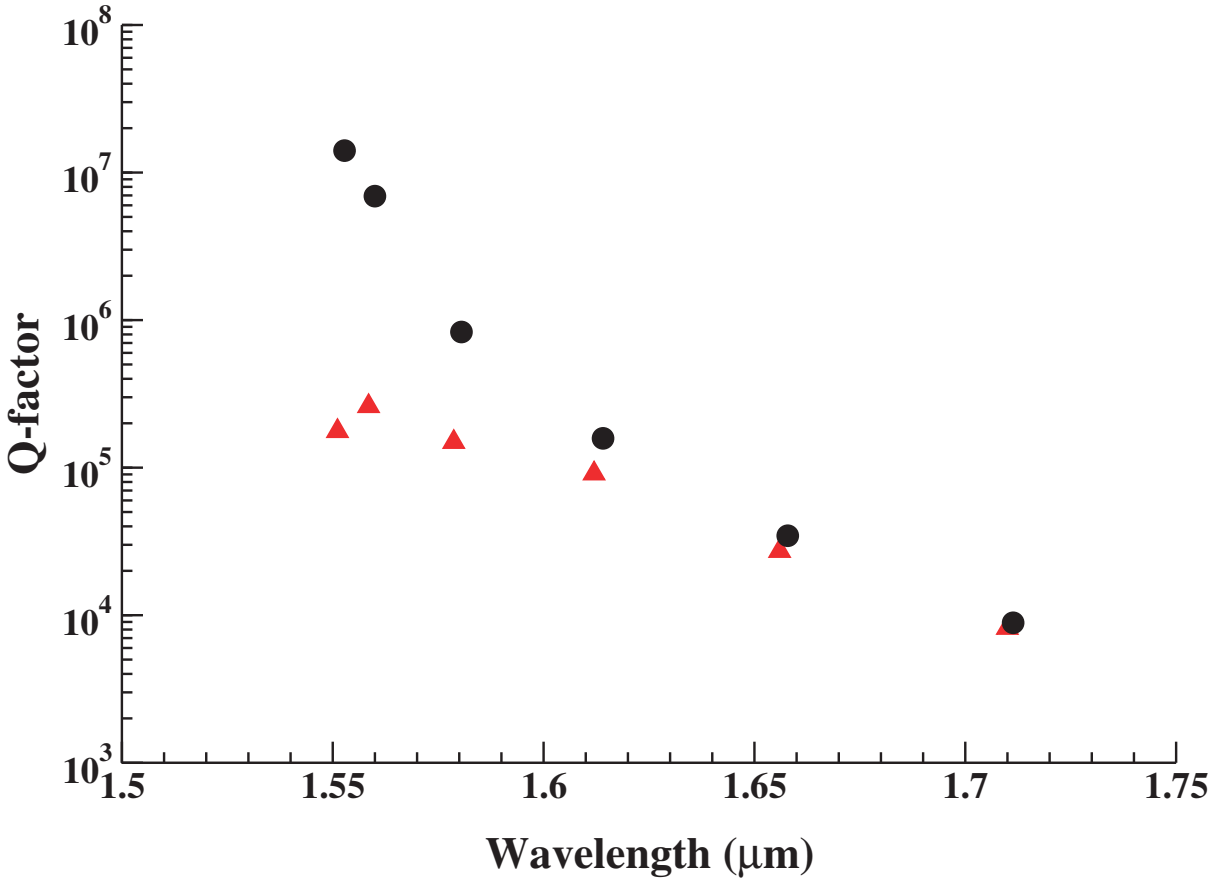

FIGURE 6.11: Quality factors of the resonant modes of the example PhCRR. The black circles indicate the quality factors of the resonator when effects due to surface roughness are neglected, while the red triangles quantify the reduction in quality factors when a surface roughness of scatterers of 3 nm in radius with a density of 2000 scatterers per micron is considered.

the eigenfunctions) must rearrange themselves so as to satisfy the orthogonality requirement specified in Section 3.2.

In addition to the decrease in quality factors of the photonic band edge mode and modification of the spectral profile of the PhCRR, the group velocity dispersion of the photonic crystal ring resonator offers key insights into the roughness induced obstacles facing slow light resonant modes. The group velocity dispersion (D_λ) indicates the amount a light pulse will distort per unit length of propagation and is described as [43]:

$$D_\lambda = -\frac{2\pi c}{\lambda^2}\frac{d^2k}{d\omega^2} \tag{6.11}$$

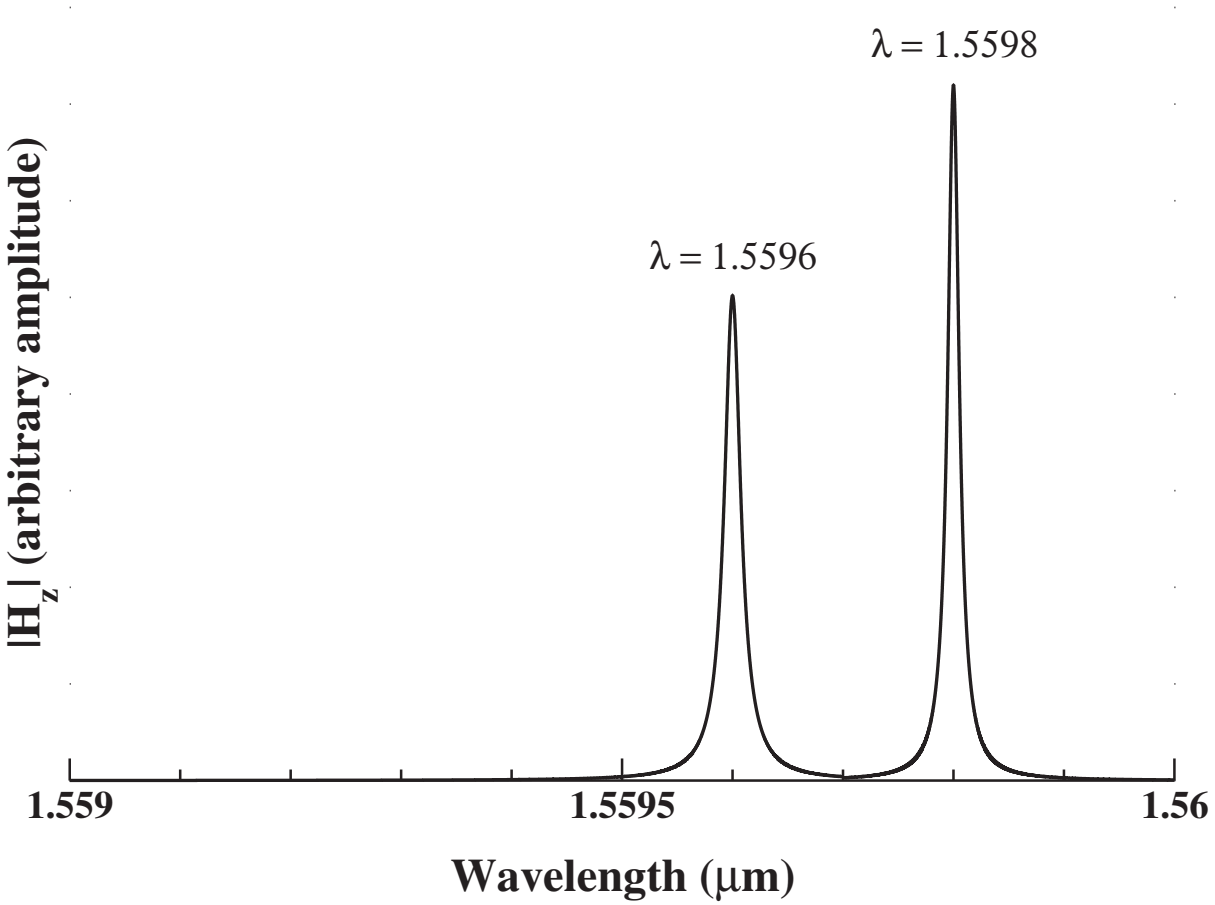

(A) Splitting of the dipole degenerate modes due to surface-induced roughness of the photonic crystal ring resonator

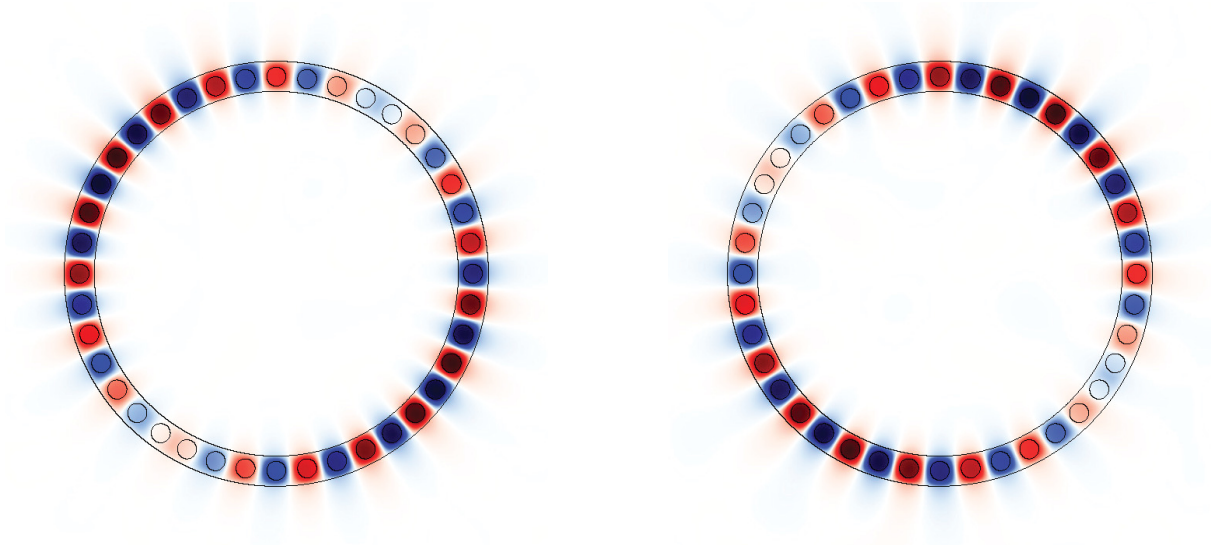

(B) Orthogonal magnetic field configurations (H_z) of the dipole split mode

FIGURE 6.12: The spectral response and magnetic field configurations for the dipole split mode for a photonic crystal ring resonator with simulated scatterers of 3 nm in radius and a density of 2000 scatterers per micron.

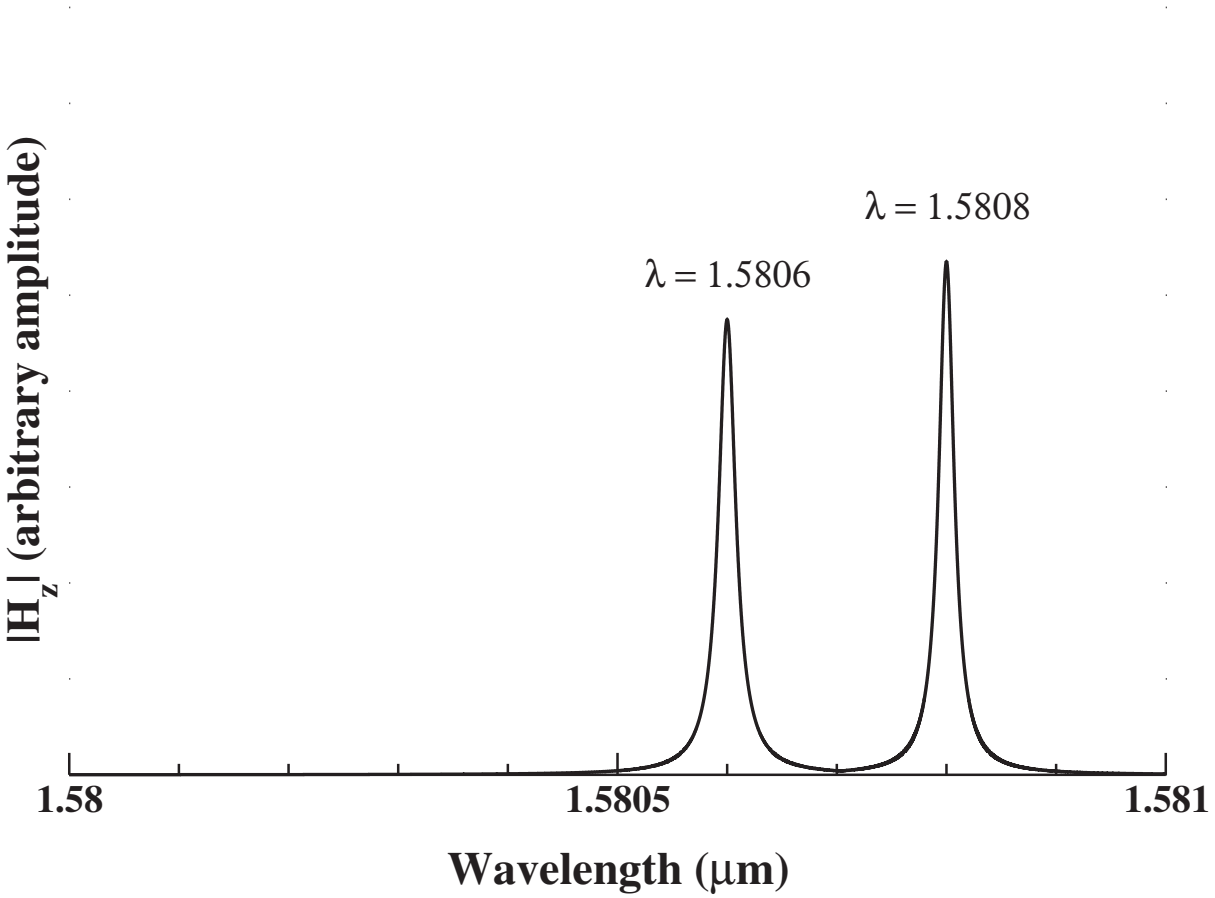

(A) Splitting of the quadrupole degenerate modes due to surface-induced roughness of the photonic crystal ring resonator

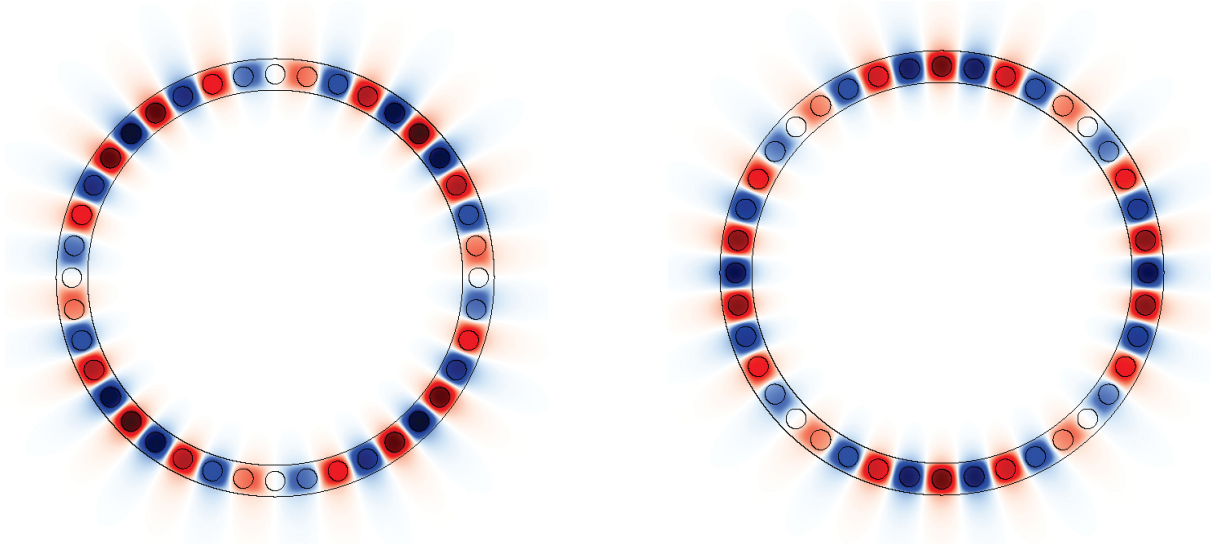

(B) Orthogonal magnetic field configurations (H_z) of the quadrupole split mode

FIGURE 6.13: The spectral response and magnetic field configurations for the quadrupole split mode.

Figure 6.14b demonstrates the divergence of the group velocity dispersion of the PhCRR at the photonic band edge. This indicates that a band edge resonant light pulse in a photonic crystal ring resonator will be severely distorted due to the slow light effects of the device.

The combined ramifications of increased optical losses, modification of the spectral profile of the PhCRR, and the distortion of optical pulses due to surface roughness may outweigh the enhancement of quality factors found directly at the photonic band edge. However, several potential solutions exist which offer promising resolutions to the problems in question. Recall from Section 5.3 that the proposed design approach can be modified to place a resonant mode of a desired wavelength not only at the photonic band edge, but in **any region** of the dispersion relation that is of interest. As a result, we have the capability to place our desired resonance slightly offset from the band edge, where the unfavourable effects due to surface roughness induced losses are lessened. It has been shown that roughness induced backscattering is the dominant loss mechanism for group velocities lower than $\frac{c}{100}$, however these losses are significantly reduced away from the photonic band edge. Resonant modes exhibiting moderate slow light behaviour (i.e. modes possessing group velocities on the order of $\frac{c}{20}$) have optical losses which scale linearly with group index [44]. It may thus prove possible to find an optimal trade-off between slow light enhancement of resonant modes near the photonic band edge and optical losses due to the high group indices of said modes.

Furthermore, several research efforts have achieved promising results in engineering slow light regions of the photonic dispersion relation via anti-crossing of coupled modes [45, 46]. These "loss-engineered" regions possess low group indices and group velocity dispersion parameters, while maintaining slow light enhancement of resonant modes. In particular, mode coupling between even and odd resonances has been achieved via group theory analysis [47]. Engineered anti-crossing regions due to group symmetries may prove to be particularly interesting due to the geometric properties of photonic crystal ring resonators. It remains to be seen whether the modes of a PhCRR can be coupled in a manner which will allow for anti-crossing slow light regions of the photonic dispersion curve which break the unfavourable association between slow light and high optical losses and pulse distortion due to surface roughness.

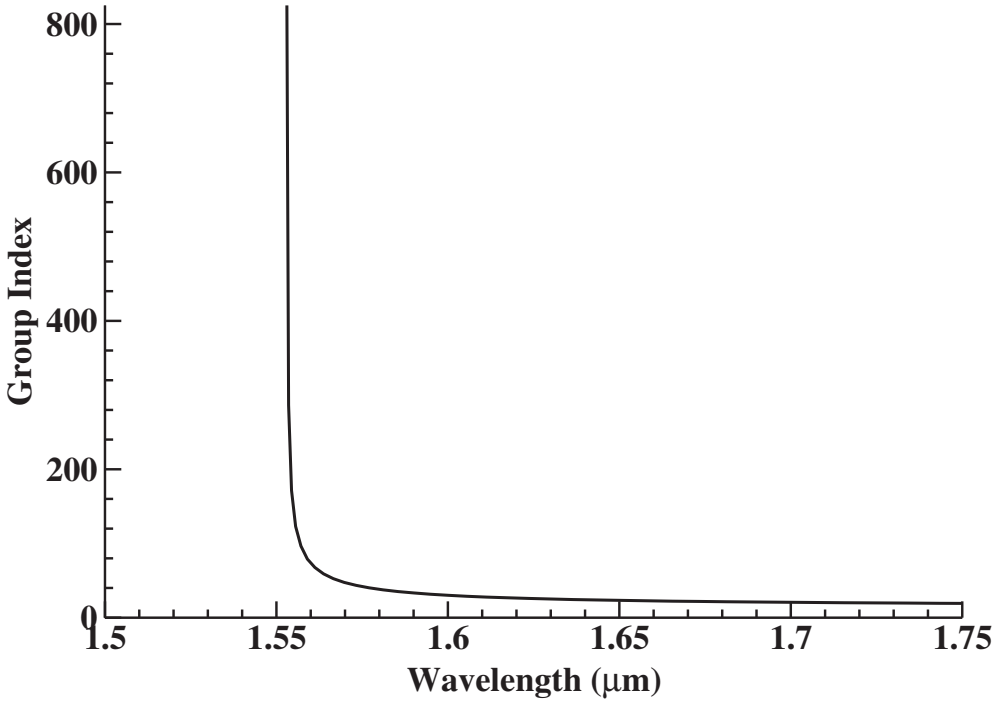

(A) Group index of the example photonic crystal ring resonator

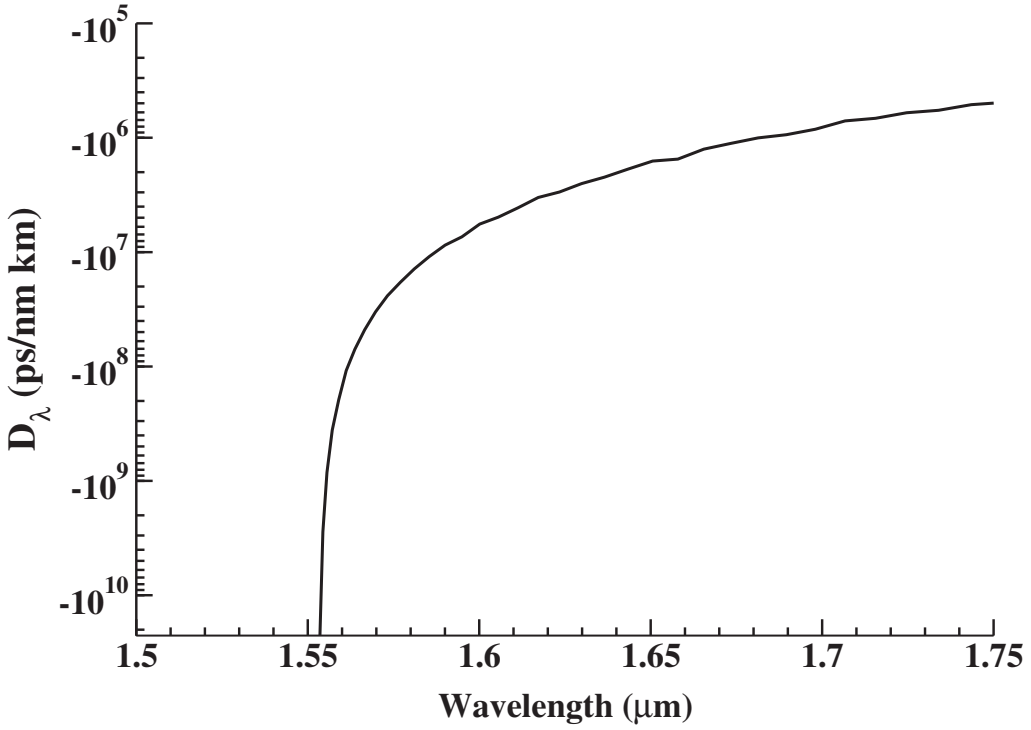

(B) The group velocity dispersion (D_λ) of the example photonic crystal ring resonator

FIGURE 6.14: The group index and D_λ of the example photonic crystal ring resonator. Both parameters diverge at the photonic band edge due to the zero group velocity of the slow light resonant modes.

6.5.2 Non-uniformity of photonic crystal lattice

Additional optical losses will be introduced into the system due to random geometric variations in the photonic crystal hole lattice or waveguide thickness during fabrication [48]. In theory, a break in the periodicity of the photonic crystal lattice renders our derivation of the design approach in Section 5.2 ineffectual. Nevertheless, if we consider only small variations of the periodic dielectric function, we can consider the non-uniformity of the photonic crystal lattice as a small perturbation of the system, which will introduce optical losses into the system rather than qualitatively alter our analysis of the mode structure of the photonic crystal ring resonator.

Optical losses due to non-uniformity of the photonic crystal lattice structure can be integrated into our computational analysis by randomly altering the radius of the low index material holes. Figure 6.15a demonstrates the effect that increasing geometric variations of the photonic crystal lattice have upon the quality factors of the photonic band edge mode. Variations as small as 1% are substantial enough to reduce the quality factor of the band edge mode by one order of magnitude. It is thus necessary to select fabrication platforms which offer high resolution and low fabrication variations in order to produce high quality factor resonators. Certain fabrication techniques have already been shown to fall within these tolerances [44].

Increasing geometric disorder can also lead to Anderson localization of the fields, as seen in Figure 6.15 [49, 50] . It may, however, prove possible to utilize this localization of fields to our gain. Engineering of the variation in the hole radius can provide control over this effect, allowing for the design of slow light nanocavity resonant modes possessing high-intensity localized fields [51, 52].

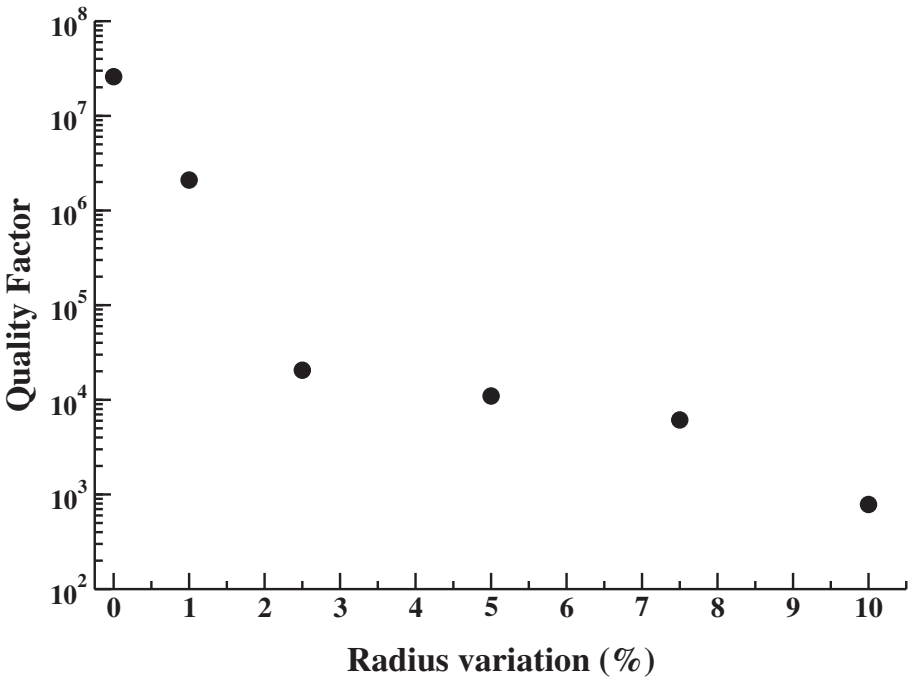

(A) Quality factors of the photonic crystal ring resonator as a function of the radius variation in the low index material holes.

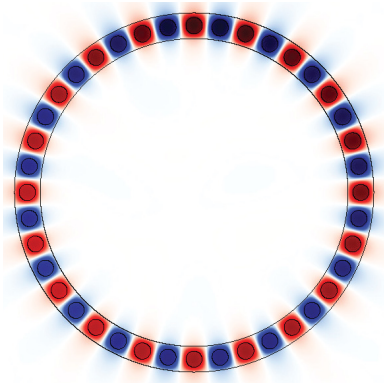

(B) H_z of the fundamental mode of the PhCRR with a **1% radius variation** of the low index material holes.

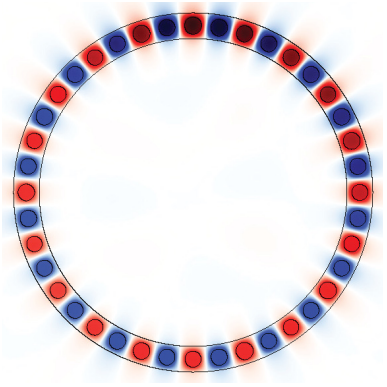

(C) H_z of the fundamental mode of the PhCRR with a **2.5% radius variation** of the low index material holes.

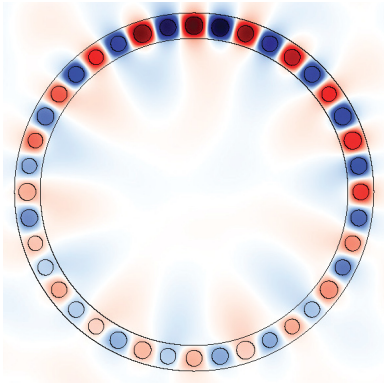

(D) H_z of the fundamental mode of the PhCRR with a **5% radius variation** of the low index material holes.

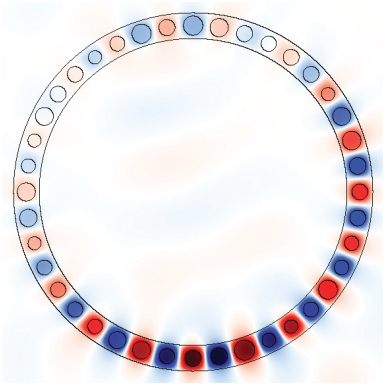

(E) H_z of the fundamental mode of the PhCRR with a **10% radius variation** of the low index material holes.

FIGURE 6.15: Anderson localization of the magnetic fields of the photonic crystal ring resonator due to geometric variation in the radius of the photonic crystal holes

Chapter 7

Fabrication design proposal for photonic crystal ring resonators

7.1 193 nm deep-UV lithography

Previous research efforts have demonstrated the successful fabrication of photonic crystal ring resonators on a silicon-on-insulator platform utilizing electron-beam lithography [33, 48]. Electron beam lithography provides high fabrication resolution, which allows for the precise manufacturing of sub-micron scale design features. However, electron-beam lithography offers a low throughput, making the fabrication process unsuitable for the mass-production of integrated photonic circuits. Alternatively, optical lithography technologies are compatible with existing electronics fabrication processes, allowing for straightforward upscaling of integrated photonic circuit manufacturing [53, 54]. In particular, 193 nm deep-UV lithography has been demonstrated to offer high fabrication resolutions comparable to those of the electron-beam lithography process [55, 56]. Accordingly, we have opted to employ 193 nm deep-UV lithography for the SOI fabrication of on-chip photonic crystal ring resonators. Utilizing deep-UV lithography will allow us to not only experimentally confirm the accuracy of our proposed design approach, but to probe the suitability of deep-UV lithography for potential mass-scale fabrication of PhCRRs.

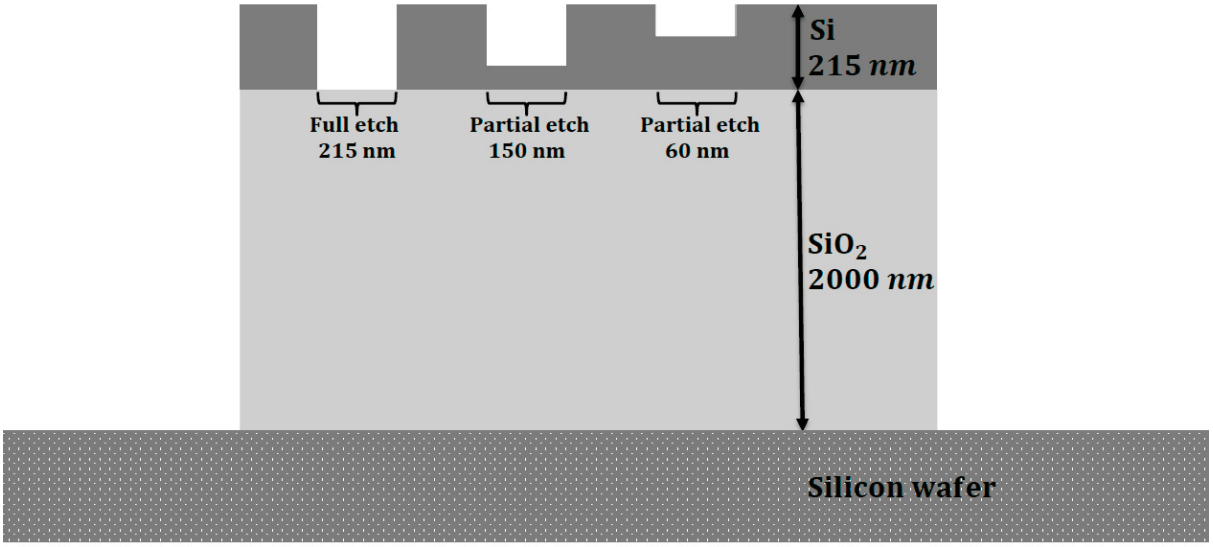

FIGURE 7.1: The silicon-on-insulator fabrication platform. Three etch options are allowed, including a full etch of 215 nm and two partial etches of 150 nm and 60 nm.

Design data has been submitted to the nano electronics research centre IMEC in Leuven, Belgium via the Canadian Microelectronics Corporation (CMC), with a device delivery date anticipated in late spring 2015. The IMEC facility utilizes a 200 mm silicon wafer with a 2000 nm buried-oxide layer of silicon dioxide. A 215 nm top layer of silicon offers three different etch levels: a full etch of 215 nm and two partial etches of 150 nm and 60 nm.

This allows for the fabrication of a wide variety of devices, including strip waveguides, rib waveguides, photonic crystal lattices, and fiber coupler gratings. Following etching of the silicon layer, three cladding options are available. An air cladding device has no side or top oxide, while a top oxide cladding device has a filling layer of silicon oxide in the etched regions and overlaying the silicon layer. Finally, a side oxide option has a filling layer of silicon oxide cladding in the etched regions with a top air cladding layer. In order to maximize the refractive index contrast between the ring resonator and the photonic crystal hole lattice of our PhCRR, we have chosen a full etch of the silicon layer with an air cladding.

When selecting design parameters for the on-chip implementation of a photonic crystal ring resonator, several fabrication restrictions of the 193 nm deep-UV lithography manufacturing process must be considered:

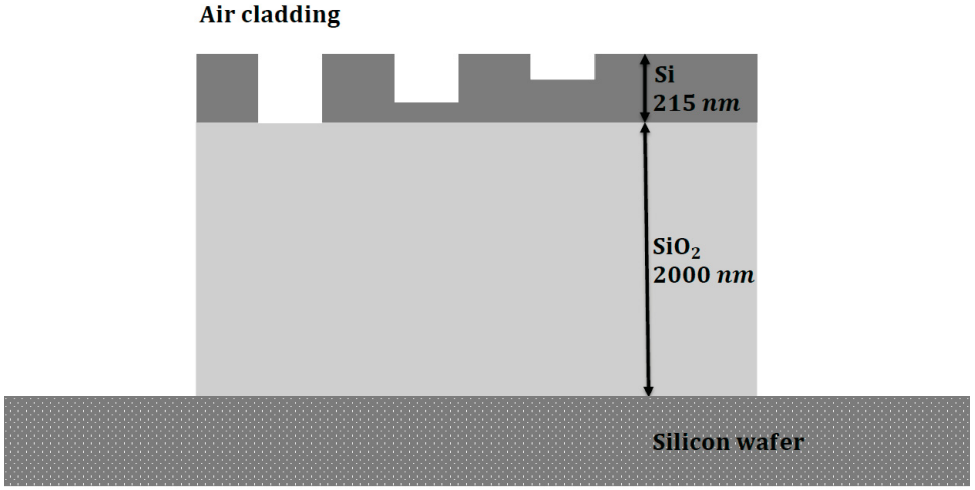

(A) An air cladding SOI device with no side or top oxide layers.

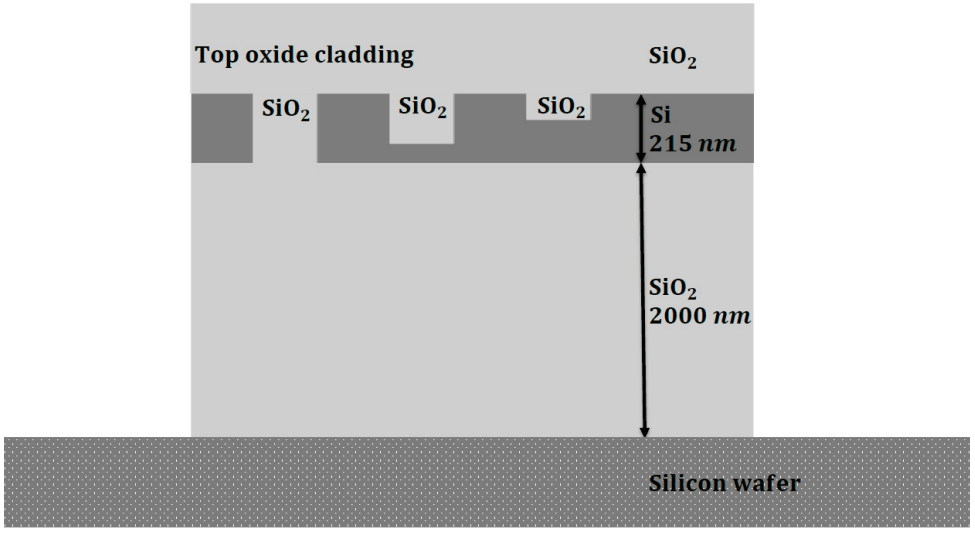

(B) A top cladding SOI device with a SiO_2 layer filling both the etched regions and overlaying the silicon material.

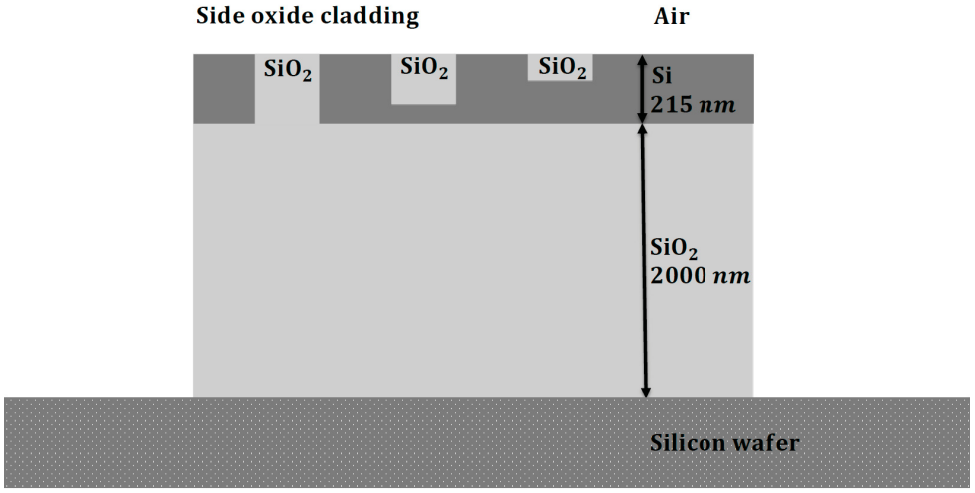

(C) A side cladding SOI device with a SiO_2 layer filling the etched regions and a top air cladding layer.

FIGURE 7.2: The three cladding options available on the SOI platform.

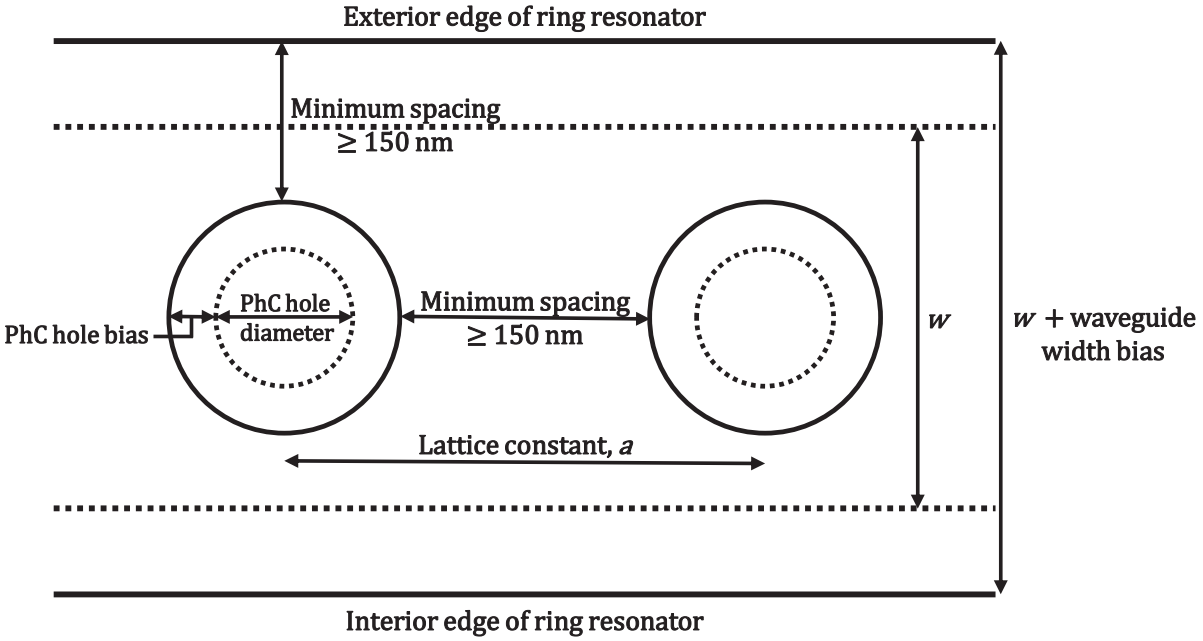

FIGURE 7.3: The minimum spacing requirements for a segment of a photonic crystal ring resonator fabricated on an SOI platform. The drawn dimensions of features are indicated in bold lines, while the actual, post-fabrication dimensions are indicated as dashed lines.

1. **Dimensional bias**:

   The deep-UV lithography fabrication process slightly alters the post-fabrication dimensions of devices. For example, a drawn photonic crystal lattice of lattice period $a = 350$ nm and hole radius of $r = 120$ nm will yield an actual photonic crystal lattice of approximately $a = 350$ nm and $r = 86$ nm, resulting in a nearly 29% change of the lattice's filling factor. Consequently, biases must be applied to the dimensions of features during the design process in order to preemptively account for these effects.

2. **Minimum width and spacing requirements**:

   Fabrication tolerances of deep-UV lithography limit the width and the minimum spacing between full etch features to 150 nm. To prevent violation of the minimum spacing design rule, a lattice period must be selected which allows for at least 150 nm between adjacent photonic crystal holes. The added limitation of accounting for positive biasing of the photonic crystal (PhC) holes further restricts the minimum lattice period allowed:

$$a = \text{PhC hole diameter} + (\text{PhC hole bias} \times 2) + 150\text{nm} \tag{7.1}$$

Additionally, the minimum spacing restriction of full etch features dictates the minimum allowable **width** of the photonic crystal ring resonator:

$$w + \text{waveguide width bias} = \text{PhC hole diameter} + (\text{PhC hole bias} \times 2) + (150\text{nm} \times 2) \quad (7.2)$$

Equation (7.2) highlights the fact that the minimum spacing requirements between full etch features must be considered *twice* to account for spacing between both the interior and exterior edges of the ring resonator and the photonic crystal hole. As opposed to the photonic crystal lattice, however, the actual dimensions of a full etch waveguide are often smaller than the drawn dimensions, which slightly alleviates the restrictions placed on the width of the high refractive index ring resonator.

7.2 Three-dimensional MPB and MEEP simulations

Recall from Chapter 5 that the first step in our design approach is to model the dispersion curve of a photonic crystal waveguide. The resultant band edge dimensionless frequency is then scaled to the desired resonant wavelength by adjusting the magnitude of the lattice period. In order to select highly accurate design parameters, three-dimensional simulations were conducted to improve the precision of the design approach. A photonic crystal waveguide of refractive index $n_{Si} = 3.518$ and thickness $t = 215$ nm with air holes of $n_{air} = 1.00$ was modelled using the MIT Photonic Bands software. The PhC waveguide was placed on a silicon dioxide substrate of thickness $t_{\text{sub}} = 2a$ and refractive index $n_{SiO_2} = 1.44$.

A Python design script was utilized which uses an iterative approach to scale the dimensionless frequency of a specified waveguide geometry to the resonant wavelength of choice. For the design under consideration, we targeted a width of $w = 1.25a$, a target band edge resonance of $\lambda = 1.550$ nm and a filling factor of $0.25a$. A large number of 3-D simulations were conducted in order to isolate design parameters which would respect the design restrictions imposed by Eqs. (7.1) and (7.2). As can be seen in Table 7.1, the lattice constant required to scale the dimensionless frequency of a photonic crystal waveguide to the desired resonant wavelength of $\lambda = 1550$ nm decreases with increasing waveguide width. Furthermore, for a constant waveguide width, the lattice constant decreases with decreasing filling factor. It thus proves difficult to

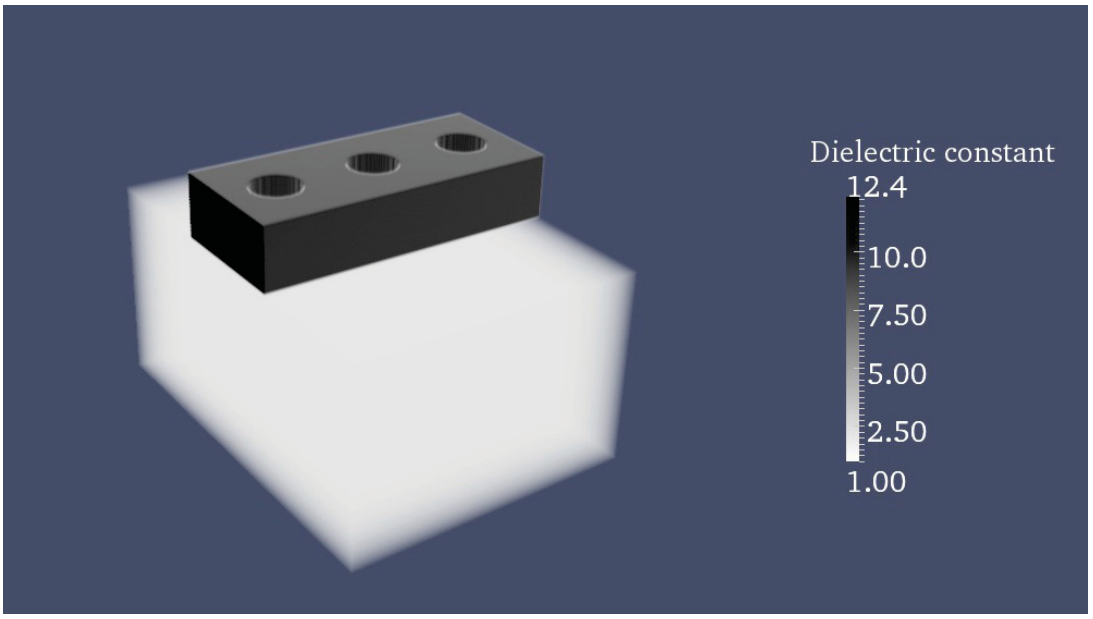

(A) The three-dimensional dielectric profile of three unit cells of the simulated photonic crystal waveguide on a silicon dioxide substrate. The scale bar indicates the strength of the dielectric constant, $\epsilon(\mathbf{r})$ of the materials. (Recall $n(\mathbf{r}) = \sqrt{\epsilon(\mathbf{r})}$).

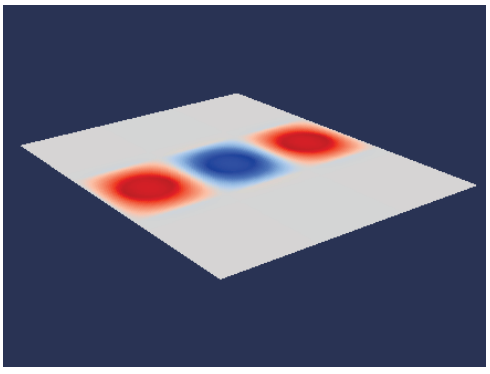

(B) A lateral slice of the H_z field profile for the first photonic band of the three-dimensional photonic crystal waveguide. The lateral slice is taken from the centre of the silicon photonic crystal waveguide (i.e. where $t_{Si} = 0.316a$ with respect to the silicon dioxide substrate).

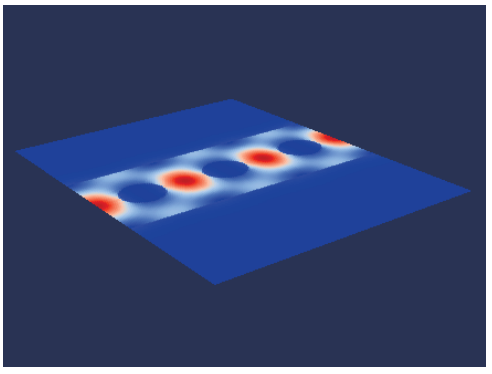

(C) A lateral slice of the electric field density for the first photonic band of the three-dimensional photonic crystal waveguide. The lateral slice is taken from the centre of the silicon photonic crystal waveguide (i.e. where $t_{Si} = 0.316a$ with respect to the silicon dioxide substrate).

FIGURE 7.4: Three-dimensional MEEP representations of the silicon photonic crystal waveguide's dielectric profile, magnetic field profile, and electric field density. The unit cell is composed of a silicon photonic crystal waveguide of lattice constant a, thickness $t_{Si} = 0.632227a$, width $w = 1.3a$, and hole radius $r = 0.242857a$. The photonic crystal waveguide is placed on a silicon dioxide buried-oxide layer of thickness $t_{BOX} = 2a$ with an air cladding. The refractive indices of the silicon and silicon dioxide are $n_{Si} = 3.518$ and $n_{SiO_2} = 1.4409$ respectively.

Waveguide width (a)	**Waveguide width (nm)**	**Lattice constant (nm)**	**Filling factor (a)**	**PC hole radius (nm)**
1.0	376	376	0.1	38
1.0	383	383	0.2	77
1.0	408	408	0.3	122
1.0	475	475	0.4	190
1.25	427	342	0.1	34
1.25	435	348	0.2	70
1.25	448	367	0.3	110
1.25	526	420	0.4	168
1.5	484	323	0.1	32
1.5	490	326	0.2	65
1.5	514	343	0.3	103
1.5	585	390	0.4	156

TABLE 7.1: Various design parameters for a photonic crystal ring resonator on an SOI platform with a photonic band edge resonance at $\lambda = 1550$ nm.

find a set of design parameters which will simultaneously satisfy the minimum spacing design restrictions. As the width of the waveguide increases, Eq. (7.2) is easily satisfied. However, the lattice constant must necessarily decrease in order to properly scale the dimensionless band edge frequency to 1550 nm, resulting in increasing violations of Eq. (7.1). In addition, increasing the width of the waveguide increases the risk of introducing higher-order modes into the waveguide.

The final design parameters selected for the on-chip testing of photonic crystal ring resonators are $a = 348$ nm, $w = 1.3a = 452$ nm, $ff = 0.242857$, and $r = 85$ nm. These parameters were selected due to the fact that they simultaneously minimized violation of the two spacing restrictions, yielding spacing values between adjacent PhC holes and the PhC hole and ring resonator edges of 141 nm and 178 nm, respectively. Taking into account the design biases required for the width of the waveguide and the radius of the photonic crystal holes, the drawn dimensions were adjusted to $w = 462$ nm and $r = 120$ nm.

As per our proposed design approach, Eq. (5.1) was applied to calculate the number of lattice periods required to construct the photonic crystal ring resonator. In order to investigate the limitations of miniaturization of the on-chip photonic crystal ring resonators, we have opted to design multiple PhCRRs of various different diameters. Due to the decreased radius of curvature, it is expected that reduction of the PhCRR's radius below 2.5 μm will lead to significant optical

losses. As a result, we have chosen to construct PhCRRs of diameters 5, 10, 20, 30 and 40 μm. The exact radius and number of lattice periods for each ring can be found in Table 7.2.

Diameter of Ring (μm)	**N**
5.096	46
9.970	90
20.162	182
30.132	272
40.102	362

TABLE 7.2: Exact diameter and number of lattice periods for the proposed on-chip photonic crystal ring resonators

To probe the spectral response of the designed photonic crystal ring resonator, three-dimensional time-domain simulations were conducted using the MIT Electromagnetics Equation Propagation software. Due to limited computational resources, only 3D simulations for the 5 μm PhCRR were carried out. To further reduce computational times, the simulations were run at low resolutions, with a simulation grid resolution of $\sim$50 nm. A broadband pulse of 1 μm was centered at 1550 nm and the excitation sources were once again placed in the centre of the first and second periodic elements. Once the sources had decayed to negligible values, the simulation was allowed to run for 1000 MEEP time units. The spectral response was then analyzed using both Fourier analysis and the Harminv harmonic inversion algorithm. As can be seen in Figure 7.5b, the photonic band edge resonance was found at $\lambda = 1548$ nm.

7.3 Proposed scheme for on-chip testing

The final design proposal for the SOI on-chip testing of photonic crystal ring resonators can be seen in Figure 7.6. The red regions represent a silicon ring resonator composed of a ridge waveguide with a full etch of the surrounding silicon material. The photonic crystal holes are seen as pink circles; the interior of the circles designate full etch regions of the silicon ring resonator. Each photonic crystal ring resonator is placed on a "no fill" region, seen here in blue. In general, unused regions of the silicon wafer are filled with dummy structures which allow for density control of the microchip's features. However, reflections off of the dummy structures may adversely affect the performance of the device. Consequently, placing "no fill" regions

(A) The three-dimensional dielectric profile of the 5.096 μm diameter PhCRR. The strength of the dielectric constant, $\epsilon(\mathbf{r})$, is equivalent to that of Figure 7.4a. The PhCRR is composed of a silicon layer of thickness 215 nm with a lattice period of 348 nm, a width of 452 nm, and photonic crystal air holes of radius 85 nm. The PhCRR is placed on a silicon dioxide substrate of thickness 696 nm.[a]

[a]While in practice, the thickness of the silicon dioxide substrate is equal to 2000 nm, a BOX substrate thickness of ~ 2 lattice periods is sufficient for simulations.

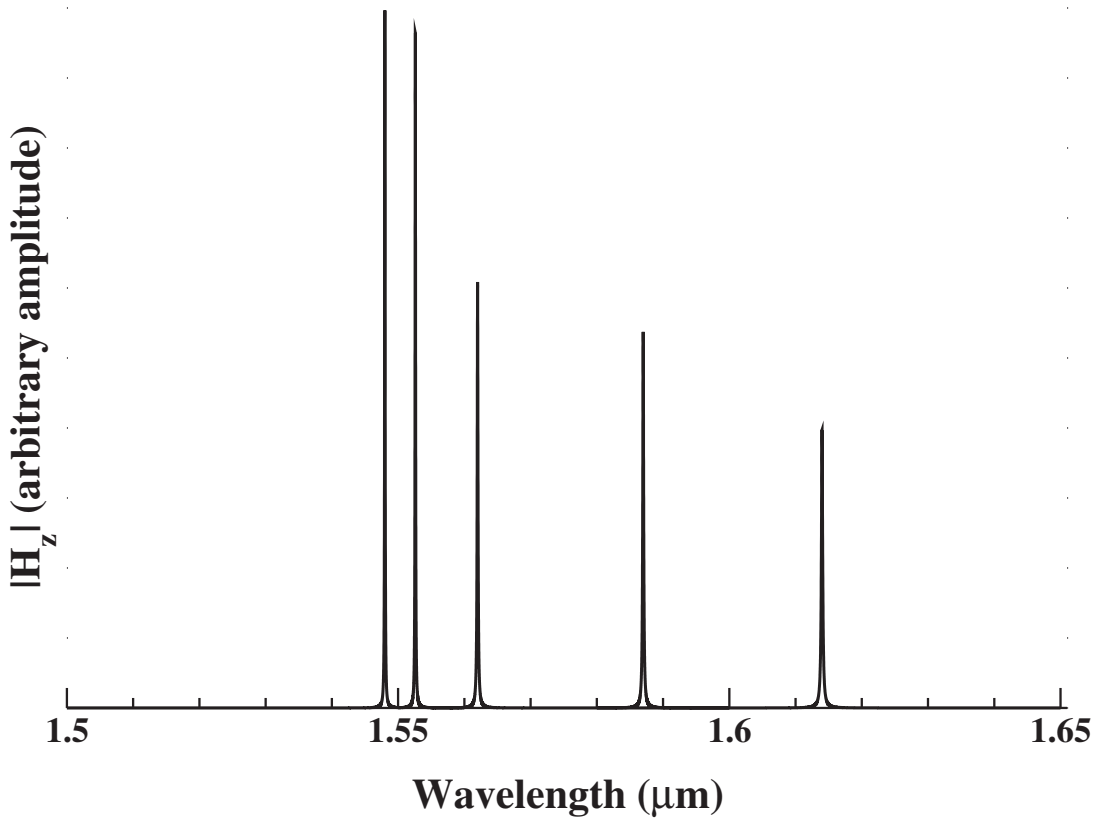

(B) The spectral response of the 5.096 μm diameter PhCRR computed via the harmonic inversion algorithm program, Harminv.

FIGURE 7.5: The dielectric profile and spectral response resulting from the three-dimensional MEEP simulation of a 5.096 μm diameter photonic crystal ring resonator.

around the active regions of the microchip can minimize the risk of unfavourable interactions between the device and dummy structures. Yellow labels are placed near each PhCRR in order to facilitate the identification of each resonator during testing.

7.3.1 Fiber grating couplers

Our design allows for two separate on-chip testing schemes. Firstly, photonic crystal ring resonators are placed in close proximity to a curved silicon waveguide of width 450 nm. The photonic crystal ring resonator can couple to the waveguide's guided modes via interaction between the waveguide's evanescent fields and the mode profiles of the PhCRR[1]. In principle, light can be inserted into the microchip via use of a single-mode optical fiber (SMF). However, coupling light directly into a silicon waveguide proves difficult due to the large mismatch between the SMF mode and the waveguide mode, resulting in high optical losses. One solution to this problem is use of a **grating fiber coupler** [57]. A grating fiber coupler utilizes a Bragg grating to vertically couple to out-of-plane SMF modes. In order to minimize unfavourable second-order reflections that occur between the SMF and the grating coupler when the fiber is oriented perpendicular to the Bragg grating, the fiber is oriented at a slight angle from the normal plane of the Bragg grating. Once light is coupled into the grating coupler, an adiabatically tapered waveguide is utilized to convert the inserted mode into a silicon waveguide mode with minimal optical losses.

We have made use of this technology by placing an input and output grating fiber coupler at either end of the curved waveguide. The fiber grating coupler utilized in our silicon microchip design is distributed with the IMEC SOI design kit and is optimized for the coupling of transverse-electric modes at 1550 nm. The grating coupler has a 30 nm bandwidth and a 10 degree insertion angle with respect to the surface normal direction of the microchip. The spectral fingerprint of each photonic crystal ring resonator will be determined by comparing the spectral profiles of the input and output channels; for each resonance of the PhCRR, we can expect a drop in transmission at the output grating coupler.

To facilitate ease of on-chip testing of the photonic crystal ring resonators, the fiber grating couplers have been equidistantly spaced a distance of 127 μm apart. The input and output

[1] See Appendix A for more information detailing coupling of waveguides and PhCRR's via evanescent fields.

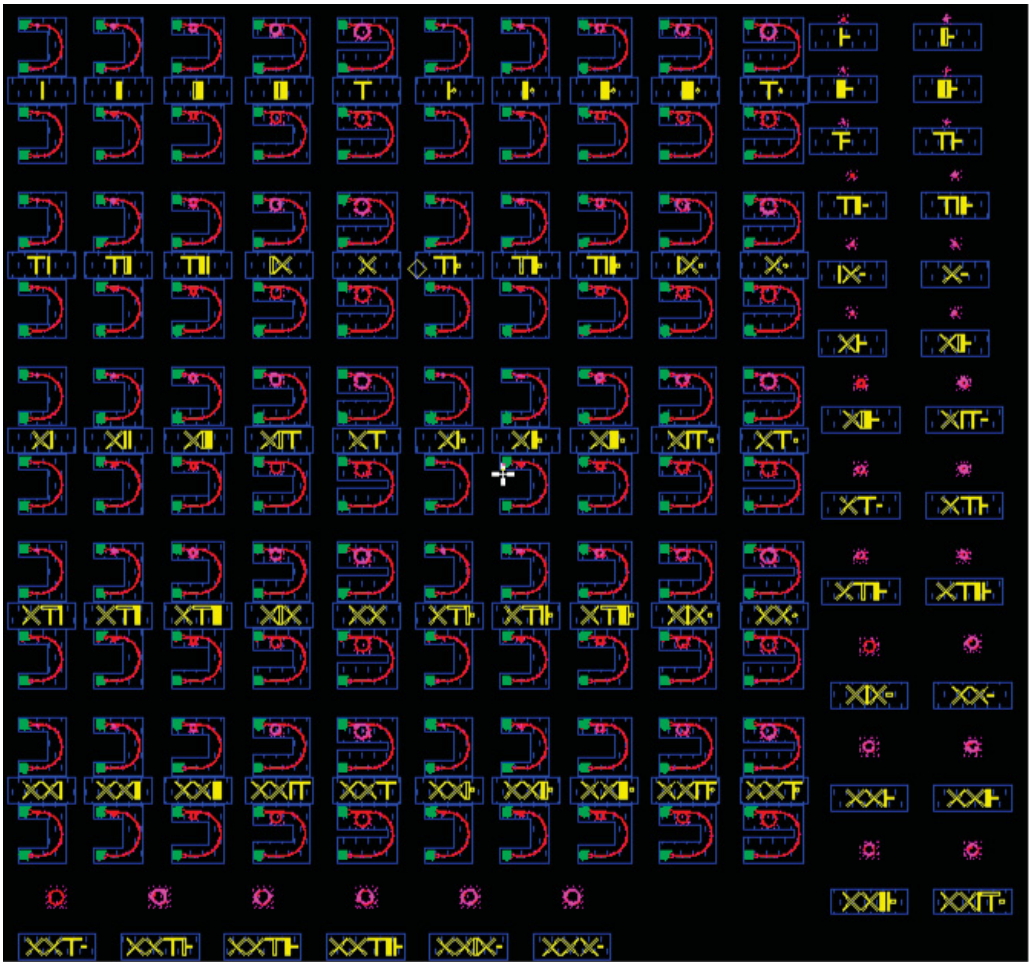

(A) Final design proposal for the SOI on-chip testing of photonic crystal ring resonators

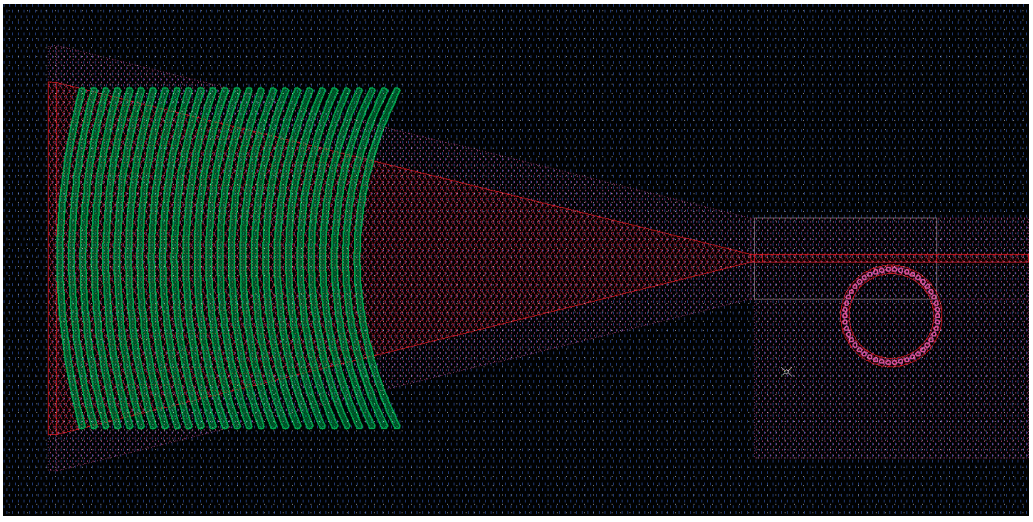

(B) A photonic crystal ring resonator of diameter $d = 5$ μm with a 450 nm wide silicon coupling waveguide and input fiber grating coupler port.

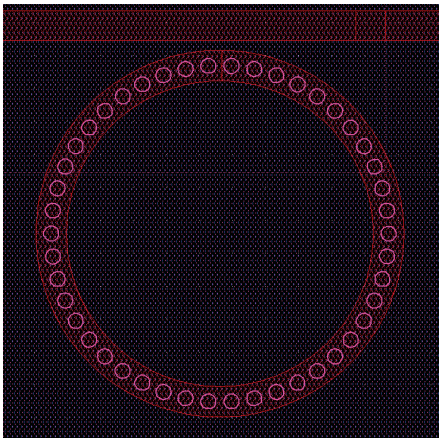

(C) A close-up of a photonic crystal ring resonator of diameter $d = 5$ μm and a 450 nm wide silicon coupling waveguide.

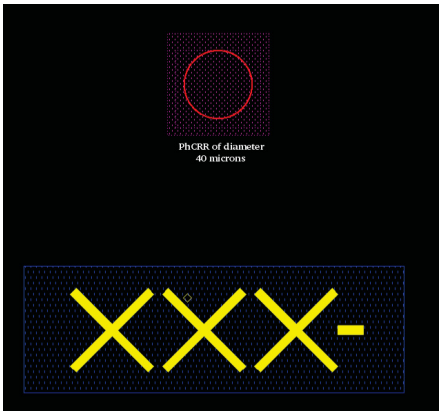

(D) A standalone photonic crystal ring resonator of diameter $d = 40$ μm photonic crystal ring resonator for on-chip testing via tapered optical fibers.

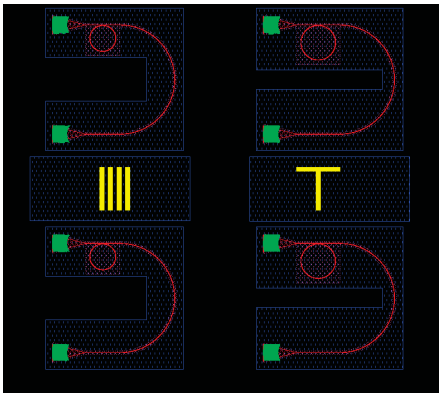

(E) Photonic crystal ring resonators of diameters $d = 30$ and 40 μm and their equivalent ring resonators. The PhCRRs and RRs are placed in close proximity to the coupling waveguides for on-chip testing via fiber grating couplers. The input and output grating couplers are placed 127 μm apart for use with a fiber array.

FIGURE 7.6: Submitted design data for the SOI fabrication of photonic crystal ring resonators via 193 nm deep-UV lithography.

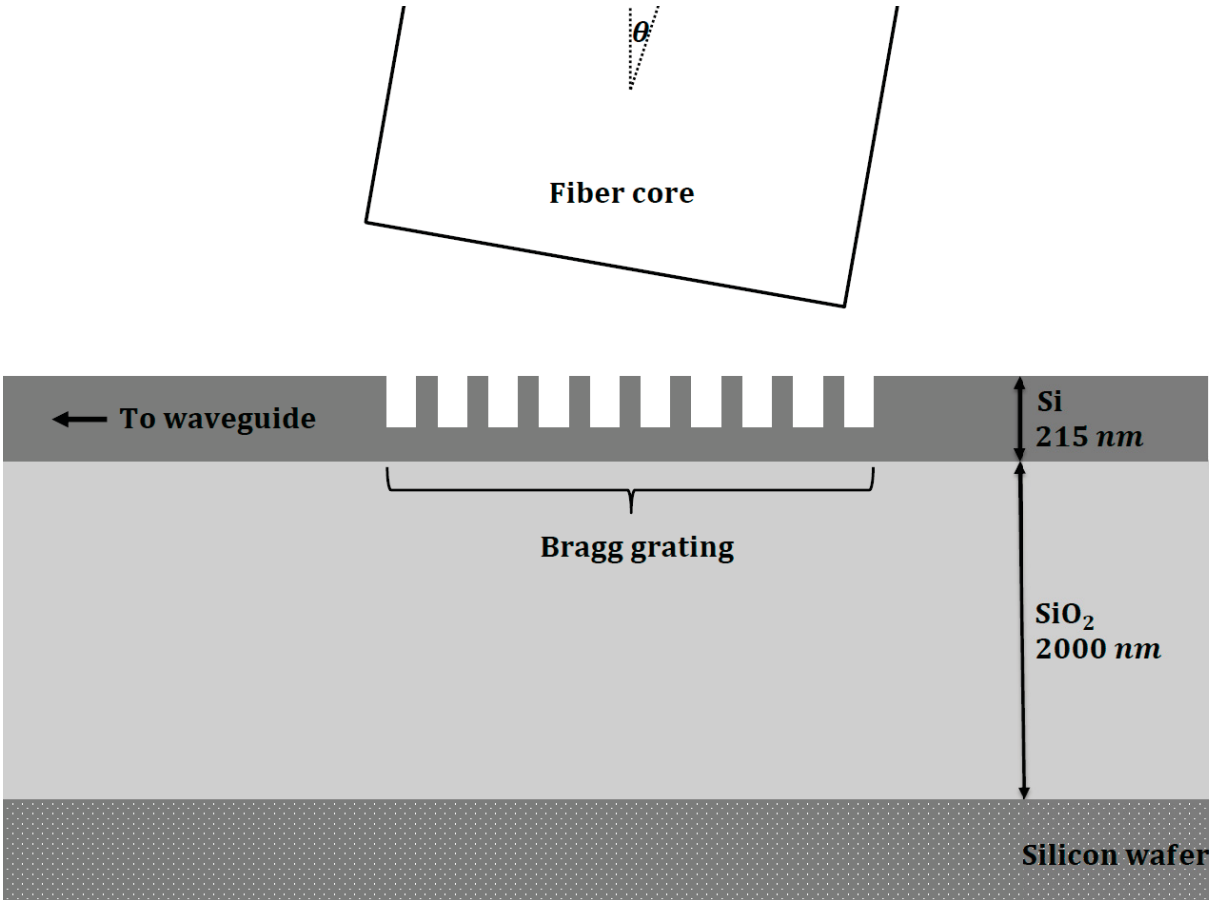

FIGURE 7.7: A fiber grating coupler consisting of a partially etched Bragg grating in a silicon waveguide. The optical fiber is coupled to the Bragg grating and placed slightly off axis with respect to the normal plane of the Bragg grating in order to prevent second-order reflections. The inserted mode is converted via an adiabatic taper of the silicon waveguide.

grating coupler channels can now be measured via use of a **fiber array**. A fiber array positions an ensemble of parallel optical fibers with a periodicity equal to the spacing of the on-chip grating couplers. It thus allows for the precise, sub-micron positioning of multiple optical fibers with respect to the input and output channels of the silicon waveguides. To experimentally confirm the slow light enhancement of quality factors, standard ring resonators of 5, 10, 20, 30 and 40 μm have been added to the microchip for comparative purposes.

7.3.2 Tapered optical fibers

Our second testing scheme makes use of **tapered optical fibers**. A tapered optical fiber is fabricated by gradually heating and stretching a standard optical fiber. The stretching process

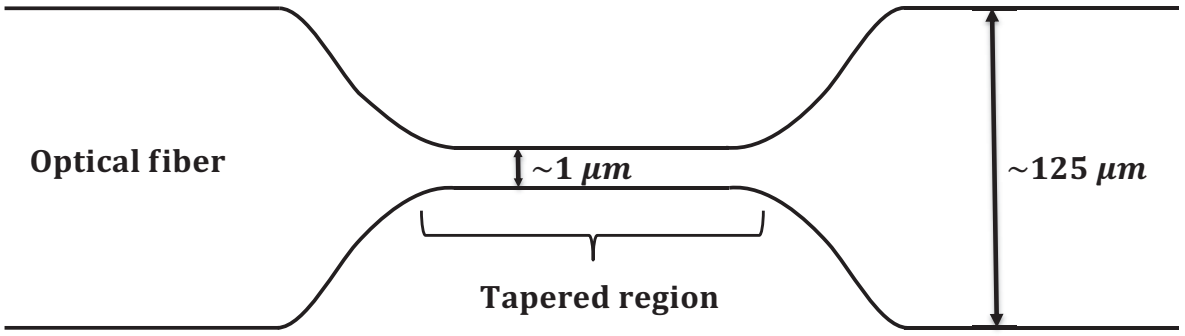

FIGURE 7.8: A tapered optical fiber. The diameter of the fiber is adiabatically tapered from ~ 125 μm to ~ 1 μm, reducing the mode mismatch between the optical fiber and the photonic crystal ring resonator. The evanescent field of the tapered region is utilized to transfer high optical power to the PhCRR.

is designed so as to adiabatically taper the diameter of a standard optical fiber from ~ 125 μm to a few microns in diameter [58]. The small dimensions of the tapered fiber's waist results in increased mode matching between the optical fiber and a silicon photonic crystal ring resonator, allowing for direct coupling. The tapered optical fiber produces a strong evanescent field that, when brought into close proximity with the PhCRR, can overlap with the field profiles of the resonator's modes. The greater the overlap between the mode profiles, the stronger the coupling between the tapered fiber and the resonator. Tapered fibers offer one main advantage over use of grating couplers: the mode match between the evanescent field of a tapered fiber and that of a silicon waveguide allows for highly efficient optical coupling between the fiber and waveguide [59]. Increasing power transfer to the photonic crystal ring resonator opens up the possibility for the observation of non-linear effects [60]. To allow for the testing of on-chip photonic crystal ring resonators via tapered optical fibers, multiple stand-alone PhCRRs and their equivalent ring resonators have been placed on the microchip.

Local variations of up to ± 10 nm may occur in the thickness of the silicon layer during the deposition fabrication process. Such a variance will result in a change in the effective refractive indices of the silicon ring resonator and photonic crystal lattice of air holes., causing a shift in the resonances of the designed PhCRRs. In order to account for these shifts, we have placed multiple occurrences of each photonic crystal ring resonator on the microchip to increase the likelihood of detecting a photonic band edge resonant mode at $\lambda = 1550$ nm. This will also

allow us to probe the suitability of 193 nm deep-UV lithography for the mass-scale fabrication of photonic crystal ring resonators by establishing the reproducibility of identical devices.

Chapter 8

Conclusions and outlook

There are currently several areas of research regarding the spectral features of photonic crystal ring resonators that require further investigation, including:

1. **Exploration of PhCRR group symmetries:** In our simulations, splitting of the degenerate quadrupole mode was more pronounced than for any other mode of the photonic crystal ring resonator. Further examination of the PhCRR's spectral response is needed to account for our observations. It is suspected that the group symmetries of the photonic crystal ring resonator's dielectric structure may be the underlying cause of these effects. Simulations of photonic crystal ring resonators possessing alternative group symmetries will allow for further analysis of this hypothesis.

2. **Engineered zero-dispersion photonic crystal ring resonators:** An investigation of the group symmetries of the photonic crystal ring resonator may also shed light on how precisely these symmetries can be utilized to engineer anti-crossing regions of the photonic dispersion relation via mode coupling. Such an anti-crossing region would possess a "flat-band" region of the device's group index, signifying a negligible group velocity dispersion parameter. An alternative approach to engineering zero-dispersion devices is via coupling of two or more photonic crystal ring resonators. Recall that the group velocity dispersion parameter is defined as $D_\lambda = -\frac{2\pi c}{\lambda^2}\frac{d^2k}{d\omega^2}$. As a result, clockwise and counterclockwise propagating resonant modes of a PhCRR possess group velocity dispersion parameters which

are equal, but opposite, in magnitude (refer to Figure 5.4). If the clockwise and counterclockwise propagating modes can be independently excited in two separate PhCRRs, coupling of the devices could nullify the distortion of a propagating optical pulse.

3. **Alternative fabrication platforms and devices**. To increase the versatility of the proposed design approach, it is fitting to explore alternative fabrication platforms and materials which might be utilized to manufacture slow light resonators. In particular, the epitaxial growth of nanopillars could potentially be used to generate a ring of nanopillars possessing comparable spectral features as those of a PhCRR. To further generalize, the proposed design approach might be applied to any nanostructure possessing a periodic dielectric function and ring-like structure, given that the absorption coefficients of the constituent materials can reasonably be neglected.

In closing, this thesis has presented a theoretical analysis of the photonic crystal ring resonator. We have analyzed the unique spectral features of the PhCRR, including the non-uniform spacing of adjacent modes and the frequency cutoff of resonances due to the bounded nature of the photonic dispersion relation. Additionally, disorder-induced phenomena, such as mode splitting and Anderson localization of electric fields, were explored.

A design approach was proposed that allows for the selective positioning of the PhCRR's resonant modes of a chosen wavelength along any region of the photonic dispersion relation that is of interest. In particular, slow light resonant modes were targeted by placing resonances directly at the photonic band edge of the photonic dispersion relation. Computational methods were employed to demonstrate the slow light enhancement of the resonances' quality factors. The field configurations of the resonant modes were examined and an analysis of the spatial beating found in higher-order modes was presented.

Simulations demonstrated that band-edge modes possessing high second- and third-order dispersion parameters are highly susceptible to optical losses stemming from fabrication induced surface roughness and geometric variations in the photonic crystal lattice. To combat the unfavourable optical losses found in slow light resonances at the photonic band edge, several possible solutions were discussed. It was demonstrated that the design approach could be modified to place the resonances of the PhCRR slightly away from the photonic band edge, where

surface induced optical losses are reduced. In addition, fabrication of "anti-crossing" regions of the dispersion relation which possess low group velocity dispersion parameters were discussed.

Finally, a design proposal for the SOI fabrication of photonic crystal ring resonators was outlined. The design will allow for the experimental confirmation of the validity of the proposed design approach and will furthermore supply valuable information concerning the suitability of 193 nm deep-UV lithography for the fabrication of photonic crystal ring resonators.

Appendix A

Total Internal Reflection: Evanescent electromagnetic fields

In Section 2.1, we discussed the phenomenon of total internal reflection and how the energy of an electromagnetic wave is completely reflected at a dielectric interface when the propagating wave and dielectric materials in question satisfy certain conditions. Notwithstanding the total confinement of the wave's energy to the high refractive index material, a portion of the electromagnetic field is allowed to penetrate the dielectric interface and propagate into the lower refractive index material [14].

In Figure A.1, we consider a plane wave of the form $e^{i(\mathbf{k}\cdot\mathbf{r})}$ propagating through the high refractive index material, n_1. Upon traversal of the dielectric interface, the change in refractive index of the material seen by the propagating wave necessarily causes a change in the photon's wave vector, which we denote as $\mathbf{k}'$. The transmitted wave can thus be described by the equation:

$$e^{i(\mathbf{k}'\cdot\mathbf{r})} = e^{i(k'_x x + k'_y y)} \tag{A.1}$$

Alternatively, the reflected wave does not experience a change in refractive index. As a result the wave vector of the incident wave is equivalent to that of the reflected wave, implying:

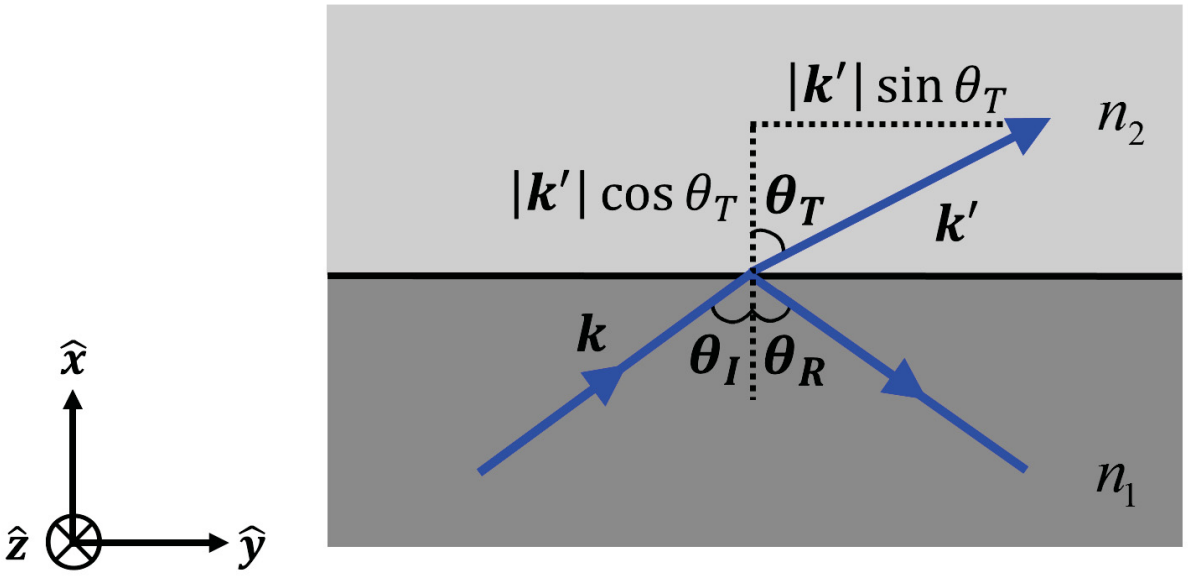

FIGURE A.1: The $\hat{x}$ and $\hat{y}$ components of the transmitted wave vector, $\mathbf{k}'$

$$\theta_I = \theta_R \tag{A.2}$$

Using Snell's Law (Eq. (2.1)) and equating the reflected and incident angles, the ratio of the refractive indices of the two materials forming the dielectric interface can be expressed as a ratio of the sines of the incident and transmitted angles:

$$\frac{\sin(\theta_I)}{\sin(\theta_T)} = \frac{n_2}{n_1} \tag{A.3}$$

Recall that for total internal reflection to occur, we must require that $n_1 > n_2$. We now consider the case when the incident angle, θ_I is greater than or equal to the critical angle, defined as $\theta_C = \sin^{-1}(\frac{n_2}{n_1})$. In such a case, Eq. (A.3) can be rewritten as:

$$\begin{aligned} \frac{\sin(\theta_I)}{\sin(\theta_T)} &\geq \frac{\sin[\sin^{-1}(\frac{n_2}{n_1})]}{\sin(\theta_T)} \\ \frac{n_2}{n_1} &\geq \frac{n_2}{n_1} \cdot \frac{1}{\sin(\theta_T)} \\ \Rightarrow \sin(\theta_T) &\geq 1 \end{aligned} \tag{A.4}$$

We see immediately that the sine of the transmitted angle must be greater than 1. This implies that the transmitted angle is a complex value, consisting of both a real and imaginary part.

In order to fully describe the behaviour of the transmitted wave, we must determine the components k'_x and k'_y. In terms of the complex transmitted angle, θ_T, the $\hat{x}$ and $\hat{y}$-components of the transmitted wave vector can be expressed as:

$$k'_x = |\mathbf{k}'| \cos(\theta_T) \tag{A.5a}$$

$$k'_y = |\mathbf{k}'| \sin(\theta_T) \tag{A.5b}$$

The component k'_y is easily described in terms of the incident and critical angle of the electromagnetic wave. We first insert Snell's law into Eq. (A.5b), yielding:

$$k'_y = |\mathbf{k}'| \cdot \frac{n_1}{n_2} \sin(\theta_I) \tag{A.6}$$

We can then use the definition of the critical angle to express the $\hat{y}$-component of $\mathbf{k}$' as:

$$k'_y = |\mathbf{k}'| \cdot \frac{\sin(\theta_I)}{\sin(\theta_C)} \tag{A.7}$$

To find the $\hat{x}$-component of $\mathbf{k}$', we must apply the trigonometric relationship $\cos^2(\theta) = 1 - \sin^2(\theta)$ to Eq. (A.5a). Recall that for $n_1 > n_2$, the sine of θ_T must be greater than 1, implying that $\cos(\theta_T)$ must be imaginary. As a result, we find:

$$\begin{aligned} \cos^2(\theta_T) &= 1 - \sin^2(\theta_T) = i^2(\sin^2(\theta_T) - 1) \\ &= i^2\left[\left(\frac{\sin(\theta_I)}{\sin(\theta_C)}\right)^2 - 1\right] \\ \Rightarrow \cos(\theta_T) &= i\sqrt{\left(\frac{\sin(\theta_I)}{\sin(\theta_C)}\right)^2 - 1} \end{aligned} \tag{A.8}$$

Inserting Eqs. (A.8) and (A.7) into Eq. (A.1), we find an expression describing the propagation of the transmitted wave in the low refractive index material.

$$e^{i(\mathbf{k}'\cdot\mathbf{r})} = e^{i|\mathbf{k}'|[\sin(\theta_I)/\sin(\theta_C)]y} e^{-|\mathbf{k}'|[(\sin(\theta_I)/\sin(\theta_C))^2-1]^{1/2}x} \tag{A.9}$$

This equation describes a plane wave propagating parallel to the plane of the dielectric boundary that is modified by a decaying exponential function. The decay will cause the transmitted wave to attenuate to negligible values within a few wavelengths of distance perpendicular from the dielectric interface. This field is known as an **evanescent wave** and is crucial in our understanding of waveguide coupling. As discussed in Section 7.3, our fabricated photonic crystal ring resonator device will utilize a fiber grating coupler to inject light into the PhCRR. In order for light to couple from the grating coupler waveguide into the resonator, the evanescent field of the waveguide must be placed in close enough proximity to the ring resonator so that the mode profiles of the waveguide's evanescent field might overlap with the mode profiles of the PhCRR's resonances. An overlap of the mode profiles will allow electromagnetic waves to pass from the waveguide into the resonator.

Figure A.2b shows how the transmitted power from the waveguide to the resonator increases with a decreasing evanescent gap (indicated here as the parameter g). While ultimately the coupling between waveguide and resonator increases for an evanescent gap < 150nm, the resolution of the deep-UV lithography fabrication process limits us to a minimum value of $g = 150$nm.

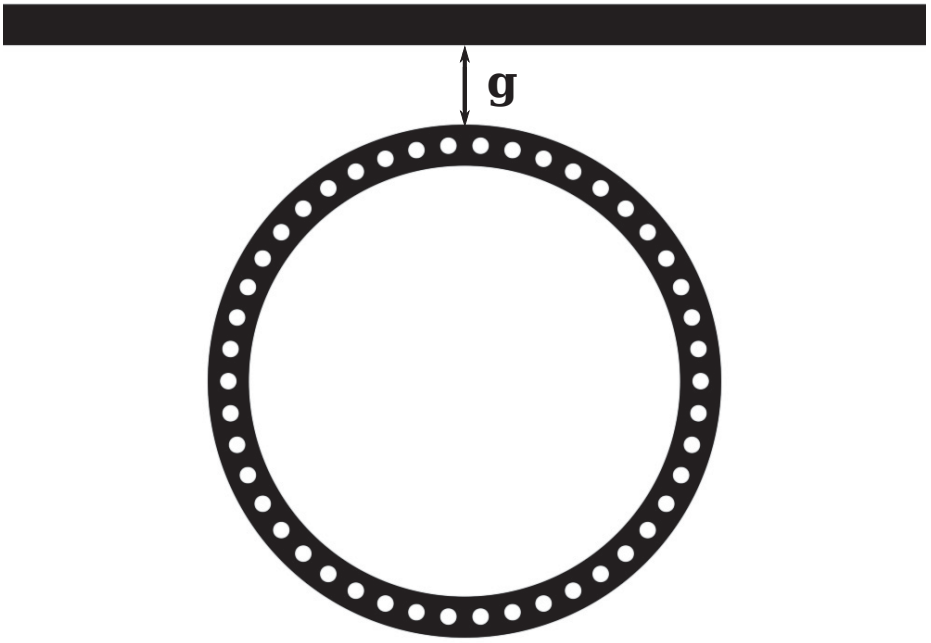

(A) A photonic crystal ring resonator and a coupling waveguide. The high and low refractive index materials are indicated in black and white, respectively. The evanescent gap between the coupling waveguide and the PhCRR is indicated by the parameter g.

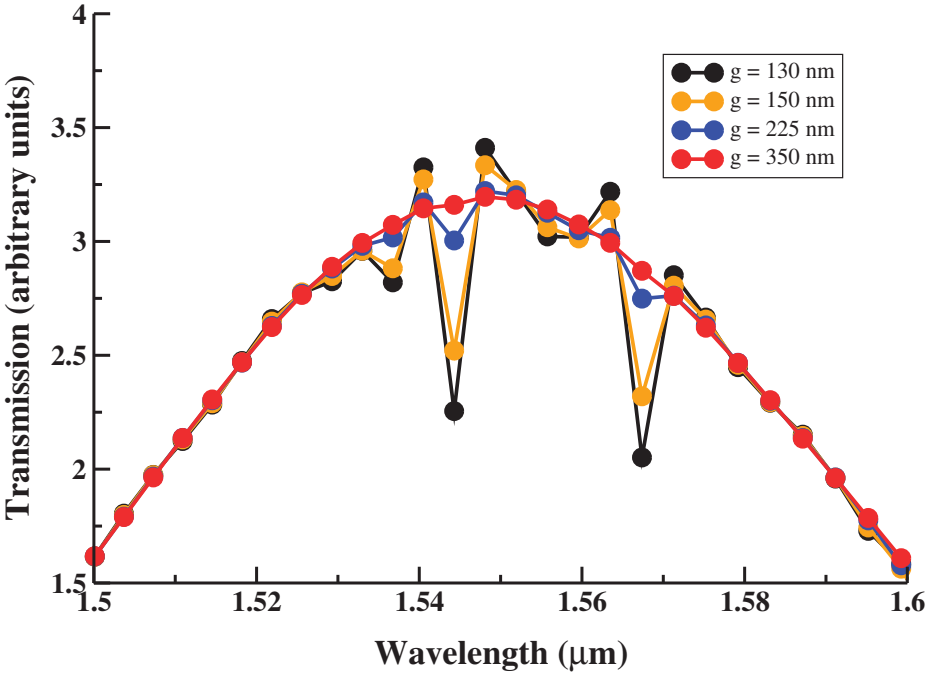

(B) The transmission spectrum of the coupling waveguide. Dips in transmission can be seen where the waveguide mode is coupled into the photonic crystal ring resonator (indicating a resonance of the PhCRR). The strength of the coupling increases with a decreasing evanescent gap.

FIGURE A.2: The dielectric profile and transmission spectra resulting from a 2-D MEEP simulation of a photonic crystal ring resonator and an accompanying coupling waveguide

Appendix B

Derivation of the propagation constant

To derive an expression for β, we first consider the electromagnetic wave described in Section2.3.1:

$$E_z(x,t) = E_z e^{-i(k_x x - \omega t)} \tag{B.1}$$

The behaviour of the wave can be described by the one-dimensional **wave equation**:

$$\frac{\partial^2 u(x,t)}{\partial x^2} = \frac{1}{v_x^2}\frac{\partial^2 u(x,t)}{\partial t^2} \tag{B.2}$$

When applying the wave equation to the electromagnetic wave under consideration, we see u describes the $\hat{z}$-component of the electromagnetic wave, E_z, while v denotes the velocity of the wave propagating in the $\hat{x}$-direction. The velocity of an electromagnetic wave can be defined as [20]:

$$v = \frac{1}{\sqrt{\epsilon_r \epsilon_0 \mu_r \mu_0}} \tag{B.3}$$

where ϵ_r and μ_r are the relative permittivity and permeability of the material and ϵ_0 and μ_0 are the vacuum permittivity and permeability, respectively. Plugging Eq. (B.1) into Eq. (B.2) yields:

$$\begin{aligned} \frac{\partial^2 E_z(x,t)}{\partial x^2} &= \left(\frac{1}{\sqrt{\epsilon_r \epsilon_0 \mu_r \mu_0}} \right)^2 \frac{\partial^2 E_z(x,t)}{\partial t^2} \\ \Rightarrow k_x^2 &= \frac{1}{\epsilon_r \epsilon_0 \mu_r \mu_0} \omega^2 \end{aligned} \tag{B.4}$$

Recall from Section 2.3.1 that the wave vector, k_x, can be expressed in terms of a real and imaginary part, $k = \beta - i\frac{\alpha}{2}$. As we have assumed that the absorption properties of the materials in question are negligible, we set α equal to zero. If we then apply the relations $\omega = \frac{2\pi c}{\lambda}$, $c = \frac{1}{\sqrt{\epsilon_0 \mu_0}}$, and $n = \sqrt{\epsilon_r \mu_r}$ to Eq. (B.4), we find:

$$\begin{aligned} k_x^2 = \beta^2 &= (\epsilon_r \epsilon_0 \mu_r \mu_0) \left(\frac{2\pi c}{\lambda} \right)^2 \\ &= (\epsilon_r \epsilon_0 \mu_r \mu_0) \left(\frac{2\pi \frac{1}{\sqrt{\epsilon_0 \mu_0}}}{\lambda} \right)^2 \\ &= (\epsilon_r \mu_r) \left(\frac{2\pi}{\lambda} \right)^2 \\ \Rightarrow \beta &= \frac{2\pi n}{\lambda} \end{aligned} \tag{B.5}$$

Bibliography

[1] D. J. Lockwood and L. Pavesi, "Silicon fundamentals for photonics applications," in *Silicon Photonics*, D. J. Lockwood and L. Pavesi, eds. (Springer-Verlag, 2004).

[2] M. Paniccia, M. Morse, and M. Salib, "Integrated photonics," in *Silicon Photonics*, D. J. Lockwood and L. Pavesi, eds. (Springer-Verlag, 2004).

[3] A. V. Kavokin, J. J. Baumberg, G. Malpuech, and F. P. Laussy, *Microcavities* (Oxford University Press, 2007).

[4] P. Nouchi, P. Sillard, and D. Molin, "Optical fibers," in *Fiber Optic Communication: Key Devices*, H. Venghaus and N. Grote, eds. (Springer-Verlag, 2012).

[5] J. Vučković, M. Lončar, H. Mabuchi, and A. Scherer, "Design of photonic crystal microcavities for cavity qed," Phys. Rev. E **65**, 016608 (2001).

[6] R. J. Coles, N. Prtljaga, B. Royall, I. J. Luxmoore, A. M. Fox, and M. S. Skolnick, "Waveguide-coupled photonic crystal cavity for quantum dot spin readout," Opt. Express **22**, 2376–2385 (2014).

[7] M. Ferrera, D. Duchesne, L. Razzari, M. Peccianti, R. Morandotti, P. Cheben, S. Janz, D.-X. Xu, B. E. Little, S. Chu, and D. J. Moss, "Low power four wave mixing in an integrated, micro-ring resonator with q = 1.2 million," Opt. Express **17**, 14098–14103 (2009).

[8] Y. Liu, Y. Xuan, X. Xue, P.-H. Wang, S. Chen, A. J. Metcalf, J. Wang, D. E. Leaird, M. Qi, and A. M. Weiner, "Investigation of mode coupling in normal-dispersion silicon nitride microresonators for kerr frequency comb generation," Optica **1**, 137–144 (2014).

[9] B. Little, S. Chu, H. Haus, J. Foresi, and J.-P. Laine, "Microring resonator channel dropping filters," Journal of Lightwave Technology **15**, 998 (1997).

[10] K. J. Vahala, "Optical microcavities," Nature **424**, 839–846 (2003).

[11] X. Fan, I. M. White, S. I. Shopova, H. Zhu, J. D. Suter, and Y. Sun, "Sensitive optical biosensors for unlabeled targets: A review," Analytica Chimica Acta **620**, 8 – 26 (2008).

[12] M. S. McClellan, L. L. Domier, and R. C. Bailey, "Label-free virus detection using silicon photonic microring resonators," Biosensors & bioelectronics **31**, 388–392 (2012).

[13] T. Baba, "Slow light in photonic crystals," Nat Photon **2**, 465–473 (2008).

[14] J. D. Jackson, *Classical Electrodynamics* (John Wiley and Sons, Inc., 1998), 3rd ed.

[15] K. J. Ebeling, *Integrated Optoelectronics* (Springer-Verlag, 1992).

[16] K. Yamada, "Silicon photonic wire waveguides: Fundamentals and applications," in *Silicon Photonics II: Components and Integrations*, D. J. Lockwood and L. Pavesi, eds. (Springer-Verlag, 2011).

[17] D. Rabus, *Integrated Ring Resonators: The Compendium* (Springer-Verlag, 2007).

[18] F. Morichetti, A. Canciamilla, M. Martinelli, A. Samarelli, R. M. De La Rue, M. Sorel, and A. Melloni, "Coherent backscattering in optical microring resonators," Applied Physics Letters **96**, 081112 (2010).

[19] N. W. Ashcroft and N. D. Mermin, *Solid State Physics* (Harcourt Brace College Publishers, 1976).

[20] D. J. Griffiths, *Introduction to Electrodynamics* (Prentice-Hall Inc., 1999), 3rd ed.

[21] J. D. Joannopoulos, S. G. Johnson, J. N. Winn, and R. D. Meade, *Photonic Crystals: Molding the Flow of Light* (Princeton University, 2008), 2nd ed.

[22] D. J. Griffiths, *Introduction to Quantum Mechanics* (Pearson Education, 2005), 2nd ed.

[23] M. L. Boas, *Mathematical Methods in the Physical Sciences* (John Wiley and Sons, 2006), 3rd ed.

[24] I. G. Main, *Vibrations and Waves in Physics* (Cambridge University Press, 1993), 3rd ed.

[25] T. F. Krauss, "Slow light in photonic crystal waveguides," Journal of Physics D: Applied Physics **40**, 2666 (2007).

[26] J. Gao, S. Combrie, B. Liang, P. Schmitteckert, G. Lehoucq, S. Xavier, X. Xu, K. Busch, D. L. Huffaker, A. De Rossi, and C. W. Wong, "Strongly coupled slow-light polaritons in one-dimensional disordered localized states," Sci. Rep. **3** (2013).

[27] M. D. Settle, R. J. P. Engelen, M. Salib, A. Michaeli, L. Kuipers, and T. F. Krauss, "Flatband slow light in photonic crystals featuring spatial pulse compression and terahertz bandwidth," Opt. Express **15**, 219–226 (2007).

[28] L. Thévenaz, I. Dicaire, and S. Chin, "Enhancing the light-matter interaction using slow light: towards the concept of dense light," in Proc. SPIE, vol. 8273 (2012), pp. 82731D–82731D–8.

[29] F. L. Pedrotti, L. S. Pedrotti, and L. M. Pedrotti, *Introduction to Optics* (Pearson Education, Inc., 2007), 3rd ed.

[30] D. Goldring, U. Levy, and D. Mendlovic, "Highly dispersive micro-ring resonator based on one dimensional photonic crystal waveguide design and analysis," Opt. Express **15**, 3156 (2007).

[31] M. Soljačić, E. Lidorikis, L. V. Hau, and J. D. Joannopoulos, "Enhancement of microcavity lifetimes using highly dispersive materials," Phys. Rev. E **71**, 026602 (2005).

[32] R. Paschotta, article on *"Group Index"* in the *Encyclopedia of Laser Physics and Technology* (accessed on 2015-02-23).

[33] J. Y. Lee and P. M. Fauchet, "Slow-light dispersion in periodically patterned silicon microring resonators," Opt. Lett. **37**, 58 (2012).

[34] K. McGarvey-Lechable and P. Bianucci, "Maximizing slow-light enhancement in one-dimensional photonic crystal ring resonators," Opt. Express **22**, 26032–26041 (2014).

[35] S. G. Johnson and J. D. Joannopoulos, "Block-iterative frequency-domain methods for maxwell's equations in a planewave basis," Opt. Express **8**, 173–190 (2001).

[36] A. F. Oskooi, D. Roundy, M. Ibanescu, P. Bermel, J. D. Joannopoulos, and S. G. Johnson, "MEEP: A flexible free-software package for electromagnetic simulations by the FDTD method," Comput. Phys. Comm. **181**, 687–702 (2010).

[37] S. G. Johnson, "Harminv," http://ab-initio.mit.edu/harminv (2004-2006).

[38] V. A. Mandelshtam and H. S. Taylor, "Harmonic inversion of time signals and its applications," The Journal of Chemical Physics **107** (1997).

[39] T. P. White, L. O'Faolain, J. Li, L. C. Andreani, and T. F. Krauss, "Silica-embedded silicon photonic crystal waveguides," Opt. Express **16**, 17076–17081 (2008).

[40] S. Hughes, L. Ramunno, J. F. Young, and J. E. Sipe, "Extrinsic optical scattering loss in photonic crystal waveguides: Role of fabrication disorder and photon group velocity," Phys. Rev. Lett. **94**, 033903 (2005).

[41] E. Kuramochi, M. Notomi, S. Hughes, A. Shinya, T. Watanabe, and L. Ramunno, "Disorder-induced scattering loss of line-defect waveguides in photonic crystal slabs," Phys. Rev. B **72**, 161318 (2005).

[42] A. Petrov, M. Krause, and M. Eich, "Backscattering and disorder limits in slow light photonic crystal waveguides," Opt. Express **17**, 8676–8684 (2009).

[43] R. Paschotta, article on *"Group Velocity Dispersion"* in the *Encyclopedia of Laser Physics and Technology* (accessed on 2015-02-23).

[44] L. O'Faolain, T. P. White, D. O'Brien, X. Yuan, M. D. Settle, and T. F. Krauss, "Dependence of extrinsic loss on group velocity in photonic crystal waveguides," Opt. Express **15**, 13129–13138 (2007).

[45] A. Y. Petrov and M. Eich, "Zero dispersion at small group velocities in photonic crystal waveguides," Applied Physics Letters **85** (2004).

[46] L. O'Faolain, S. A. Schulz, D. M. Beggs, T. P. White, M. Spasenović, L. Kuipers, F. Morichetti, A. Melloni, S. Mazoyer, J. P. Hugonin, P. Lalanne, and T. F. Krauss, "Loss engineered slow light waveguides," Opt. Express **18**, 27627–27638 (2010).

[47] P. Colman, S. Combrié, G. Lehoucq, and A. D. Rossi, "Control of dispersion in photonic crystal waveguides using group symmetry theory," Opt. Express **20**, 13108–13114 (2012).

[48] D. Goldring, U. Levy, I. E. Dotan, A. Tsukernik, M. Oksman, I. Rubin, Y. David, and D. Mendlovic, "Experimental measurement of quality factor enhancement using slow light modes in one dimensional photonic crystal," Opt. Express **16**, 5585–5595 (2008).

[49] N. A. Wasley, I. J. Luxmoore, R. J. Coles, E. Clarke, A. M. Fox, and S. M. S., "Disorder-limited photon propagation and anderson-localization in photonic crystal waveguides," Appl. Phys. Lett. **101**, 051116 (2012).

[50] J. Topolancik, B. Ilic, and F. Vollmer, "Experimental observation of strong photon localization in disordered photonic crystal waveguides," Phys. Rev. Lett. **99**, 253901 (2007).

[51] Q. Quan and M. Loncar, "Deterministic design of wavelength scale, ultra-high q photonic crystal nanobeam cavities," Opt. Express **19**, 18529–18542 (2011).

[52] L. Sapienza, H. Thyrrestrup, S. Stobbe, P. Garcia, S. Smolka, and P. Lodahl, "Cavity quantum electrodynamics with anderson-localized modes," Science **327**, 1352–1355 (2010).

[53] W. Bogaerts, V. Wiaux, D. Taillaert, S. Beckx, B. Luyssaert, P. Bienstman, and R. Baets, "Fabrication of photonic crystals in silicon-on-insulator using 248-nm deep uv lithography," Selected Topics in Quantum Electronics, IEEE Journal of **8**, 928–934 (2002).

[54] P. Dumon, W. Bogaerts, V. Wiaux, J. Wouters, S. Beckx, J. Van Campenhout, D. Taillaert, B. Luyssaert, P. Bienstman, D. Van Thourhout, and R. Baets, "Low-loss soi photonic wires and ring resonators fabricated with deep uv lithography," Photonics Technology Letters, IEEE **16**, 1328–1330 (2004).

[55] M. Settle, M. Salib, A. Michaeli, and T. F. Krauss, "Low loss silicon on insulator photonic crystal waveguides made by 193nm optical lithography," Opt. Express **14**, 2440–2445 (2006).

[56] S. Selvaraja, W. Bogaerts, D. Van Thourhout, and R. Baets, "Fabrication of uniform photonic devices using 193nm optical lithography in silicon-on-insulator," in Proc. 14th European Conference on Integrated Optics (2008).

[57] D. Taillaert, F. V. Laere, M. Ayre, W. Bogaerts, D. V. Thourhout, P. Bienstman, and R. Baets, "Grating couplers for coupling between optical fibers and nanophotonic waveguides," Japanese Journal of Applied Physics **45**, 6071 (2006).

[58] J. M. Ward, A. Maimaiti, V. H. Le, and S. N. Chormaic, "Contributed review: Optical micro- and nanofiber pulling rig," Review of Scientific Instruments **85**, 111501 (2014).

[59] P. E. Barclay, K. Srinivasan, M. Borselli, and O. Painter, "Efficient input and output fiber coupling to a photonic crystal waveguide," Opt. Lett. **29**, 697–699 (2004).

[60] R. Sarkissian and J. O'Brien, "Cross two photon absorption in a silicon photonic crystal waveguide fiber taper coupler with a physical junction," Journal of Applied Physics **117**, 033101 (2015).